Tracking Proton Transfers in the Optogenetic Proteins Channelrhodopsin-1 and DsLOV

Im Fachbereich Physik der Freien Universität Berlin eingereichte Dissertation zur Erlangung des Grades eines Doktors der Naturwissenschaften (Dr. rer. nat.)

vorgelegt von

Raiza Nara Antonelli Maia

Berlin 2021

Contents

Abstract

The field of optogenetics is in constant development while searching for new optogenetic tools that can be used to control nerve cells, stimulus and optical control of neuronal activity. Among the candidates to be developed as new optogenetics tools, are the LOV (Light Oxygen Voltage) proteins which are ubiquitous photosensors in all domains of life. Channelrhodopsins are frequently used in optogenetics due to their light-gated cation activity, which is a unique characteristic among the ion channels.

Channelrhodopsin-1 from *Chlamydomonas augustae* (*CaChR1*) exhibits slower inactivation under continuous illumination and a shift in the visible maximum absorption compared to Channelrhodopsin-1 and Channelrhodopsin-2 from *Chlamydomonas reinhardtii*. These features are advantageous when developing optogenetic tools, securing *CaChR1* as a viable candidate for research. Here, by variation of amino acid chains, an investigation of the molecular changes in the photocycle of *CaChR1* was conducted. Steady-state and time-resolved molecular spectroscopy revealed the unusual deprotonated cysteine amino acid (C174) in the ground state. It was also established that C174 plays a central role as the internal proton donor to the retinal Schiff base during the decay of the P_2^{380} intermediate state, which is concomitant with the deprotonation of D299 and protonation of E136 and E169 amino acids.

Among the LOV domains an investigation on a variant of the short LOV protein from *Dinoroseobacter shibae* was conducted. The DsLOV-M49S has the advantage of having an exceptionally fast photocycle compared to other LOV domains. This unique feature of DsLOV-M49S enables the performance of time-resolved molecular spectroscopy and the characterization of the thio-adduct state's formation. Using an infrared quantum cascade laser (QCL), the evolution of the weak changes in absorption were successfully

tracked for the S-H vibration of a single cysteine residue. The changes indicate the deprotonation of C72 with a time constant of 12 μs, which coincides with the formation of the FMN-cystenyl-thiol-adduct state.

This thesis focuses on a deep biophysical mechanistic investigation of these two systems candidates to optogenetic tools. The experiments performed elucidate the choreographed sequence of proton transfers, changes in electron densities, spin alterations, and transient bond formations and breakages; all of which supplement and refine the mechanistic interpretation of the light-induced structural changes in LOV domains and *CaChR1*.

Zusammenfassung

Das Gebiet der Optogenetik befindet sich in ständiger Entwicklung bei der Suche nach neuen optogenetischen Werkzeugen, die zur Steuerung von Nervenzellen, Stimuli und optischer Kontrolle neuronaler Aktivität verwendet werden können. Zu den Kandidaten, die als neue optogenetische Werkzeuge entwickelt werden sollen, gehören die LOV-Proteine (Light Oxygen Voltage), welche ubiquitäre Photosensoren in allen Bereichen des Lebens sind. Channelrhodopsine werden aufgrund ihrer lichtgesteuerten Kationenaktivität, die ein Alleinstellungsmerkmal unter den Ionenkanälen ist, häufig in der Optogenetik eingesetzt.

Channelrhodopsin-1 aus *Chlamydomonas augustae* (*CaChR1*) zeigt eine langsamere Inaktivierung unter kontinuierlicher Beleuchtung und eine Verschiebung des sichtbaren Absorptionsmaximums im Vergleich zu Channelrhodopsin-1 und Channelrhodopsin-2 aus *Chlamydomonas reinhardtii*. Diese Eigenschaften sind vorteilhaft bei der Entwicklung optogenetischer Werkzeuge und machen *CaChR1* zum Gegenstand aktuellen Forschung. Hier wurde durch Variation einzelner Aminosäuren eine Untersuchung der molekularen Veränderungen in dem Photozyklus von *CaChR1* durchgeführt. Statische und zeitaufgelöste Molekülspektroskopie zeigte den ungewöhnlichen Deprotonierungszustand einer Cystein-Aminosäure (C174) im Grundzustand. Es wurde auch festgestellt, dass C174 eine zentrale Rolle als interner Protonendonor der Retinal-Schiff-Base während des Zerfalls des P_2^{380}-Intermediats spielt, der mit der Deprotonierung von D299 und der Protonierung der Aminosäuren E136 und E169 einhergeht.

Unter den LOV-Domänen wurde eine Variante des kurzen LOV-Proteins aus *Dinoroseobacter shibae* untersucht. DsLOV-M49S hat den Vorteil, dass es im Vergleich zu anderen LOV-Domänen einen außergewöhnlich schnellen Photozyklus aufweist. Diese

einzigartige Eigenschaft von DsLOV-M49S ermöglicht die Durchführung zeitaufgelöster Molekülspektroskopie und die Charakterisierung der Bildung des Thio-Addukt-Zustands. Unter Verwendung eines Infrarot-Quantenkaskadenlasers (QCL) wurden schwache Absorptionsänderungen der S-H-Schwingung eines einzelnen Cystein-Restes erfolgreich verfolgt. Die Änderungen weisen auf die Deprotonierung von C72 mit einer Zeitkonstante von 12 μs hin, die mit der Bildung des FMN-Cystenyl-Thiol-Adduktzustandes zusammenfällt.

Diese Arbeit konzentriert sich auf eine tiefgreifende biophysikalisch-mechanistische Untersuchung dieser beiden Systeme und evaluiert diese als optogenetische Werkzeuge. Die durchgeführten Experimente klären die choreografierte Abfolge von Protonentransfers, Änderungen der Elektronendichte, Spin-Veränderungen und transiente Bindungsbildungen und -brüche auf; all dies ergänzt die mechanistische Interpretation der lichtinduzierten strukturellen Veränderungen in LOV-Domänen und *CaChR1*.

List of Abbreviations

ATR $\longrightarrow$ attenuated total reflection

AvLOV $\longrightarrow$ Light-Oxygen-Voltage domain from *Avena sativa*

BLUF $\longrightarrow$ Blue-Light-Using-FAD photoreceptors

BR $\longrightarrow$ bacteriorhodopsin

BaF$_2$ $\longrightarrow$ barium fluoride

CaChR1 $\longrightarrow$ channelrhodopsin-1 from *Chlamydomonas augustae*

CrChR1 $\longrightarrow$ channelrhodopsin-1 from *Chlamydomonas reinhardtti*

CrChR2 $\longrightarrow$ channelrhodopsin-2 from *Chlamydomonas reinhardtti*

CrLOV $\longrightarrow$ Light-Oxygen-Voltage domain from *Chlamydomonas reinhardtii*

CRYs $\longrightarrow$ Cryptochromes

DsLOV $\longrightarrow$ Light-Oxygen-Voltage domain from *Dinoroseobacter shibae*

EC-QCL $\longrightarrow$ external cavity quantum cascade laser

FAD $\longrightarrow$ Flavin adenine dinucleotide

FMN $\longrightarrow$ Flavin mononucleotide

FTIR $\longrightarrow$ Fourier transform infrared

HeNe $\longrightarrow$ helium-neon

IR $\longrightarrow$ infrared

ISC $\longrightarrow$ intersystem crossing

LOV $\longrightarrow$ Light-Oxygen-Voltage domain of phot protein

MCT $\longrightarrow$ Mercury-Cadmium-Telluride

OPO $\longrightarrow$ Optical Parametric Oscillator

QM/MM $\longrightarrow$ hybrid quantum mechanism / molecular mechanism

SB $\longrightarrow$ Schiff base

UV/Vis $\longrightarrow$ Ultraviolet/Visible spectroscopy

Introduction

The gain or loss of function in cells of living tissue can be controlled by using genetic and optical methods. The use of these methods are defined as optogenetics. Thus, understanding physical and chemical processes of biological systems including proteins is fundamental for the application of optogenetics, which is a rapidly evolving field.

Optogenetics has taken off with the discovery of the light-gated cation channel, Channelrhodopsin-1, in 2002 by Nagel et. al. [1] having a breakthrough in 2005 with the demonstration of optical control of mammalian neurons using Channelrhodopsin-2 from *Chlamydomonas reinhardtii* [2]. Further development of the technology included the search for new tools, including the optimization of DNA transfer by viruses and the improvement of illumination conditions with light-guiding cables, being the underlying mechanism the use of transmembrane ion channels. The use of photosensitive proteins provides the advantage that stimulation of transfected neuronal cells by light can be performed without the insertion of electrodes into tissue [3]. Beyond activation, new optogenetical tools can also monitor neural activities leading to "all-optical neurophysiology" [4–6].

Channelrhodopsins (*ChR*) are the most common optogenetic tools, due to their unique function to act as light-driven ion channels. The latter feature enables that nerve cells after expressing channelrhodopsin, can be triggered by light to elicit action potentials.

Besides channelrhodopsins, other microbial rhodopsins that are used as candidates optogenetic proteins are chloride pumps such as halorhodopsins that can deactivate nerve cells. The underlying mechanism of photoactivation in these rhodopsins is a *trans/cis* isomerization of the retinal chromophore initiated by photon absorption [1, 7, 8]. Another class of optogenetic tools are blue-light photoreceptors, such as LOV-, BLUF-proteins and cryptochromes that allow for light control over biological phenomena. Optical stimulation drives the blue-light photoreceptors through conformational changes that can be used to modulate signaling events. Here, upon photostimulation the natural photoreceptors get involved in electron transfer or adduct formation [9, 10].

All these optogenetics tools mentioned are proteins, which are defined as macromolecules and have specific functions in biological systems. Proteins are formed by 20 different amino acids linked in a specific sequence to form long chains. Among these amino acids is the cysteine residue, which has unique features exhibiting diverse functionalities in different proteins, such as the tendency to form clusters [11]. Clustered cysteines have a higher degree of conservation than isolated cysteine residues [12]. The cysteine residues have the highest propensity to be located at important functional sites in proteins [12] and they can be affected by electrostatic interactions from secondary structure or also by proximity to charged residues [13, 14]. Despite these interesting properties, cysteines are not as intensively studied as for example aspartates or glutamates. Still, the side chains of these amino acids can act as proton donors/acceptors and can be directly involved in proton transfer in proteins.

Throughout this work, spectroscopic methods are applied to study Channelrhodopsin and LOV -domains that are strong candidates for the development of optogenetic tools. The common feature of these systems are their cyclic reaction that involves proton transfer among reactive amino acids. In this chapter, an overview of the current knowledge about these two systems is presented. Although years of research have already been invested on these proteins, open questions about their mechanism remain. Answering some of these is the topic of this thesis as well as solve the proton transfer

involving the S-H and COOH terminal groups of the cysteine and carboxylic amino acids, respectively. After a brief theoretical introduction about the applied experimental methods, each system will be discussed separately with their own results and discussion part. A particular focus will be laid on the involvement of cysteines in proton transfer in both proteins as this amino acid was mostly overlooked in previous spectroscopic studies due to experimental challenges.

1.1 Channelrhodopsins

1.1.1 Structure and Photocycle of Channelrhodopsins

Complex organism make use of certain stimuli as like light, nutrients, temperature and pressure to adapt their behavior to the environment in which they are inserted. Photoreceptors such as rhodopsins can detected light that is converted into a biochemical signal that is passed on to the nervous system. These mentioned photoreceptors are divided into microbial and animal rhodopsins [15]. Based on their architectures and functions, the microbial rhodopsins can be classified into ion pumps, channels and sensors [16]. Ion channels and pumps are essential for living organisms, due to their involvement in signal transduction pathways and in the transmission of electrical signals [16]. They are located in the cell membranes which are impermeable for water and ions.

However, the presence of aqueous cavities or vestibules in the protein can work as pathways for ion translocation. Based on a specific geometry and charge distribution of polar amino acids, the transported ions are usually filtered by specific binding sites in ion pumps or by a selectivity filter in ion channels [17, 18]. Thus, ion transport across biological membranes is regulated by ion channels and pumps. Despite this similar ability, the ion channels and pumps perform different functions. In pumps the ion transport occurs against the electrochemical gradient transferring the ion across the cell membrane. In ion channels, the ion transport is in a passive flow of ions, causing for example a depolarization in nerve cells and thus triggering an action potential [17, 18] (Figure 1.1). In general, the family of ion channels is subdivided into ligand-gated, voltage-gated and mechano-sensitive channels. The former opens a pore after ligand biding, the second is activated by changes in the transmembrane voltage and the latter is activated by a change in lateral pressure of the cell membrane [18].

Among the ion channels are the channelrhodopsins that have as unique feature their
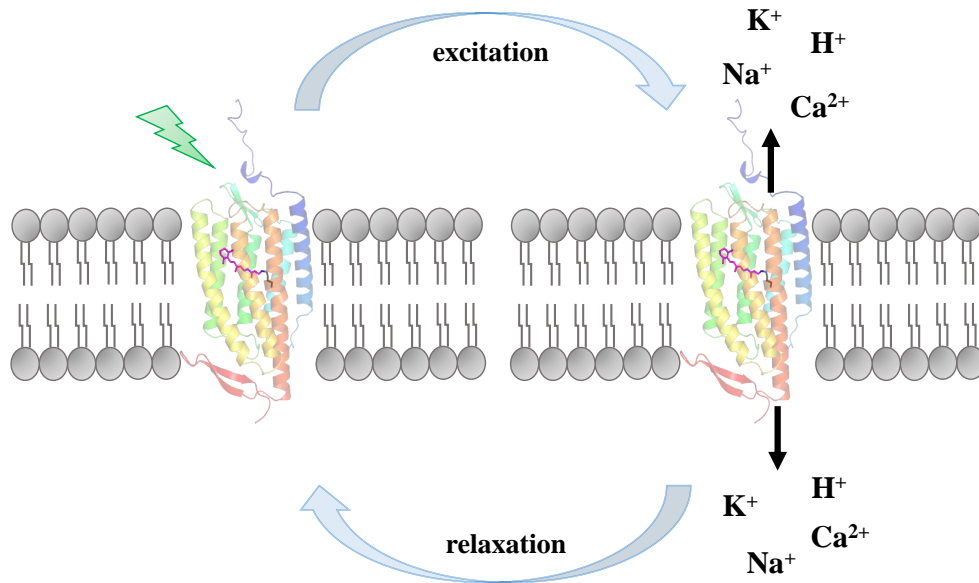
Figure 1.1: Schematic representation of the light-gated cation-selective ion channel channelrhodopsin. The light excitation triggers the formation of the pore while the relaxation leads the channelrhodopsin to the ground state. The retinal chromophore is in magenta and the lipid membrane is shown in grey.

activation being initiated by absorption of a single photon [1]. Buried inside a biological membrane the channelrhodopsins are formed by 7 transmembrane helixes and, like the other rhodopsins, their harbor a retinal as chromophore in the core of the protein, bounded in the form of a protonated Schiff base to a lysine residue to the peptide backbone of the protein (SB - Figure 1.2). In their natural environment, channelrhodopsins are found in the eyespot of green algae and are responsible for the positive and negative phototaxis. Here, the sensory photoreceptors depolarize the plasma membrane in the eyespot upon light activation [1, 7] by increasing the local Ca^{2+} concentration, this induces a yet unknown signalling cascade leading to flagellar movement. At high light intensity, the ion current is mainly dominated by the channel activity of channelrhodopsin. On other hand, at low light intensity, it is speculated that the voltage-controlled calcium channels have a contribution to the overall ion transport.

In optogenetics, the cyclic mechanism of channelrhodopsins are quickly activated to depolarize cell membranes with light, triggering the ion flow through the membrane [19].
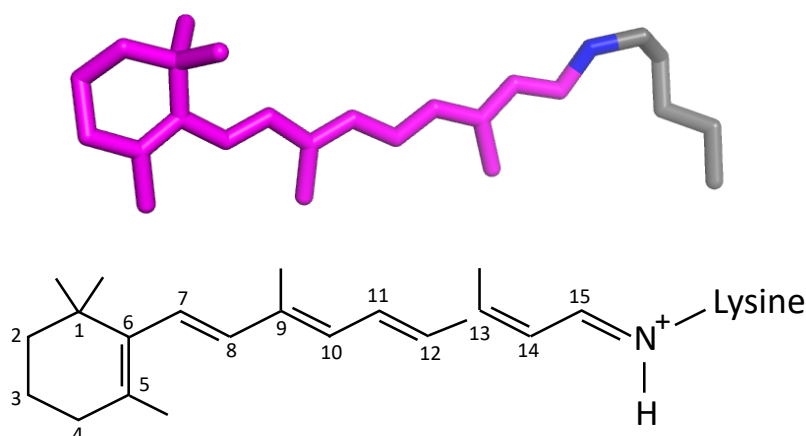
Figure 1.2: Retinal chromophore structure (sticks representation) and labeled chemical representation (bottom). The all-*trans* (15-anti) retinal is covalently bound to a lysine residue via a protonated Schiff base. This retinal configuration is present in the ground state of *CaChR1* and is the starting point of the all-*trans* photocycle. Upon light excitation, *CaChR1* retinal isomerizes to 13-*cis* with changes of the C_{13}=C_{14} double bond.

The cyclic mechanism and the flow of selected ions make channelrhodopsins versatile and useful as optogenetic tools for altering membrane potentials [20]. In addition, it is possible to produce and use channelrhodopsin variants and fusion constructs [21], in order to optimize their properties and function in optogenetics, as like shift of the visible absorption maximum and the desensitization of the protein [22].

Even with the possibility of the constructions of *ChR* variants, the search for natural optogenetics tools is still in progress, since the mechanism of *ChR* photoreaction is not yet fully understood. In 2011 up to 13 different channelrhodopsins were identified. The differences between them are mainly reflected in their kinetics, cation selectivity, absorption spectrum and light sensitivity [23–27]. Among these 13 different channelrhodopsins are the *ChR* from *Chlamydomonas reinhardtii* (*CrChR1* and *CrChR2*) [28] that are the most investigated ones, due to their overall properties suiting best the needs of optogenetic application. However, *CaChR1* from the algae *Chlamydomonas augustae* has two advantageous properties regarded to optogenetics compared to the *CrChR1* and *CrChR2*. First, *CaChR1* has a red-shifted absorption maximum at 518 nm and can therefore be activated with light of longer wavelengths, which can penetrate deeper

into tissue. Second, the inactivation of *CaChR1* is slower under continuous illumination, this mean that the *CaChR1* is open longer under continuous illumination compared to *CrChR1* [23]. Therefore, it is informative/instructive to understand the dynamics and molecular processes that occur in *CaChR1* leading to these properties. This knowledge will certainly be beneficial in further improving *Chrs* variants.

1.1.2 Channelrhodopsin-1

Channelrhodopsins are polymorphic proteins and can be identify and classify based on their amino acid sequence. Since sections of this sequence are essential for their function and are therefore conserved among different populations. The most studied channelrhodopsins, *CrChR1* and *CrChR2*, belong to different branches of the phylogenetic tree because their conserved amino acids are different [23]. Thus, the channelrhodopsin from *Chlamydomonas augustae* was classified as a channelrhodopsin-1 based on two conserved amino acids E94 and Y233. As like *CrChR1*, *CaChR1* also has 7 transmembrane α helices and a longer C-terminus [23, 29], which the function is not yet well defined. However, it is suggested that the C-terminus determines the position of the channelrhodopsin in the eye spot of the algae [23, 29]. Interestingly, most of the functional amino acids of *CrChR2* are also conserved in the sequence of *CaChR1*. Namely, the two counterions of the Schiff base E123 (E169) and D253 (D299), the proton donor D156 of *CrChR2* is conserved and analogous to D202 in *CaChR1* and the amino acid E90 that is essential for ion selectivity in *CrChR2*, is also conserved in *CaChR1* as the E136 amino acid (Figure 1.3).

A distinct characteristic of *CaChR1* is an unusually large number of the cysteine residues compared to other rhodopsins. In total, there are 14 cysteines in the *CaChR1* structure (*CrChR2* has only 9 cysteine or *BR* which does not have any cysteine) being the C174 the equivalent to the cysteine C128 of the DC gate of the *CrChR2*, adjacent to C174 is a second cysteine C173 unique for the *CaChR1* structure (Figure 1.3). Interestingly, we can identify the presence of 7 cysteines forming a waistband in the middle of the transmembrane region C133, C134, C173, C174, C231, C232 and C109 (Figure 1.3). Due to their centralized positions it is likely that one or more cysteines are directly or indirectly involved in the proton transfer during the reaction of *CaChR1*.

After the light excitation *ChRs* go through a cyclic mechanism, the ion channels open temporarily a pore enabling the free transposition of ions from the inside and outside
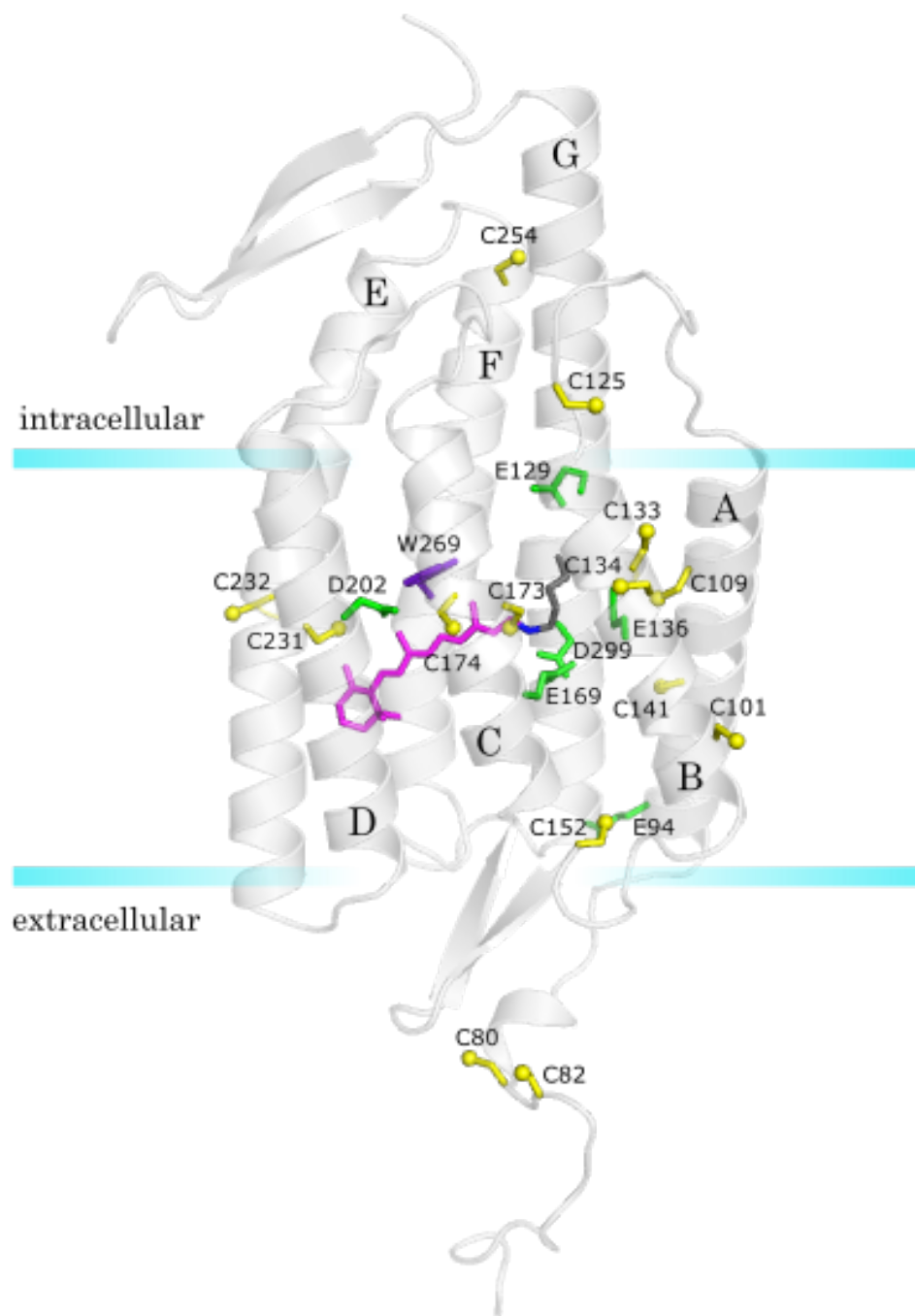
Figure 1.3: Homology model of the monomer of *CaChR1* created by the SWISS-MODEL server, using the C1C2 structure (PDB: 3UG9) [30–32]. Shown is the retinal (from the structure of C1C2) in magenta, as well as relevant amino acids: carboxyl groups in green and all present cysteines in yellow. Clearly visible are the three adjacent cysteine pairs (C133/C134, C173/174, and C231/C232), which together with C109 lie in the center of the transmembrane region.

of the cell. Theses cyclic reactions are know as a photocycle. The light excitation let

the retinal of the protein adapts to a new corformational isomerization that triggers

rearrangements in the secondary structure, which can affect their functionality. The photocycle of the protein is concluded by the reisomerization of the retinal leading the protein back to the ground (resting) state, allowing the re-execution of the function. The channelrhodopsins can also go through the desensitization or inactivation process [22] due to the accumulation of less conductive intermediates, inhibiting the re-execution of the photocycle.
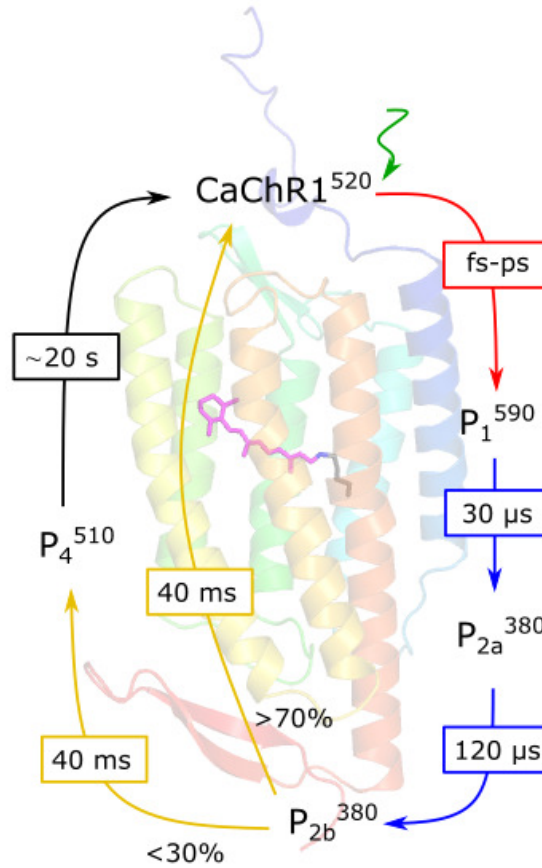
Figure 1.4: Schematic representation of the branched photocycle of *CaChR1* [33]. Shown is the sequence of the intermediates with their respective absorbance (superscripts) and the time constants of decay. *CaChR1^{520}* is the ground state form mainly by all-*trans* isomerization. P_1^{590} first intermediate after green-light excitation, resulting in isomerization to 13-*cis* and a red shifted photoproduct. P_{2a}^{380} and P_{2b}^{380} are blue shift intermediates with deprotonated Schiff base. The P_2^{380} represent the open (conductive) state in *CaChR1* photocycle. The reisomerization back to all-*trans* configuration does not take place until the decay of the P_4^{510} state.

Even with intense investigation of *CaChR1*, there is still no consensus on the isomeric composition of *CaChR1* retinal in the ground state. Ogren et. al. [34] suggested that

the ground state is formed almost for pure all-*trans* retinal based on resonance Raman spectroscopic data. On the other hand, Muders et. al. [35] using also resonance Raman spectroscopy suggested a heterogeneous ground state population comprise of 30% 13-*cis* and 70% all-*trans* retinal. Further, short-lived intermediates were identified and the photocycle scheme of *CaChR1* was propose as shown in Figure 1.4 [33]. Here, continuous illumination of *CaChR1* with green light (518 nm) accumulates the blue shifted P_2^{380} intermediate state [35], which unlike the ground state has a deprotonated Schiff base. The P_2^{380} is suggested being a two phase intermediate (P_{2a}^{380} and P_{2b}^{380}) [29, 33].

Using time-resolved rapid scan spectroscopy Muders et. al. [33] and Lórenz-Fonfría et. al. [36] followed the biphasic recovery of the negative C-C stretching vibrational band at 1237 cm^{-1}, assigned to the all-*trans* retinal of the ground state [33, 35]. The recovery of this vibrational mode ((-) 1237 cm^{-1}) coincides with the decay of the P_{2b}^{380} intermediate ($> 70\%$ of the vibrational mode decays), while the remaining intensity decays with recovery of the ground state [33, 36]. Thus, it was suggested by Ref. [33] that *CaChR1* has a branched photocycle in which the majority of the molecules in the P_{2b}^{380} intermediate relax directly to the ground state, while the remainder molecules presumably transition to the ground state via P_4^{510} intermediate state. This would be analogous to *CrChR2*, where also only a fraction of the molecules ($\sim 25\%$) pass through the P_4^{480} intermediate and the majority ($\sim 75\%$) go back to the ground state directly after the open P_3^{520} intermediate [37]. The branch photocycle in *CrChR2* indicates that most of the molecules close the channel in the transition from P_3^{520} to ground state, restoring the initial retinal and protein conformation. The smallest fraction that goes through the P_4^{480} intermediate possibly close the channel and do not revert all the conformational changes in the protein backbone [37].

Electrophysiological measurements performed by Hou et. al. [23] on *CaChR1* have shown that the inactivation of the ionic current is slower compared to *CrChR1* keeping the channel open longer [23]. Sineshchekov et. al. [29] found that exchange of E169 for a glutamie (Q) greatly reduces the outwardly directed proton transfer as well as

the passive ion current, while the exchange of D299 for an asparagine (N) has only a minor effect on the outwardly directed proton transfer and appears to be decisive only for the channel opening. Thus, the results from Sineshchekov et. al. [29] suggest that the E169 could be a possible primary proton donor [29], reinforcing the possible central participation of this amino acids in the *CaChR1* photocycle.

Although many other spectroscopy approaches were applied on *CaChR1* [34–36, 38–40], the proton transfer pathway in *CaChR1* is still unknown. Thus, trying to solve the proton transfer pathway, even partially, is one of the goals of this work.

1.2   Light-Oxygen-Voltage (LOV) photoreceptors

1.2.1   Structure and Photocycle of LOV domains

In biological systems six different photoreceptor proteins are classified based on the chemical structure of the light-absorbing chromophores [41], being three of them blue-light sensitive. These blue-light photoreceptors have as characteristic a chromophoric cofactorflavin, responsible for the yellow coloration of the protein and a maximum absorption at around 450 nm. The natural blue-photoreceptors can be subdivided in Cryptochromes(CRYs) and BLUF photoreceptors (blue-light sensors using flavin) that carry flavinadenine dinucleotide (FAD) as a cofactor and the phototropin photoreceptors that have the signal genereted by LOV domain (light, oxygen,voltage) which harbor a flavin mononucleotide (FMN) acting as a chromophore (Figure 1.5).
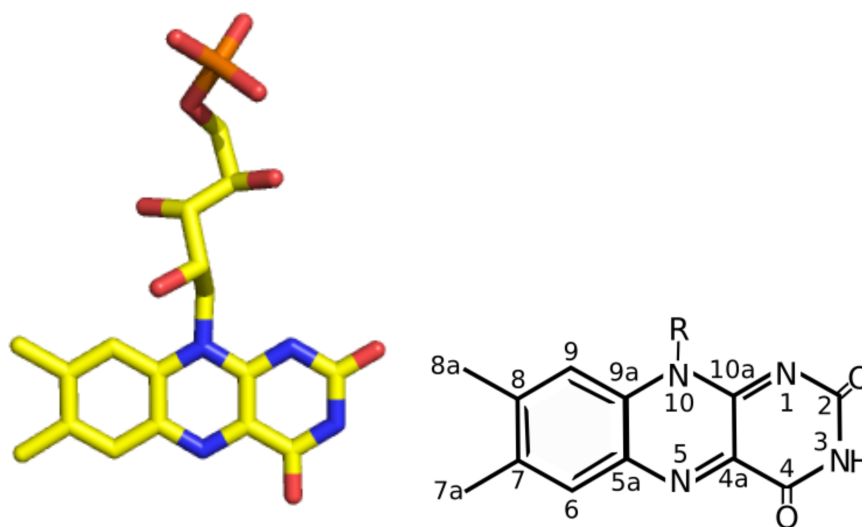
Figure 1.5: Flavin Mononucletide (FMN) chromophore 3D structure (left), and the labeled chemical representation of FMN (right).

The photoreceptors of the phototropin family are widely found in all kingdoms of life and regulate different cellular functions such as phototropism, chloroplast movement and stomatal opening [10, 42, 43]. The molecular nature and the function of phototropins have been identified to *Arabidopsin*, where the regulation of Hypocotyl phototropins

occur by two phototropins known as LOV1 and LOV2 [44, 45]. Unlike in the unicellular green alga *Chamydomonas reinhatdii* [46, 47] with only one phototropin identified that is engaged in blue-light mediated sexual life cycle [48].

As shown in Figure 1.6, the overall protein structure can be described with a N-terminal having the photosensory domain, followed by a conserved α helix (called Jα) and the C-terminal with the serine/theorine kinase domain. The N-terminal has two domains LOV1 and LOV2, which are similar to each other and are composed by $\sim$110 amino acids [42]. The LOV domains are members of the large family of PAS (Per - Period circadian protein, ARNT - Ah receptor translocator protein, Sim - Single-minded protein) domains associated with cofactor binding and mediating protein interactions [49].

Figure 1.6: Domain architecture of Phototropin protein. Each LOV domain has one FMN and they are bound to serine/threonine kinase domain.

After blue light excitation, LOV domains undergo a cyclic photoreaction consisting of a sequence of intermediate states. Several spectroscopic studies have been applied in the attempt to characterize and understand the intermediate states that lead to the active conformation containing a FMN-cysteinyl-thiol-adduct ([LOV]^A) (Figure 1.7). The adduct state is formed between the FMN chromophore and the terminal thiol group of a nearby cysteine residue (Figure 1.7). This reaction involves the release of the proton of the thiol moiety of the reactive cysteine, the protonation of the N_5 atom of the FMN and the formation of a covalent bond between the reactive cysteine and the C_{4a} atom of the FMN isoalloxazine ring [50–55]. Finally, the photocycle is completed when the adduct state reverts thermally back to its original dark state in a few seconds to hours [55–62].

The cyclic photoreaction of LOV domains starts with excitation into the singlet-excited
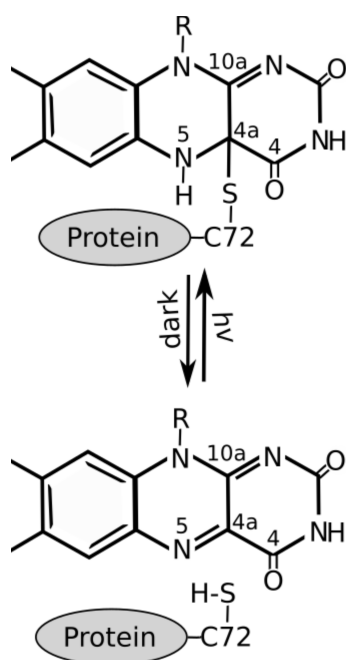
Figure 1.7: Chemical structure of the catalytic co-factor FMN in LOV domains. Blue light excitation induces a reversible formation of the covalent bond between FMN and the reactive cysteine residue C72. The adduct reverts thermally back to the dark state on a timescale of seconds to hours.

state of the FMN cofactor in fs-ns time range [56, 63]. Intersystem crossing (ISC) populates the triplet state ($[LOV]^3$) on the nanosecond time scale and decays at a time range of microseconds [57, 58]. In the subsequent microsecond range, a small fraction of the triplet state decays back to the ground state while the largest amount of the triplet state decay yields a covalent FMN-cysteinyl-thiol-adduct ($[LOV]^A$ - Figure 1.8). The adduct state is well accepted as the active signaling state of the LOV domains, due to its long-living nature and the lack of additional intermediates during the decay to the dark state.

Despite of extensive research on the photoreaction of LOV domains over the last few years, the reaction sequence leading to the formation of the flavin-cysteine adduct has not yet been fully resolved. Various possible pathways have been proposed [52–54, 57, 58, 64, 65], as summarized in Figure 1.8.

Among them is the concert mechanism, where a direct proton transfer from the reactive cysteine thiol to the N_5-FMN atom during the triplet state is expected consequently, the
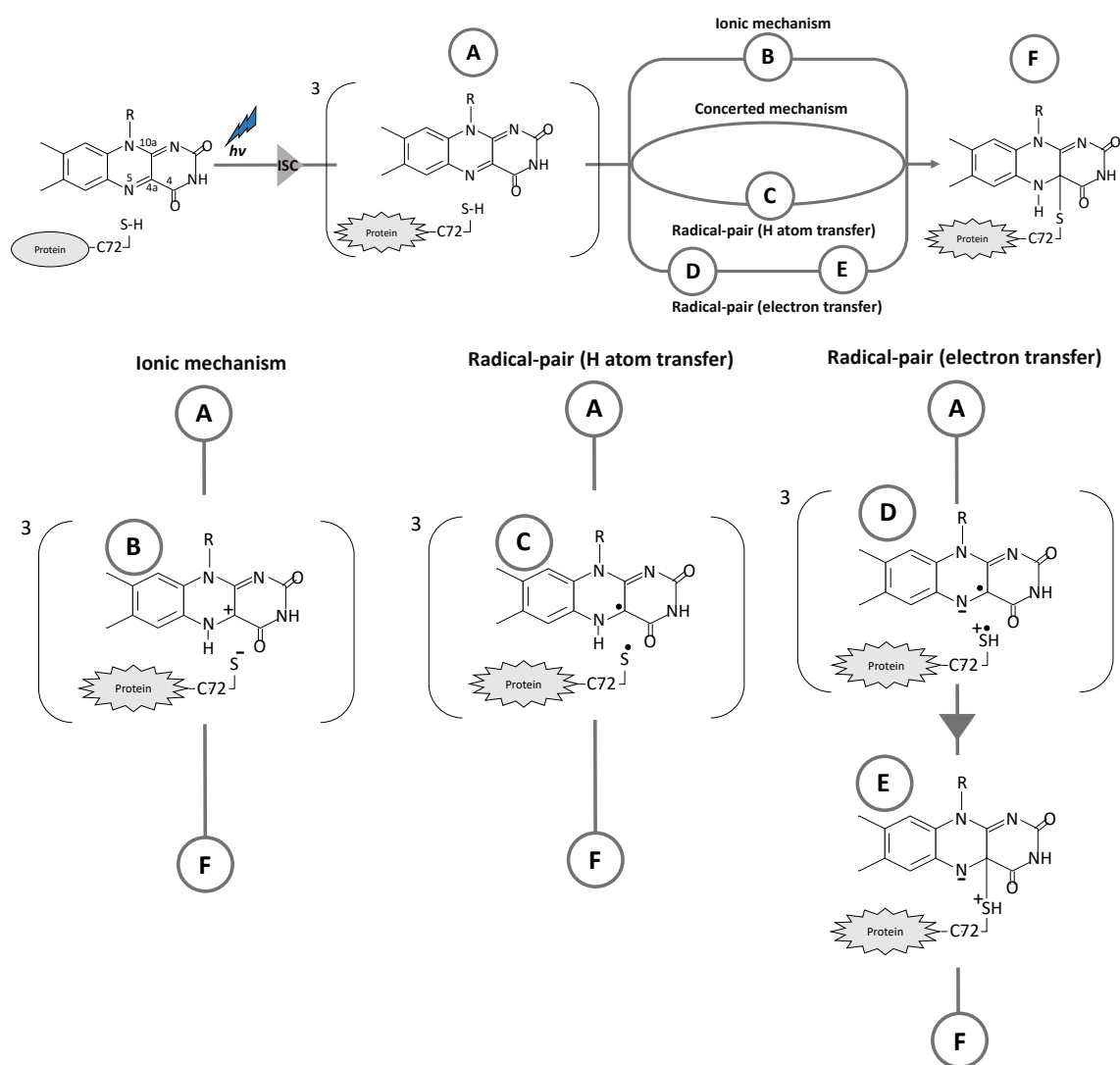
Figure 1.8: Suggested reaction pathways (top) and intermediates (bottom) in the DsLOV domain wild-type. The different intermediates are indicated as A: triplet state, B: ionic mechanism, C: radical-pair with H atom transfer, D: radical-pair with electron transfer and F: adduct state. The intermediates B, C and D have not been detected experimentally in wild-type LOV domain.

sulfur from the reactive cysteine attacks the C_{4a}-FMN forming the covalent bond [54]. Using the crystal structure of LOV1 domain to calculate the charge redistribution of FMN upon the formation of the triplet state, Fedorov et. al. [53] proposed that the S-H proton of the reactive cysteine moves towards the N_5 atom of FMN during the life-time of the triplet state. Meanwhile, the interaction between the reactive cysteine and the C_{4a} atom increases, going to the point that the sulfur and C_{4a} orbitals overlap with each other and forming the adduct state. On the other hand, the Ab initio quantum

chemical investigation by Neiss and Saalfrank [65] indicated that the adduct formation during the triplet state is unlikely.

Another pathway discussed in previous literatures is the ionic mechanism (Figure 1.8 B) proposed by Stwartz et. al. [58]. Here the proton transfer from the reactive cysteine to the [LOV]³ will happen before the covalent bond formation take place (C_{4a}-S). It was shown experimentally using FTIR spectroscopy that the reactive cysteine is protonated in the ground state [66, 67]. Based on this, Crosson et. al. [54] suggested that the initial step to the adduct formation would be proton transfer from the reactive cysteine to the N_5 atom during the triplet state, followed by the covalent bond formation between the S-Cys and the C_{4a}-FMN. Spectroscopic investigations of the *Adiantum* phy3 LOV2 by Kennis et. al. [57] supported the possibility of a protonated triplet state.

Lastly, the reaction more endorsed by literature is the radical-pair mechanism involving either a hydrogen atom transfer (Figure 1.8 C) or via zwitterionic adduct species. Here, an electron transfer occurring first while the thiol proton is still bonded at the sulfur atom, followed by the covalent bond formation before the hydrogen atom is transfered from the reactive cysteine to N_5 atom (Figure 1.8 D and E). Electron paramagnetic resonance (EPR) studies found that the radical-pair mechanism would be the dominat reaction pathway in the transition from the triplet state to the adduct formation as suggested by Ref. [68, 69]. However, Quantum-chemical simulation by Neiss et. al [65] and quantum mechanical/molecular mechanical (QM/MM) simulation by Dittrich et. al. [52] found that a neutral radical mechanism proceeding via hydrogen atom transfer and consequently the formation of a neutral radical (Figure 1.8 C) is energetically more favorable than passing via zwitterionic radical species. This interpretation is additionally supported by the studies conducted in the cysteine variant of *Chlamydomonas* LOV1 [70, 71]. However, until now none of the recent studies presented solid evidences to support these proposed mechanisms. Thus, an experimental approach is required which can resolve the kinetics of deprotonation of the reactive cysteine and formation of the covalent bond involved in the rise of the adduct state. Unfortunately, the usually long

dark state recovery lifetime challenges time-resolved experiments which typically require many repetitions for signal averaging.

1.2.2   *Dinoroseabacter Shibae* LOV domain

Inside the LOV domains photoreceptors branch there is a wide variety of "short" LOV proteins, which can be found in bacteria and fungi having no effector domains [72–77]. Even without the effector domains the short LOV domains have the ability to act as blue-light receptors [74, 76, 77]. So far, the structural characterization of short LOV proteins suggest that outside the conserved LOV core domain, all the short LOVs have N- and/or C-terminal helical extensions (N-terminal N-cap or A′α-helix and C-terminal Jα-helix) which are involved in signaling [74, 75, 77].

The short LOV protein DsLOV from the photoheterotrophic marine α-protobacterium *Dinoroseabacter shibae*, was recently described and characterized with regard to structure and function [78, 79]. Strikingly, DsLOV exhibits unique characteristics opposed to other LOV photoreceptors, for example participating in the regulation of photopigment synthesis in the absence of blue-light. Thus, DsLOV domains use the dark state as the physiologically relevant signaling state [78, 79]. In accordance to this finding DsLOV shows a strongly accelerated photocycle with a lifetime of the adduct-state of τ=9.6 s [78].

Moreover, DsLOV owes a methionine (M) residue at position 49 [78, 79], whereas in other LOV domains usually an isoleucine or leucine residue is found at this position. Several studies have shown that the exchange of residues at this position can strongly influence the adduct-state lifetime of LOV proteins [57, 61, 79]. Based on this, Fettweiss et. al. [79] conduced a study to analyze how the residue alterations at position 49 could affect the recovery of the protein back to the ground state. Using kinetic, thermodynamic and structural analyses of different variants they were able to describe how the residue alterations can affect the energetics of the dark-recovery process, due to changes in the

steric strain of the link between FMN and the cysteine thiol, affecting the access of the solvent on the active site of the LOV domains.
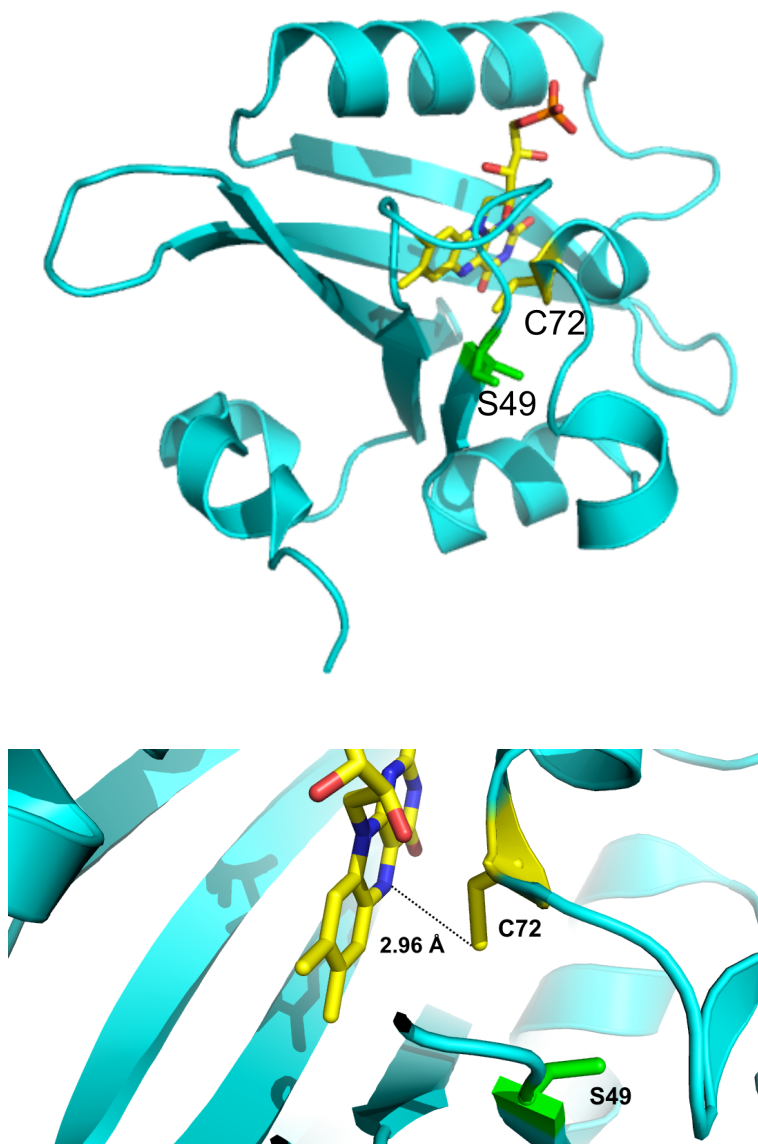
Figure 1.9: X-ray structural model of the DsLOV-M49S domain from the photoheterotrophic marine α-protobacterium *Dinoroseabacter shibae* (PBD: 6GB3) in the dark state (top). Close up of the crystal structure of DsLOV-M49S indicating the distance between the C_{4a}-FMN atom and the S atom from the reactive cysteine (bottom).

Fettweiss et. al. [79] showed that the replacement of M49 by a serine (S) in DsLOV produces a variant with faster dark recovery than other natural variants, without revealing strong structural changes compared to the wild type. The crystalline structure of the DsLOV-M49S is shown in Figure 1.9. The accelerated recovery rate of dark-state

of the DsLOV-M49S after photoactivation ($\tau = 1.6$ s [79]) facilitates time-resolved spectroscopic experiments, strictly speaking it enables convenient averaging, which is necessary to get a data set with good resolution to track the evolution of different intermediate states involved in the DsLOV-M49S photocycle.

1.3 Scope of this work

Channelrhodopsin-1 and DsLOV domains are light-induced proteins and promising new optogenetic tools. Although these proteins were intensively studied for years, their reaction dynamics are still not fully resolved. In this thesis, I elucidate on their photoreaction focussing on proton pathways.

For this, time-resolved IR spectroscopy is a non-invasive technique that combines structural sensitivity with high temporal resolution. This method is in particular suitable to solve and assign the temporal structural changes in apoproteins. With this information, I can shine light on the photocycle intermediates and answer the pathway of proton transfer in *CaChR1*, which is presumably responsible for the opening and closing of the channel.

The mechanism involved in the transition from the triplet state to the FMN-cysteinyl-thiol-adduct state is still unknown for the LOV domains proteins, mostly due to the slow photocycle of LOVs. The recent characterization of the *Dinoroseabacter Shibae* LOV with a faster photocycle comparing to other LOV domains enables me to perform time-resolved absorption spectroscopy with high signal-to-noise ratio combing different spectroscopic techniques, electronic and molecular structure information can be obtained, permitting clarification if the proton transfer from the reactive cysteine to FMN is the rate-limiting step in the formation of the adduct state.

For both proteins, the cysteine amino acids are expected to play a central role during the development of the photocycle, one of the principal challenges is to track the cysteine dynamics by conventional IR techniques because of the low excitation coefficient of the S-H hydrogen bonding. This issue was overcome with the development of time-resolved IR spectrometer employing the intense emission from a tunable external cavity quantum cascade lasers (EC-QCLs). The high photon flux of QCLs [80] facilitates the detection of contributions of single amino acids such as the weak S-H vibration of the cysteine

residues.

Material and Methods

2.1 Sample Preparation

The experiments were performed only on proteins that have a very good ratio of purity assuring good data quality (*CaChR1* the ratio is $A_{280}/A_{520} = 2.3 - 2.8$)). The purified *CaChR1* wild-type protein and the variants were supplied by the laboratory of *Dr. Ramona Schlesinger* (Freie Universität Berlin), sample production is described in Ref. [33]. The DsLOV-M49S sample was supplied by the *Dr. Ulrich Krauss* laboratory (Heinrich Heine Universität Düsseldorf), the sample preparation was described previously in Ref. [78, 79]. The proteins were solubilized in water resulting in a strong absorption peak in the infrared at around 1650 cm^{-1}. To reduce the water absorption, highly concentrated protein films ensuring a fine balance in water content.

The film samples were prepared as follows, 5-10 mg/mL of concentrated protein solution was dried on a BaF_2 window. 3 μL of glycerol/water mixture (2:8 weight/weight) was then placed close to the dehydrated sample and the sample was subsequently sealed with a second BaF_2 window. Between the windows a 1 mm thick spacer was sandwiched using vacuum grease, as show in Figure 2.1. The dry sample was let rehydrated over the vapor phase generated by the glycerol/water mixture during 1 h [81]. The amount of protein used depended on the vibrational region of interest. To perform experiments
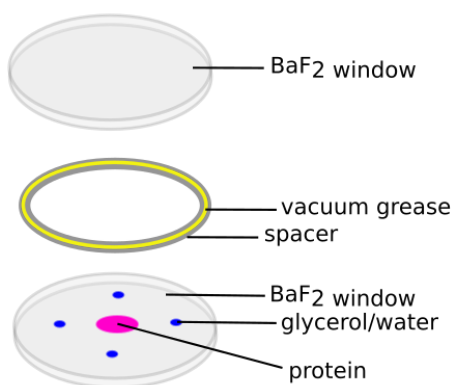
Figure 2.1: Diagram of sample preparation for the transmission technique.

in the S-H vibrational range (2600-2500 cm^{-1}) a thicker sample is necessary due to the low signal intensity of this vibration.

In order to get a homogeneous protein film the *CaChR1* protein solution (wild-type and variants) was previously brought to a lower detergent concentration (2%). This process was controlled by an attenuated total reflection (ATR) experiment of the liquid sample. To reduce the detergent concentration in *CaChR1*, the solution washed at least 5 times with 5 times the volume of the original sample. For *CaChR1* wild-type and variants a buffer solution containing 2 mM NaCl, 5 mM HEPES at pH 7.4 was used. The DsLOV-M49S is a water soluble protein that was concentrated on a 10 mM sodium phosphate buffer at pH 8. All samples were measured at room temperature ($\sim$24 °C). The experiments in this work were performed on the following proteins and their variants: DsLOV-M49S, *CaChR1* wild-type, E169Q, E136Q, D299E, D299N, D202N, C173T, C174T and C173/174T.

2.2   Theoretical Background

Spectroscopy, at its core, is the study of electromagnetic radiation interacting with atoms bound together to form molecules of matter. Each type of the electromagnetic radiation provokes a different interaction with the molecules and the total energy can be described as a sum of the contributing energy terms

$$E_{total} = E_{eletronic} + E_{vibrational} + E_{translational} + E_{rotational} + ... \tag{2.1}$$

The eletronic energy, $E_{eletronic}$, is relate to the motion of electrons, vibrational energy, $E_{vibrational}$, is linked to the absorption of energy by a molecule as the atoms vibrate, translational energy, $E_{translational}$, corresponds to the displacement of the molecules in space and rotational energy related with the rotational motion of a molecule [82, 83]. The total energy (Equation 2.1) has other contributions, which are neglected here.

The description of the total energy of a system can be complex, where one of the most simple cases is that of a diatomic molecule where the atoms are two points of mass (m_i) connected to one to another by a spring (k_{ij} spring constant). For this classic case, the potential can be assume as a harmonic oscillator (Figure 2.2 - red trace) [84]. Using quantum mechanics, the quantization of the eigenvalues can be taken into account and their vibrational energies can be calculated solving the Schroedinger's time-independent equation

$$\hat{H}\psi = \left(\frac{\hat{p}^2}{2m} + V_{(r)} \right)\psi = \frac{\hbar^2}{2\mu}\frac{d^2\psi}{dr^2} + \frac{k_{ij}}{\mu}\frac{1}{2}(r - r_0)^2\psi = E\psi \tag{2.2}$$

$$\mu = \frac{m_1 m_2}{m_1 + m_2} \rightarrow \text{reduced mass of the atoms.}$$

Where $\hat{H}$ is the Hamiltonian, $\hat{p}$ the momentum operator, $V_{(r)}$ the potential energy, r

the distance between two atoms, k_{ij} is a constant representing the strength of the bond and ψ the wave function with its corresponding energy E. Thus, the energy eigenvalues are

$$E = \left(\nu + \frac{1}{2}\right)\hbar\omega \tag{2.3}$$

$$\omega = \sqrt{\frac{k_{ij}}{\mu}} \rightarrow \text{correspond to the angular frequency.}$$

Based on the quantized eigenvalues the molecules can vibrate at a certain frequencies, which can be describe to a diatomic molecule as

$$\nu = \frac{1}{2\pi c}\sqrt{\frac{k_{ij}}{\mu}}. \tag{2.4}$$

The minimum energy of the system is well-described by the harmonic potential model. However, at higher energies the system can be more accurately approximated by considering the potential energy surface given by the anharmonic Morse potential (Figure 2.2) [84]

$$V(r) = V_0(1 - e^{-a(r-r_0)})^2 \tag{2.5}$$

$$a = \left(\frac{\mu\omega^2}{2V_0}\right)^{\frac{1}{2}} \rightarrow constant,$$

where the V_0 is the dissociation energy, a the slope of the potential and r_0 the resting distance. By solving the Schrödinger's equation with the anharmonic Morse potential, the energy eigenvalues can be described as

$$E = \left(\nu + \frac{1}{2}\right)\hbar\omega - \left(\nu + \frac{1}{2}\right)^2 \frac{\hbar^2\omega^2}{4V_0}. \tag{2.6}$$

In the anharmonic Morse potential, unlike in the harmonic potential, the energy difference between two vibrational levels is not constant. As the vibrational quantum potential increases, the difference between the levels decreases, until the dissociation of the molecule [84].
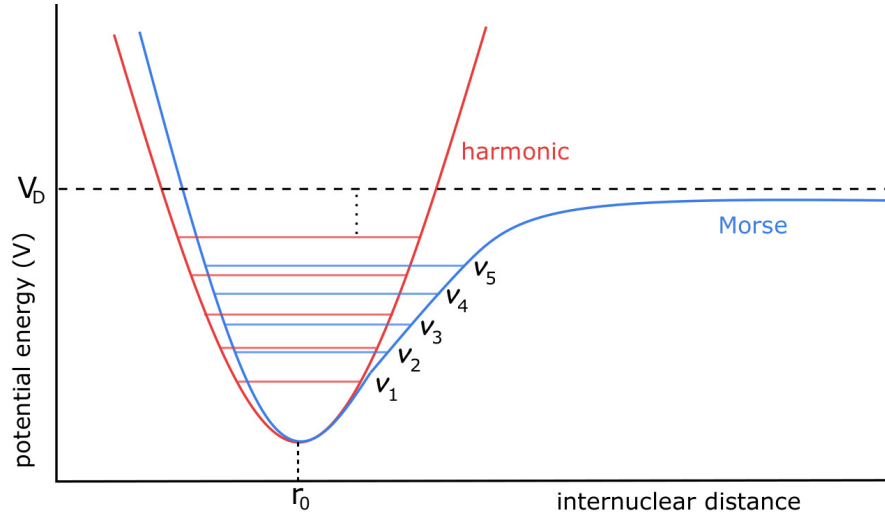
Figure 2.2: Schematic representation of the 1-dimensional harmonic potential (red) and Morse potential (blue). The vibrational energy levels are indicated by vertical lines.

So far we have only discussed the case of a diatomic molecule. However, we can extrapolate upon this and consider the case of a polyatomic molecule containing N atoms that exhibit 3N degrees of freedom [84]. Using the Hooke's law in the quadratic form, the potential energy can be described as

$$V = \frac{1}{2} \sum_{j=1}^{3N} \sum_{i=1}^{3N} f_{ji} q_j q_i, \tag{2.7}$$

when it is used the so-called mass-weighted displacement coordinates $q_i = \sqrt{m_i} x_i$, x_i are the Cartesian displacement coordinates and f_{ji} are the force constants.

Using classical mechanics and assuming the absence of external and non-conservative forces, we can write Newton's equation of motion as

$$\frac{d}{dt}\frac{\partial T}{\partial \dot{q}_j} + \frac{\partial V}{\partial q_j} = 0, \tag{2.8}$$

where T is the kinetic energy [83]

$$T = \frac{1}{2}\sum_{j=1}^{3N} \dot{q}_j{}^2. \tag{2.9}$$

Replacing the Equations 2.7 and 2.9 into Equation 2.8

$$\ddot{q}_j + \sum_{i=1}^{3N} f_{ij}q_i = 0. \tag{2.10}$$

Equation 2.10 represents a set of 3N linear second-order differential equations, where a general solution can be written as

$$q_j = A_j cos(\omega t + \phi), \tag{2.11}$$

A_j is the amplitude of displacement in the j direction of Cartesian axis, ϕ is the phase angle [85]. Where each solution to the 3N equations corresponds to a specific frequency, ω [83, 85]. Replacing Equation 2.11 into Equation 2.10 yields

$$- A_j\omega^2 + \sum_{i=1}^{3N} f_{ij}A_i = 0 \tag{2.12}$$

which corresponds to 3N linear equations for the amplitude of displacement in the j direction of Cartesian axis A_j and the eigenvalues are the squares of the so-called normal mode vibrational frequencies. Considering the summation over all 3N degrees of freedom, 6 for a nonlinear and 5 for a linear molecule, the frequencies related to translational and rotational motions of the whole (non-linear and linear) molecule must be zero. Which leaves then 3N-6 (non-linear molecule) and 3N-5 (linear molecule) non-zero eigenvalues ω_j^2 [84, 85]. These non-zero solutions are nominated as the normal

modes. Even though the treatment of normal modes in the Cartesian coordinate system is simple and straightforward, it has the disadvantage that the normal modes information is spread over 3N equations. Thus, in order to simplify the representation of the probabilities of vibrational transitions in quantum mechanics, an orthogonal transformation can be used to convert the mass-weighted Cartesian coordinates (q_i) into normal coordinates (Q_k)

$$Q_k = \sum_{i=1}^{3N} l_{ik} q_i, \qquad (2.13)$$

where an individual transformation coefficient, l_{ik}, is applied for each normal mode, k. The normal coordinates describe that each of the 3N normal modes of vibrations are related only to one normal coordinate Q_k. For this new representation, six of the normal coordinates describe cases with zero vibrational frequency (three translations and three rotations) [83, 85], Figure 2.3 illustrates the vibrational modes of a triatomic system.

symmetrical stretch   bending   rocking

asymmetrical stretch   twisting   wagging
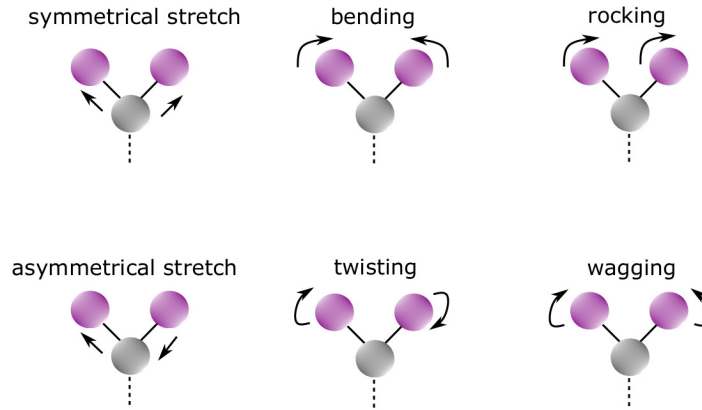
Figure 2.3: Molecular vibrational mode of a triatomic system. The stretch, bending and rocking vibrations take place in the plane of the system while the twisting and wagging vibrations are out-of-plane.

In a molecule the transitions between two vibrational states Ψ_f (final state) and Ψ_i (initial state) are induced by the absorption of a photon ($E_{photon} = \hbar\omega = \Delta E$), the process is controlled by the transition dipole moment operator, $\hat{\mu}$, which is the sum

over all electrons, ε, and nucleus, N, of the molecule

$$\hat{\mu} = \hat{\mu}_\varepsilon + \hat{\mu_N} = -e\sum_\varepsilon \hat{r}_\varepsilon + e\sum_N Z_N \hat{R_N}, \tag{2.14}$$

where e is the elementary charge of the electron and Z_N the charges of the nucleus. Due to the contributions of electrons and nucleus, two approximations can be made as described below.

→ First, omission of the nuclear (N) contribution

For this case it is assumed that the electrons are excited, but the nucleus is fixed. The probability of the transition from Ψ_i to Ψ_f is defined as [84]

$$P_{fi} = \langle \Psi_f | \hat{\mu} | \Psi_i \rangle = \int \Psi_f^* \hat{\mu} \Psi_i d\tau. \tag{2.15}$$

Applying the dipole moment operator (Equation 2.14) in Equation 2.15

$$P_{fi} = \left\langle \Psi_f \left| \left(-e\sum_\varepsilon \hat{r}_\varepsilon + e\sum_N Z_N \hat{R_N} \right) \right| \Psi_i \right\rangle \tag{2.16}$$

$$P_{fi} = \int \Psi_{f,elec}^* \Psi_{f,vib}^* \left(-e\sum_\varepsilon \hat{r}_\varepsilon + e\sum_N Z_N \hat{R_N} \right) \Psi_{i,elec} \Psi_{i,vib} d\tau \tag{2.17}$$

$$P_{fi} = -e\sum_\varepsilon \int \Psi_{f,elec}^* \hat{r}_\varepsilon \Psi_{i,elec} d\tau \int \Psi_{f,vib}^* \Psi_{i,vib} d\tau$$

$$+e\sum_N Z_N \int \Psi_{f,elec}^* \Psi_{i,elec} d\tau \int \Psi_{f,vib}^* \hat{R_N} \Psi_{i,vib} d\tau.$$

Due to the orthogonality, the integral in the second summand is zero over the electronic part. The same can not be considered to the integral over the vibrational term, since

each wavefunction describes solutions of different energy surfaces [84]. Thus, neglecting the nuclear contribution we have

$$P_{fi} = \underbrace{-e \sum_{\varepsilon} \int \Psi_{f,elec}^* \hat{r}_\varepsilon \Psi_{i,elec} d\tau}_{\hat{\mu}_{\varepsilon,fi}} \underbrace{\int \Psi_{f,vib}^* \Psi_{i,vib} d\tau}_{S(\Psi_{vib,f}, \Psi_{vib,i})} \tag{2.18}$$

$$= \hat{\mu}_{\varepsilon,fi} S(\Psi_{vib,f}, \Psi_{vib,i}).$$

The second integral $(S(\Psi_{vib,f}, \Psi_{vib,i}))$ denotes the measure in overlap of the vibrational wavefunctions of the different electronic states. The eletric dipole transition $(\hat{\mu}_{\varepsilon,fi})$ is related to the redistribution of electrons upon interaction with an eletromagnetic wave.

→ **Second, omitting the electronic (ε) contribution**

Here only the nuclear contribution is considered, so the dipole moment operator from Equation 2.14 can be rewritten as [83, 84]

$$\hat{\mu} = e \sum_N Z_N \hat{R}_N. \tag{2.19}$$

Considering the harmonic approximation, the dipole operator can be expanded by a Taylor's series

$$\hat{\mu} = \mu_0 + \sum_{k=1}^{3N-6} \left(\frac{\delta\mu}{\delta Q_k} \right)_0 \hat{Q}_k + ... \rightarrow \mu_k = \left(\frac{\delta\mu}{\delta Q_k} \right)_0. \tag{2.20}$$

Rejecting the terms of higher order and inserting the Equation 2.20 into Equation 2.15 the probability of the transition is describe by

$$P_{fi} = \left\langle \Psi_f \left| \left(\mu_0 + \sum_{k=1}^{3N-6} \mu_k \hat{Q}_k \right) \right| \Psi_i \right\rangle. \tag{2.21}$$

Considering the orthogonality of vibrational wavefunctions, the first term of Equation 2.22 is zero

$$P_{fi} = \underbrace{\mu_0 \langle \Psi_f \Psi_i \rangle}_{=0} + \underbrace{\sum_{k=1}^{3N-6} \mu_k \langle \Psi_f | \hat{Q}_k | \Psi_i \rangle}_{\neq 0}, \tag{2.22}$$

and the second term of Equation 2.22 is non-zero if two conditions are fulfilled [86]; The first condition is that $\mu_k = \left(\frac{\delta\mu}{\delta\hat{Q}_k}\right)_0 \neq 0$, this means that the dipole moment will be affected due to vibrational displacement of the nucleus. The second condition, considering the harmonic approximation, is that the integral must be non-zero, which is respected when the vibrational quantum number changes by one unit ($\Delta\nu = \nu_f - \nu_i = \pm 1$) [86].

2.3 UV/Vis spectroscopy

2.3.1 Steady-state UV/Vis spectroscopy

ChRs are light-gated ion channels from green algae that own a retinal and the LOV domains harbor a flavin mononucleotide (FMN). Both cofactors act as a chromophores. Retinal and FMN absorb visible light that triggers the photocycle of the protein. After excitation the molecules go through electronic transitions that can be investigated by UV/Vis spectroscopy.

The basic idea of a UV/Vis spectrometer is to have a bright polychromatic light source passing a monochromator. The provided light hits the sample and gets absorbed or scattered by the molecules. The light transmitted through the sample is measured by a photomultiplier, which provides the intensity of the light transmitted through the sample (I). According to the Lambert-Beer law (equation 2.23) the measured intensity I is proportional to the initial intensity I_0, the concentration of the sample c, the differential path length dx and a proportionality constant ϵ' [87].

$$\frac{dI_0}{dx} = -\epsilon' I c \tag{2.23}$$

After integration, the absorbance of a material (A) is defined as

$$I = I_0 \exp(-\epsilon_\lambda dc) \rightarrow A = -\log \frac{I}{I_0} \tag{2.24}$$

with absorption $A = cd\epsilon_\lambda$, d is the thickness of the sample and $\epsilon_\lambda = \epsilon'/ln10$ the molar extinction coefficient at a given wavelength λ which is a intrinsic property of the sample.

Figure 2.4 presents the steady state UV/Vis absorption spectra of *CaChR1* wild-type (black) and DsLOV-M49S (blue). *CaChR1* carries a chromophore with an extended
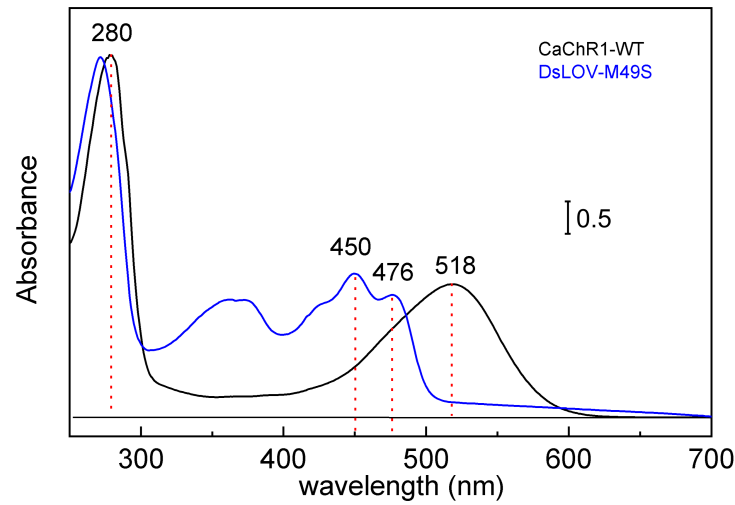
Figure 2.4: UV/Vis absorption spectra of *CaChR1* wild-type (black) and DsLOV-M49S (blue). The maximum absorption of the retinal, FMN and the aromatic amino acids are highlighted with the red dashed line. The DsLOV-M49S spectrum is scaled in relation to the *CaChR1* using the peak ∼280 nm (x1.5).

π-system, providing absorption in the visible range at 518 *nm*. The band at 280 *nm* in the spectra of *CaChR1* and DsLOV-M49S is due to absorption of aromatic amino acids like tyrosin, tryptophan and phenylalanine. Therefore, visible absorption spectroscopy can be used for the quantitative determination of protein concentration.

LOV photoreceptors are characterized by their chromophoric cofactor flavin, which gives rise to the yellow color and three maximum absorption peaks in the UV/Vis absorption spectrum. The DsLOV-M49S absorption in Figure 2.4 shows the typical FMN absorption peak pattern with a maximum at 450 *nm* and a second peak at 476 *nm*, which are correlated to vibronic fine structure [88] and an additional shoulder around 370 *nm*. The characteristics peaks can be related to the well defined binding between the non-covalently bound FMN and the ordered protein structure. The UV/Vis spectra of DsLOV-M49S, *CaChR1* wild-type and variants were measured on our UV-2450 Shimadzu spectrometer. The sample containers were quartz cuvettes ($d = 1$ cm).

2.3.2 Time-Resolved UV/Vis Spectroscopy

During the photocycle the protein and chromophore are subjected to structural and configuration changes that lead to a shift of the absorption maximum. One way to detect these changes over time and to study the different intermediates is via time-resolved UV/Vis spectroscopy. For this purpose, a flash photolysis UV/Vis setup (Applied Photophysics) is used, as schematically depicted in Figure 2.5. The setup contains a pulsed Neodymium doped Yttrium Aluminum Garnet laser (Nd:YAG laser, pulse length: 10 ns) to excite the sample. The laser pulse is set via an optical parametric oscillator (OPO) to a wavelength of 460 nm (DsLOV-M49S). The beam is adjusted to reach the sample with an energy of ~ 3 mJ/cm^2. The second light source presented in the setup is a polychromatic Xenon gas discharge lamp, the Xenon lamp wavelength is selected by a monochromator. For DsLOV-M49S the experiments were performed in the 380 - 730 nm range. A second monochromator is placed behind the sample. For each wavelength the absorbance of the sample is measured over time before and after light excitation. Therefore, the differential absorption can be detected. Experiments are performed on two different time scales: I) a fast time range from 50 ns to 300 μs and II) a slow time range form 30 μs to 10 s. Each kinetic on both time range were collected with 10 average and had been merged to form a broad time range.
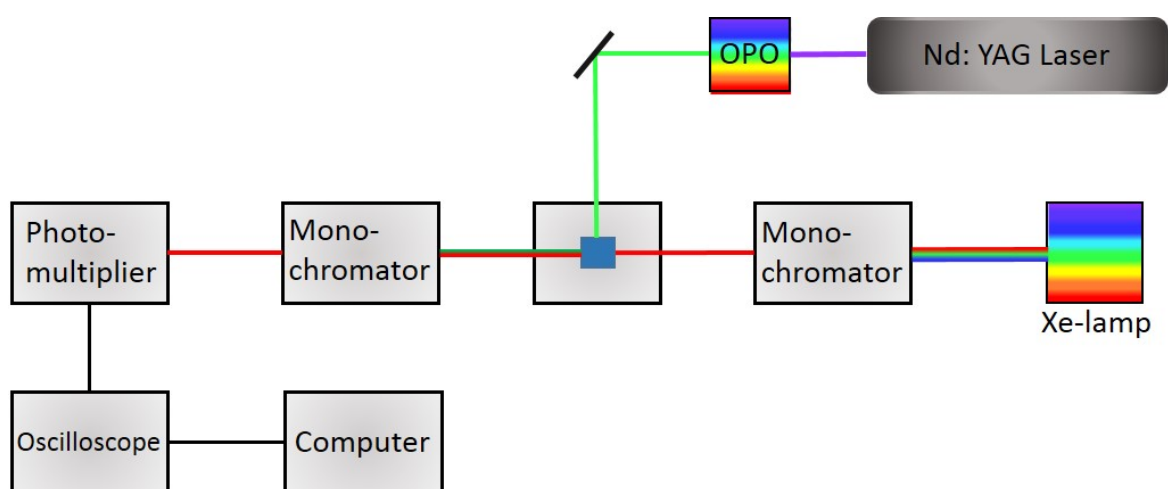
Figure 2.5: Schematic illustration of the flash photolysis apparatus. The sample was excited by a Nd:YAG laser tuned to 460 nm (DsLOV-M49S) by an optical parametric oscillator (OPO). The probing light is emitted by a xenom lamp, which has the specific wavelength selected by a monochromator attached at the lamp. The second monochromator (left) prevents the detection of scattering light from the laser pulse. Time-dependent absorption changes of the sample at different wavelengths is detected with the photomultiplier. Then, the signal get digitized by the oscilloscope and processed by the computer.

2.4 IR Spectroscopy

2.4.1 Vibrational modes in proteins

Infrared (IR) spectroscopy involves the study of the interaction between electromagnetic radiation and matter, as in UV/Vis spectroscopy. IR spectroscopy is a valuable technique from which vibrational modes of a molecule are recorded. The result of the interaction is that energy gets absorbed and vibrations are induced. These molecular vibrations depend on the atomic mass and bond strength between the atoms (Figure 2.3).

The alternating electric field of the incident radiation interacts with the molecules, triggering changes in their dipole moment and consequently alterations in their vibrational or rotational movement giving rise to IR absorption. IR spectroscopy is a sensitive technique, allowing to resolved structural changes of functional groups and properties of hydrogen bonds in molecules. It provides a huge scope of information and application, such as distinguishing protonation dynamics and electronic states, kinetic information, proton transfer reactions, and many more.

Figure 2.6 shows the IR absorption spectra of rehydrated sample films of *CaChR1* wild-type (black) and DsLOV-M49S (blue). The IR spectra are dominated by the C=O and N-H vibrations, the amide A and B bands (around 3300 and 3170 cm^{-1}) correspond to stretching vibrations of N-H (amide A), the amide B correspond to the Fermi-resonance between the stretching vibrations of N-H of amide A. The 3300-3170 cm^{-1} range has also contributions of the O-H stretching vibration of the water. The amide I band (around 1650 cm^{-1}) emerges mainly from C=O stretching vibrations of the protein backbone but it also carries a minor contribution of C-N stretching vibrations and N-H bending (in-plane). The amide II band (around 1550 cm^{-1}) are mainly caused by N-H bending (in-plane) and C-N stretch modes of the backbone. The others two highlighted regions (Figure 2.6) are the C-H stretching (around 2900 cm^{-1})
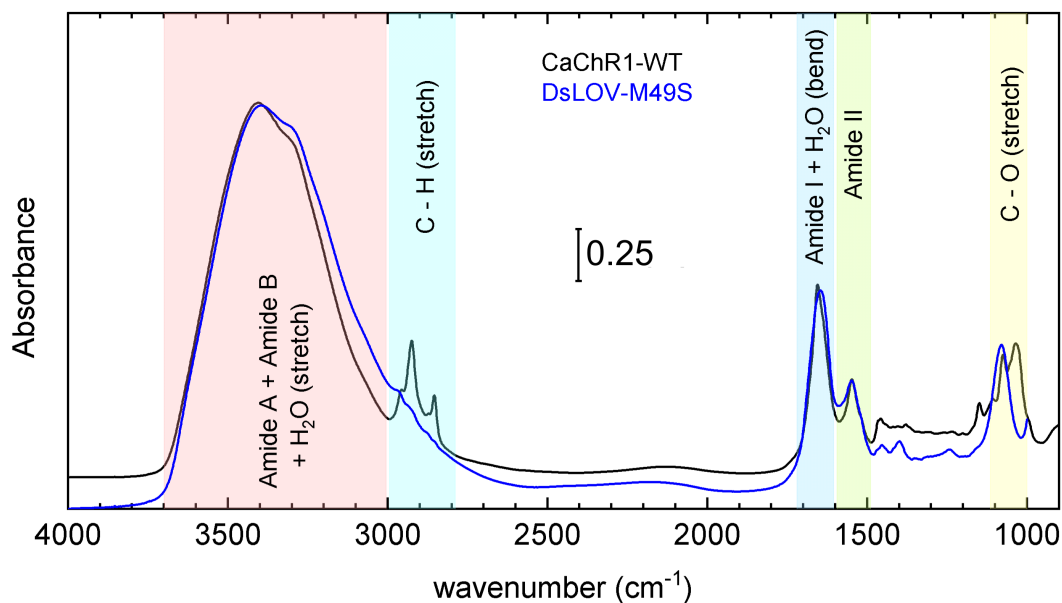
Figure 2.6: FTIR absorption spectrum of rehydrated protein films of *CaChR1* wild-type and DsLOV-M49S recorded in transmission configuration. The main contributions of specific vibrational modes are highlighted. The DsLOV-M49S spectrum was scale in relation to the *CaChR1* using the peak ~ 1650 cm^{-1} (x1.2).

and C-O stretching (around 1100 cm^{-1}). The last one contains the absorption of the protein overlapped with the ones from the environment (detergent in the *CaChR1* case). Besides the protein vibrations, the amide I, amide A and B bands have contribution of the vibrations of the water molecules H_2O bending (amide I) and H_2O stretching (amide A and B).

2.4.2 FTIR spectroscopy

Dispersive elements as prisms or gratings are used in conventional IR spectrometers in order to convert the light from a polychromatic infrared source into a monochromatic probing beam. However, conventional spectrometers have some limitations, which include low signal intensity, poor wavelength precision and low scan speed. More modern constructs instead use a Michelson interferometer (2.7A) as their centerpiece, which greatly improves the measuring capacity of an IR spectrometer [83, 87].

The Michelson interferometer has two plane mirrors, perpendicularly oriented to each other and a beamsplitter (BMS), which splits the IR beam into two parts. The beam is reflected by the stationary mirror and the movable mirror, the movement of the second mirror changes the optical path length of one of the split beams. The two splits beam reflected by the fixed and moveble mirrors are recombined again via the beam splitter causing them to interfere with one another. Changes in the interference pattern are related to differences in the frequency composition of the beam that occur due to constructive and destructive interaction between the two beam signals. This happens due to the relative phase-shift cause by the different optical path of the movable mirror.

After the recombination of the reflected beams at the beamsplitter, the beams are sent to a detector which records an interferogram dependent of the position on the movable mirror β and the frequency of radiation

$$I_{(\beta)} = \frac{I_{(\lambda)}}{2} \left(1 + cos(2\pi \frac{\beta}{\lambda}) \right), \tag{2.25}$$

where $I_{(\lambda)}$ is the intensity of the monochromatic light source. The Equation 2.25 can be generalized for a polychromatic source with a spectral intensity, $I_{(\tilde{\nu})}$, by performing an integral over all the frequencies

$$I_{(\beta)} = \int_{-\infty}^{\infty} \frac{I_{(\tilde{\nu})}}{2} \left(1 + cos(2\pi\tilde{\nu}\beta) \right) d\tilde{\nu}. \tag{2.26}$$

The interferogram is therefore related to the Intensity of a given wavenumber, $\tilde{\nu}$. The Equation 2.26 is known as the cosine Fourier-transform (FT), performing the inverse FT yields the following equation

$$I_{(\tilde{\nu})} = \int_{-\infty}^{\infty} \frac{I_{(\beta)}}{2} \left(1 + cos(2\pi\tilde{\nu}\beta) \right) d\beta. \tag{2.27}$$

For the following steps the constant terms can be neglected, such that the spectrum

$B_{(\tilde{\nu})}$ can be computed from the modulated signal $D_{(\beta)}$ measured at the detector by

$$B_{(\tilde{\nu})} = \int_{-\infty}^{\infty} D_{(\beta)} cos(2\pi\tilde{\nu}\beta)d\beta. \tag{2.28}$$

Looking to the Equation 2.28, it is apparent that a high precision spectrum is achieved if the integral be performed from $-\infty$ to $+\infty$. However, in a real experiment the optical path difference is limited by the maximal mirror retardation ($\Delta\beta = 2\beta_{max}$) that can be considered by using a retardation-dependent boxcar function and the interferogram can be multiplied by a function $A_{(\beta)}$, which is zero for the follow conditions $-\infty < \beta < -\Delta\beta$ and $+\Delta\beta < \beta < +\infty$. Thus the Equation 2.28 can be rewritten as

$$B_{(\tilde{\nu})} = \int_{-\infty}^{\infty} A_{(\beta)} D_{(\beta)} cos(2\pi\tilde{\nu}\beta)d\beta. \tag{2.29}$$

Due to the finite retardation, the interferogram is truncated. Mathematically this process is equivalent to multiplying the real (infinite) interferogram with a boxcar function that would generated error in the resulting spectrum and broaden the spectrum with side-lobes. We can see this effect in Figure 2.7B, which shows the FT of a boxcar function for $-\Delta\beta < \beta < +\Delta\beta$. In order to reduce the amount of secondary ripples in the interferogram, one can apply an empirical apodization function for $A_{(\beta)}$. This process helps to weight the points collected in the interferogram, smoothly decaying the interferogram to 0 at both extremities. Different apodization functions have individual characteristics that can strongly help to reduce the sidelobes but consequently decrease the spectral resolution as well [89–91].

For the data acquisition in a real experiment, the range of resolved frequencies can be determined by the Nyquists criterion, which tells us that discretization of the interferogram means that the highest detectable wavenumber will be limited by the step-size of the movable mirror x

$$\tilde{\nu}_{max} = \frac{1}{2\Delta x}. \tag{2.30}$$

The mirror position is determined using a Helium-neon laser (633 nm) which is coupled parallel to the IR beam and detected by a separate photodiode.

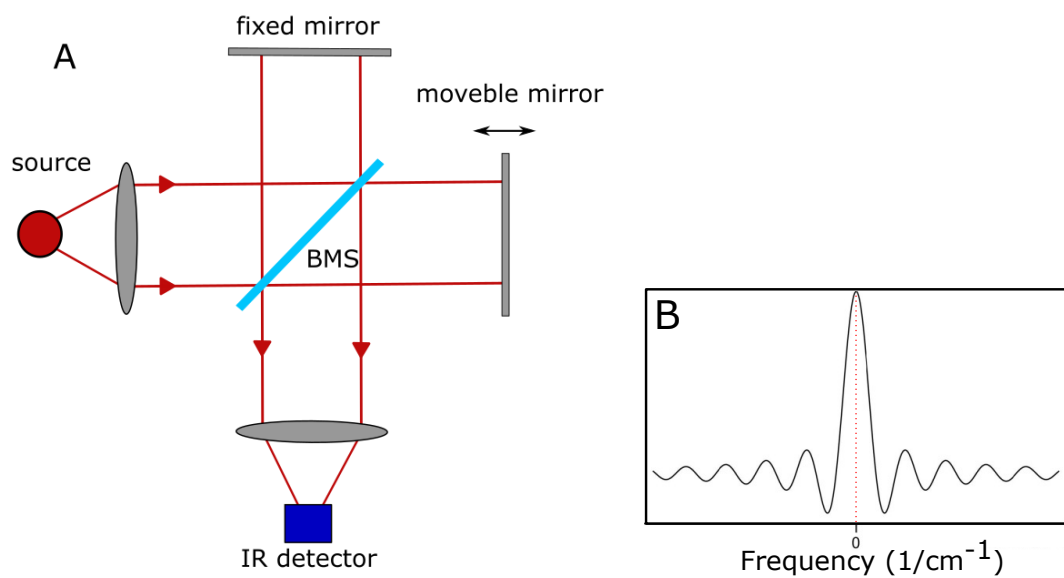

Figure 2.7: (A) Schematic representation of Michelson interferometer in a FTIR spectrometer. The interferometer contains a static and a moveable mirror, a beam splitter (BMS) and a infrared source. (B) Fourier transform of a boxcar function.

2.4.2.1 Light-induced FTIR difference spectroscopy

Difference spectroscopy is applied in order to observe vibrational differences between the dark (ground) state and the light intermediate states of the photocycle. The change in absorption in a light-induced FTIR difference experiment is given by equation 2.24, where I_0 is the single channel of the dark state and I is the single channel of the photostationary mixture. All samples were prepared in a transmission cell as described in section 2.1. The rehydrated sample of DsLOV-M49S was kept in the dark for 4 s followed by 3 s continuous illumination with an LED emitting at a central wavelength of 450 nm (10 mW/cm^2). The rehydrated samples of *CaChR1* wild-type and variants were kept in the dark for 5 s followed by 5 s constinuous illumination with an LED emitting at a center wavelength 530 nm (10 mW/cm^2). 3000 co-additions were recorded using a FTIR spectrometer Vertex 80v (Bruker) with a spectral resolution of 2 cm^{-1}.

2.4.3 Time-Resolved IR spectroscopy

2.4.3.1 Rapid-Scan FTIR spectroscopy

The rapid-scan method of FTIR spectroscopy has a time resolution limited by the forward and backward speed of the movable mirror which is 10 ms in the spectrometer used in this work. The rapid scan experiment was performed on DsLOV-M49S using the commercial IFS 80v spectrometer (Bruker). The rehydrated sample at ∼24 °C was excited every 10 s with a 10 ns blue laser (460 nm) pulse from an optical parametric oscillator (OPO) driven by the third harmonic of a Nd:YAG laser with energy between 2.5 - 3 mJ/cm^2. To improve the signal-to-noise ratio, the data collection process was repeated 500 times with a spectral resolution of 4 cm^{-1}. The data was analyzed using singular value decomposition (SVD) [81].

2.4.3.2 Time-Resolved IR spectroscopy with Quantum Cascade Laser

Rapid scan is a time-resolved method which provides information in the *ms* time range. However, we are also interested in resolving the protein photocycle in the *n*s to *μ*s time regime that also has processes involving the protonation, deprotonation and changes in the H-bonds of the protein amino acids. To achieve a higher time resolution compared to the rapid scan method, the time-resolved IR spectroscopy method was applied in which a external cavity quantum cascade laser (EC-QCL) serves as a monochromatic probing light source (Faist, Capasso et al. 1994 [92] and Schultz et. al. [80]). Time-resolved IR spectroscopy using tunable EC-QCLs was performed on a home-built spectrometer (built and improved by *Bernd Schultz* and *Pit Langner*, respectively). Figure 2.8 shows the scheme of the time-resolved IR experiment setup.

The continuous monochromatic emission of EC-QCLs is directed through the rehydrated sample in a transmission cell, which is excited by a pulsed Nd:YAG laser (Minilite II, Continuum) with green-light for *CaChR1* ($532\ nm$) and by a pulsed blue-light to DsLOV-M49S ($460\ nm$ - OPO pumped with a Quanta-Ray Nd:YAG, Spectra-Physics), the energy of the laser intensity were kept between $2.5 - 3\ mJ/cm^2$. The absorption kinetics of individual wavenumbers in the time range of $500\ ns$ - $500\ ms$ are recorded by means of a MCT detector (KV104 Series, 50 MHz). The detector output is amplified and divided into two separate channels, which are digitized by picoscopes. The picoscopes are running in different sampling frequencies a fast at 250 MHz and a slow at 1 MHz. The higher light intensity of the quantum cascade laser ($\leq 300\ mW$) compared a globar used in FTIR spectrometers leads to a better signal-to-noise ratio [80]. However, a disadvantage in using EC-QCL is the small spectral range of emission. To cover a broad spectral range, four different EC-QCL during data collection were used, for the S-H vibrational range an EC-QCL covering 2600-2500 cm^{-1}, for the carboxyl (C=O) vibrational range an EC-QCL covering 1700 - 1630 cm^{-1}, for the amide I vibrational range an EC-QCL covering 1700 - 1630 cm^{-1} and for the amide II vibrational range

an EC-QCL covering 1640 - 1510 cm^{-1}. A step size of 2 cm^{-1} was chosen for the 1690-1510 cm^{-1} vibrational range and 1 cm^{-1} for the S-H and carboxyl vibrational ranges. The rehydrated films of DsLOV-M49S, *CaChR1* wild-type and variants were excited every 4*s* (DsLOV-M49S) or 3 *s* (*CaChR1* wild-type and variants) with 100 average for each kinetic. The analysis of the time-resolved IR data were performed using singular-value-decomposition analysis (SVD) [93] and lifetime-density analysis (LDA) [94].
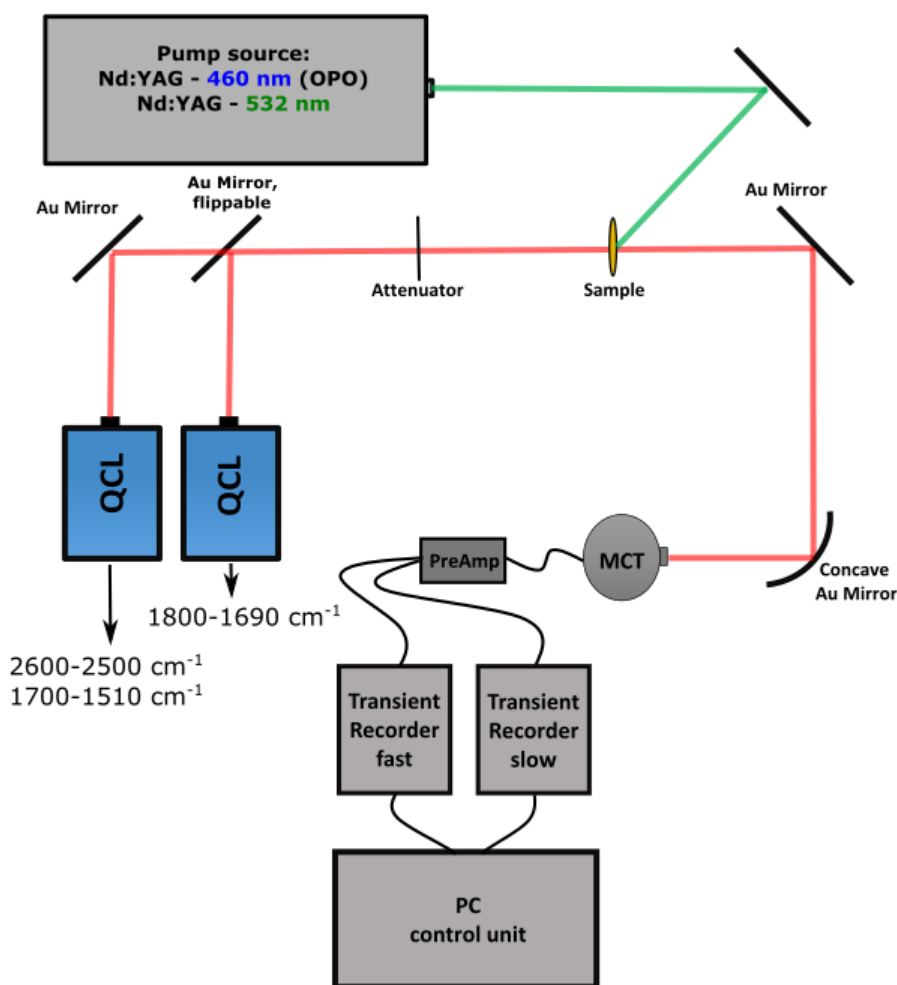
Figure 2.8: Schematic illustration of the home-built time-resolved IR spectrometer using EC-QCLs. The 2600-2500 cm^{-1}, 1800-1690cm^{-1} and 1700-1510 cm^{-1} frequencies regions were measured with differents EC-QCLs. Tunable QCL run in continuous mode at a specific wavenumber. The samples in a transmission cell were excited with a Nd:YAG laser that was tuned by an OPO to 460 *nm* (DsLOV-M49S) and with a minilite at 532 *nm* (*CaChR1* wild-type and variants), the transmitted intensity signal is collected by a MCT detector.

2.4.3.3 Intrinsic noise of the Quantum Cascade Laser

The use of QCLs as light sources in time-resolved IR spectroscopy allow the measurement of larger absorbances, resulting in larger difference signals. This is usually achieved by using a highly concentrated sample, leading to a larger path length for the probing beam. It was show by Schultz et. al. [80] that the intrinsic noise level of individual QCL heads can diverge. Thus, depending on the data set wavelength range, the number of averages necessary to achieve a good signal-to-noise ratio can greatly increase.

In conventional FTIR spectroscopy, the noise is detector-limited, thus the incoming photon flux and the signal-to-noise ratio scales linearly. On the other hand, the time-resolved measurements which use the QCL set-up are not limited by noise from the detector, rather the intrinsic noise in the QCL caused by fluctuations in the output power [80]. It was suggested that the QCL's intrinsic noise can vary at different emission frequencies, giving the power emission spectrum a Gaussian shape. This leads to the conclusion that QCLs perform poorly when operating at the edges of their tuning range, which results in increased output noise and decreased output intensity at these frequencies.

Similar investigation presented by Ref. [80] was performed for our QCL with emission frequencies in the 2600-2500 cm^{-1} range. The single shots kinetics of 2544, 2560 and 2570 cm^{-1} wavenumbers for the picoscopes sampling at 250 MHz and 1 MHz are presented in Figure 2.9, all the kinetics feature similar behaviour. Figure 2.10 show the zoom in of the single shots kinetics, here we can see oscillations over the kinetics for both picoscopes, which are also printed in the zero-line kinetics show in Figure 2.11.

Figure 2.11 show the zero-line of the 2544, 2560 and 2570 cm^{-1} kinetics, illustrating the performance of the QCL in the 2600-2500 cm^{-1} range under conditions that minimize the oscillations and intrinsic noise. The data collected by the picoscopes 1 (250 MHz) and 2 (1 MHz) are shown before the merge, for 1 and 100 acquisitions (top and lower panel, respectively). It is clear that collecting each kinetic 100 times and averaging them
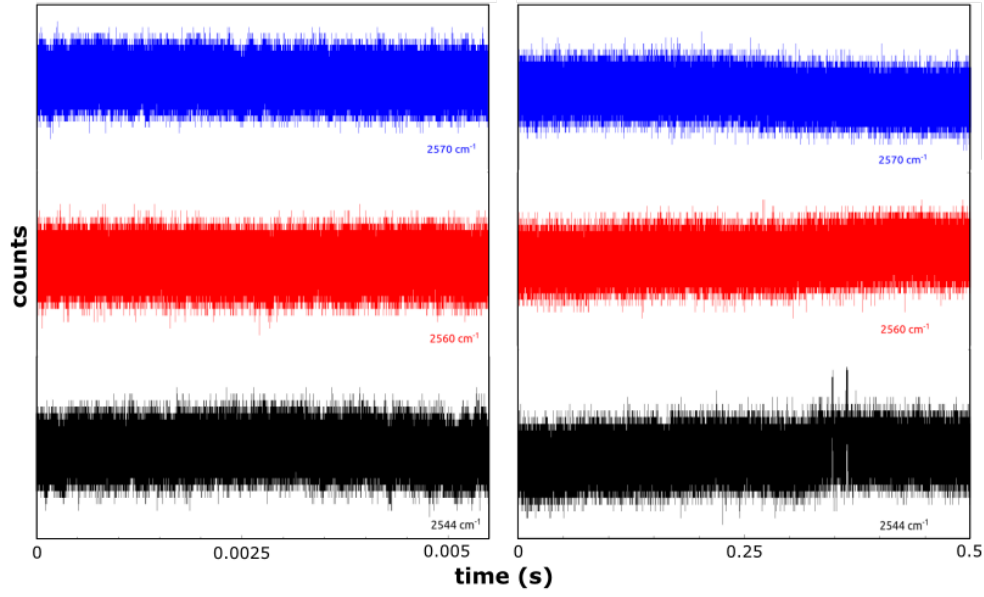
Figure 2.9: Single shots kinetics at different emission wavenumbers of the 2600-2500 cm^{-1} QCL, collected by a picoscope running in 250 MHz (fast times - left panel) and in 1 MHz (long times - right panel) sampling frequencies. The kinetics were collected using a BR sample.
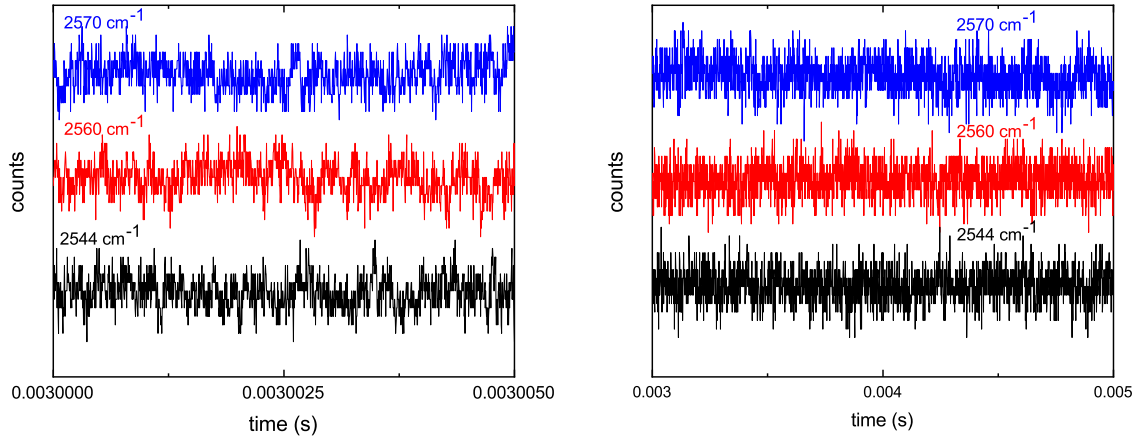
Figure 2.10: Zoom in of the single shots kinetics at different emission wavenumbers of the 2600-2500 cm^{-1} QCL. The time range cover from 3 to 3.005 ms for the 250 MHz picoscope (fast times - left panel) and from 3 to 5 ms for the 1 MHz picoscope (long times - right panel) sampling frequencies. The kinetics were collected using a BR sample.

across the number of acquisitions, significantly improves the signal-to-noise ratio for both picoscopes. However, despite averaging 100 acquisitions we can still see oscillations in the kinetics (Figure 2.11) which suggests that they can be interpreted as an artifact.

To demonstrate the final performance of the QCL (2600-2500 cm^{-1} range), Figure 2.12 show the average of the data points of the raw data of CaChR1 wild-type from 1 to 2.6
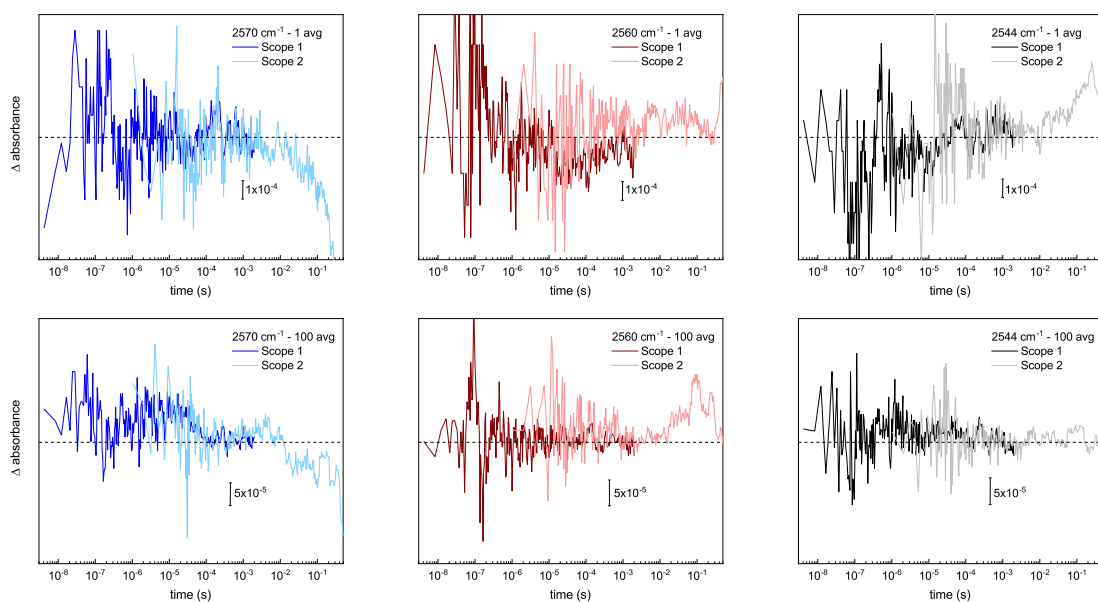
Figure 2.11: Zero-line kinetics at 2570, 2560 and 2544 cm^{-1} emission frequencies. The top graphics are kinetics for 1 average and the bottom for 100 average. The data collected by the picoscopes 1 (250 MHz) and 2 (1 MHz) are show before the merge. The kinetics were collected using a BR sample.

ms and the fit provided by global analysis at 1.8 ms.
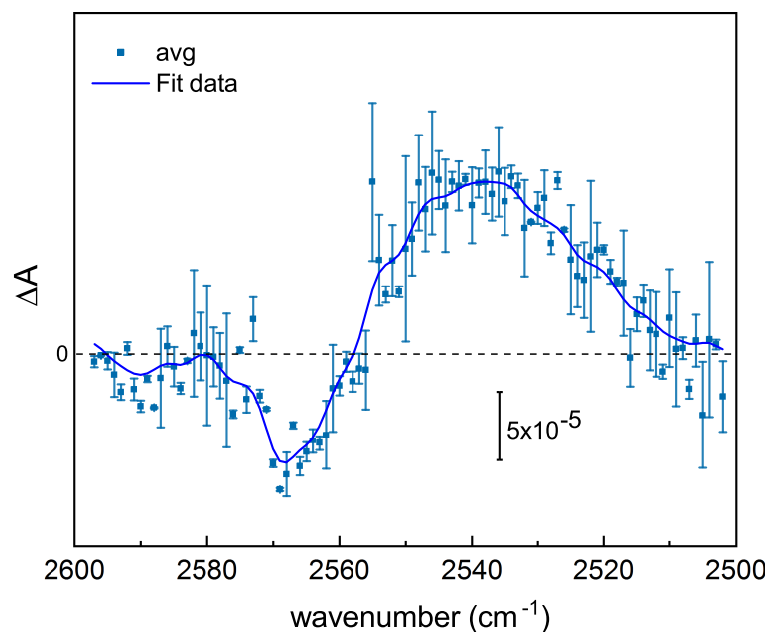
Figure 2.12: *CaChR1* wild-type raw data and fit provided by global analysis at 1.8 ms. The standard deviation was calculated by averaging the data points from 1x10^{-3} to 2.6x10^{-3} seconds in the 2600-2500 cm^{-1} range. The sample was excited at 532 nm and has spectral resolution of 1 cm^{-1}.

Results

3.1 Light Induced FTIR spectroscopy on wild-type CaChR1

During the last few years several studies trying to explain the molecular changes during the photocycle of *CaChR1* have been conducted. These were performed using several different experimental techniques such as FTIR difference spectroscopy [36, 39, 40], Resonance Raman [34, 35], UV/Vis spectroscopy [33, 38]. However, the proton transfer pathway of *CaChR1* is still unknown, which is in part due to the unusually high number of cysteine residues present in *CaChR1* (14 cysteine amino acids) compared to other rhodopsins. So far, no studies have shown an extensive time-resolved investigation focusing on variants with site-specific amino acids exchange. Therefore, in this work a detailed investigation in the *CaChR1* photocycle was made, with an intense mutational analysis focusing on the Cys, Asp and Glu residues near the retinal of the protein. Here the discussion of the light induced data of *CaChR1* wild-type is shown. The light induced data of *CaChR1* variants and time-resolved data of *CaChR1* wild-type and variants will be discussed in the next sections.

Under green-light illumination the *CaChR1* wild-type transitions from the ground (closed) state to the long-lived intermediate (open) state. Electromagnetic excitation

induces changes in the electronic structure at the protein's molecular level. These variations result in a change in dipole moment which is manifested as an alteration in the vibrational pattern of the molecule. These alterations can be detected by light-induced FTIR difference spectrocopy.
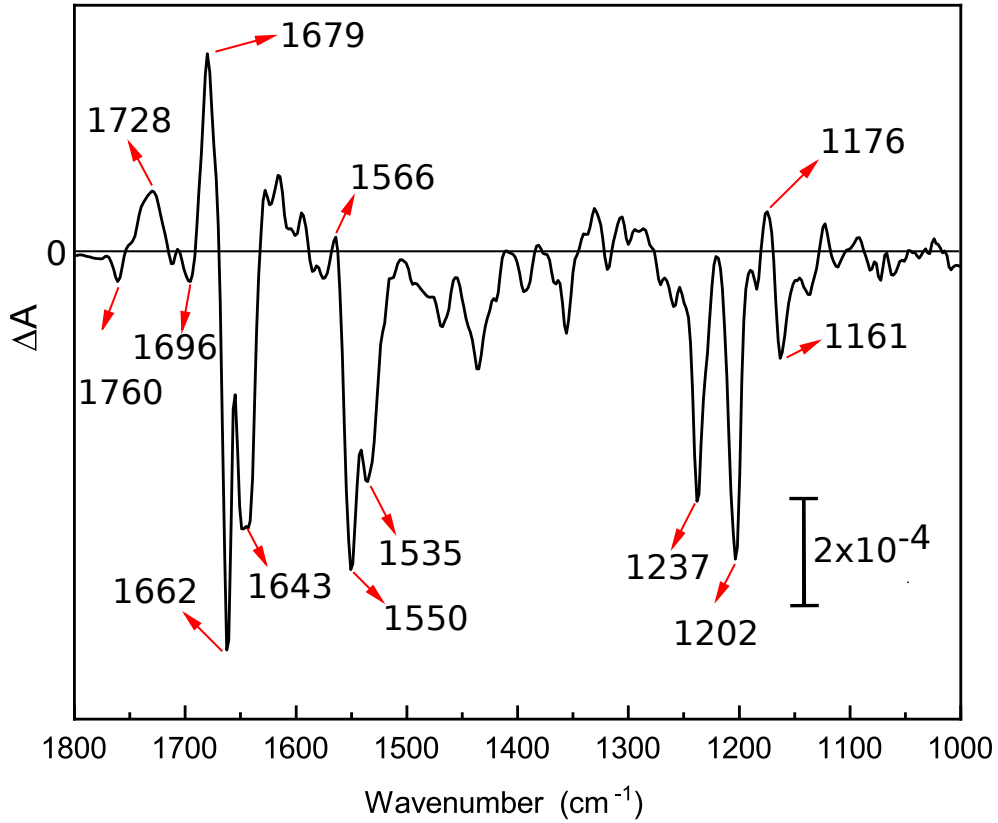
Figure 3.1: FTIR difference spectrum of the light state versus the dark state of *CaChR1*. The spectrum was recorded at 24 °C under continuous illumination with a LED emitting maximum at 530 nm.

Figure 3.1 shows the light-induced FTIR difference data of the *CaChR1* wild-type in the 1800-1000 cm^{-1} range. The negative bands originate from the dark state and the positive represent vibrational bands from the light-induced intermediate state [35, 36, 40]. The light-induced FTIR spectrum (Figure 3.1)) of *CaChR1* wild-type accumulates predominantly the P$_2^{380}$ intermediate state with a minor contribution of P$_4^{520}$ [34–36, 39, 40, 95]. The P$_2^{380}$ state represents the open state of *CaChR1* wild-type, implying that cations are translocated across the membrane along the concentration gradient. The observed difference bands are indicative of changes in the eletronic

structure of the retinal chromophore and conformational changes of the surrounding apo-protein [96].

In the 1260-1100 cm^{-1} spectral range the bands of the C-C stretching vibrations in the retinal chromophore can be found. Here three negative modes are found at 1161, 1202 and 1237 cm^{-1} and assigned to C-C stretching vibrations of the all-*trans* retinal [97–99]. In this range only a small positive mode at 1176 cm^{-1} is found. The absence of a stronger positive band at this region suggests there is a predoment accumulaton of an intermediate state with deprotonated retinal Schiff base [35, 100, 101].

Previously, Resonance Raman spectroscopy applied to the retinal of the *CaChR1* wild-type identified the presence of three coupled ethylenic modes at 1548 cm^{-1}, 1533 cm^{-1} and 1525 cm^{-1} (C=C stretching) [34, 35]. Two of these modes are found in the FTIR difference spectrum with a small shift [35], (-)1550 cm^{-1} and (-)1535 cm^{-1} (Figure 3.1). Here, the band at (-)1535 cm^{-1} represents the ethlylenic vibration in the configuration of all-*trans* retinal with protonated Schiff base [35]. Close to the ground state frequency of the ethylenic stretch a small positive mode at 1566 cm^{-1} is identified, which has been assigned as the ethylenic stretch mode in the P$_2^{380}$ intermediate state [35, 40] in the configuration of 13-*cis* retinal with a deprotonated Schiff base [35]. The presence of the (+)1566 cm^{-1} band supports the suggestion that the P$_2^{380}$ intermediate state is the dominant contribution of the FTIR difference spectrum [35, 40]. The (-)1550 cm^{-1} band can be assigned to the C=C ethylenic vibrations of 13-*cis* retinal [35, 36] with contributions of the amide II vibrations (N-H bending and C-H stretching of α-helices) [36, 39, 40].

In the 1680-1620 cm^{-1} vibrational range bands are found at (-)1662 cm^{-1}, (+)1679 cm^{-1} and (-)1628 cm^{-1}, assigned to amide I vibrations due to C=O stretching of the peptide bond [36, 102]. The (-)1662 cm^{-1} mode falls into a typical vibrational frequency for transmembrane helices [103, 104]. A negative band in a similar position was also observed in the P$_3^{520}$ intermediate (open) state of *CrChR2* [37, 105]. The (+)1679 cm^{-1}

mode is unique to *CaChR1*, the presence of this characteristic band supports the idea that the structural changes arising in the *CaChR1* and *CrChR2* proteins upon light activation differ slightly [35]. The (+)1679 cm^{-1} band together with changes in the amide II vibrational range could indicate structural changes in the protein backbone between the ground state and the light induced intermediate states [34, 39, 40].

In the carboxylic vibrational range (1780-1690 cm^{-1}) the C=O stretching vibrations mainly from the Asp and Glu residues (Figure 3.2a) are present. In the P$_2^{380}$ intermediate state (Figure 3.2a) three negative modes at 1760, 1711 and 1696 cm^{-1} and three positive overlapping modes at 1751, 1740 and 1728 cm^{-1} are found. These vibrational modes might arise from changes in the carboxyl amino acid side chains, such as a protonation and deprotonation of the Asp/Glu residue and consequent changes in the H-bonding [35, 36, 39, 40].
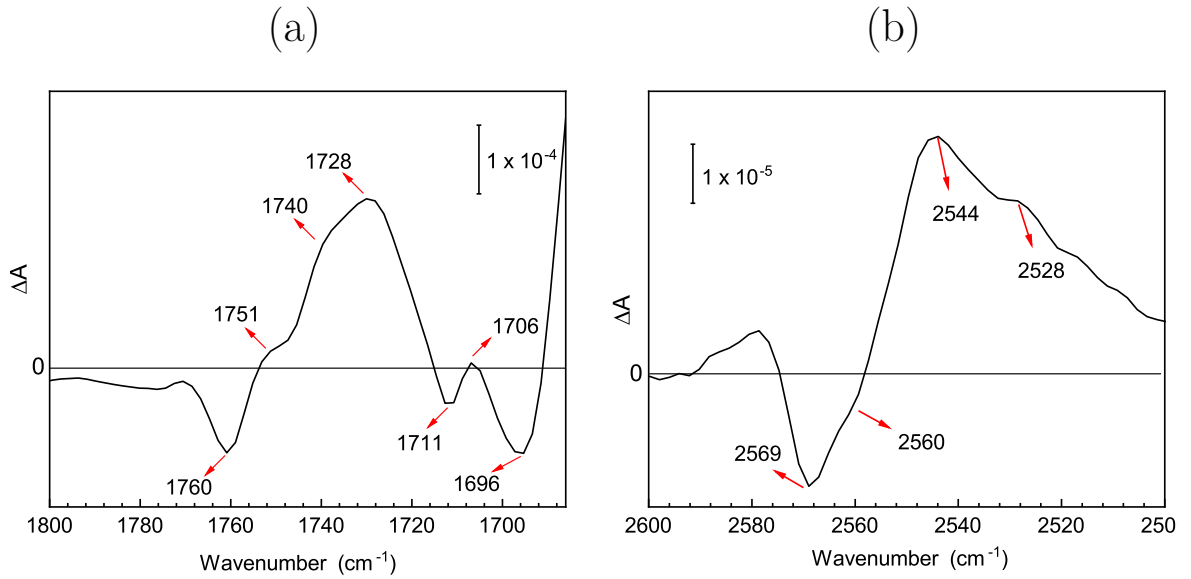
Figure 3.2: Light induced FTIR difference spectrum of *CaChR1* wild-type in the (a) carboxylic region from 1800-1690 cm^{-1} (C=O) and (b) the cysteine region from 2600-2500 cm^{-1} (S-H).

Proteins that carry a cysteine residue can show characteristic vibrational modes in the 2600-2500 cm^{-1} range, originating from changes in the protonated state of the cysteine or due to alterations of its hydrogen bonding [106]. Figure 3.2(b) shows the S-H stretching vibration from the thiol group. S-H vibrations are widely used investigative

tool [107, 108] and have a similar behaviour to the O-H stretch, which shifts to lower wavenumbers when acting as an H-bond donor. When studying the cysteine S-H group proton bonding, a band at 2585 cm^{-1} is expected for non-hydrogen-bonded, 2580-2575 cm^{-1} for weak H-bonded, 2575-2560 cm^{-1} for moderate H-bonded and finally 2560-2525 cm^{-1} for strongly H-bonded [107, 108]. The S-H vibrational range of *CaChR1* have already been show by the Ref. [36], but no band assignment has been discussed yet.

The light-induced FTIR difference spectrum of Figure 3.2(b) shows the presence of a negative mode at 2569 cm^{-1} and a shoulder at 2560 cm^{-1}. The positive band at 2544 cm^{-1} has a stronger intensity than the negative vibrational bands. Here, the S-H vibrational frequency is downshifted by 25 cm^{-1} [36]. This shift is not unique to *CaChR1*, similar behaviour was also observed for other proteins like *Neurospora* rhodopsin [109], *Anabaena* sensory rhodopsin [110] and C1C2 chimera [111]. The changes of the S-H frequency may occur due to changes in the intensity of the H-bond that can be formed via intra-helical (H-bond with the oxygen atom of the backbone positioned in the same helix) or inter-helical (H-bond with a side chain positioned in another helix) bonding [112, 113]. Another possibility for the appearance of the S-H absorption bands is due to the protonation or deprotonation of one or more cysteine residues. This suggestion will be further addressed in the discussion of *CaChR1* variants in Chapters 3.2 and 3.4. The band assignment for the carboxylic region and the S-H vibrational range (Figure 3.2b) will be discussed further with the help of *CaChR1* variants.

3.2 Light Induced FTIR spectroscopy on CaChR1 variants

To perform the band assignment of the *CaChR1* wild-type and address molecular changes arising after green-light excitation, FTIR difference spectroscopy on *CaChR1* variants was performed [35, 36, 39, 40]. Thus, an extensive mutational analysis on variants with site-specific amino acid exchanges with focus on Cys, Asp and Glu residues will be discussed (Figure 1.3). The band assignment of the *CaChR1* wild-type using the variants D299N, D299E and E169Q was previously discussed by Muders [33] and Ogren et. al. [39, 40]. However, even with intense investigation in *CaChR1* variants (D299N, D299E and E169Q), these studies were not able to complete the identification of the amino acids involved in the protonation and deprotonation steps during the photocycle. Together with *Maria Walter* we have expanded the number of *CaChR1* variants investigated using light-induced FTIR spectroscopy.

Below, the vibrational analysis of Cys, Asp and Glu variants (Figure 3.3: E136Q, D299N, D299E and E169Q; Figure 3.4: D202N, C174T, C173T and C173/174T) in the 1700-1000 cm^{-1} range will be presented. Subsequently, the discussion is focussed on the C=O (1800-1690 cm^{-1}) and S-H (2600-2500 cm^{-1}) vibrational ranges.

3.2.1 1800-1000 cm^{-1} Vibrational Range

The C-C bands (1163-1237 cm^{-1} - wild-type) of the coupled vibrations of the polyene backbone of the retinal are defined as the region of the retinal fingerprints [114]. Part of these vibrational modes are present in IR [36, 40] and Raman [35, 36] data. In Section 3.1 the wild type fingerprint bands are discussed. These are assigned to the all-*trans* retinal in the ground state and are marked by three negative modes at 1237, 1202 and 1163 cm^{-1}. Beside these bands, Bergo et. al. [115] and Kawanabe et. al. [110]

identified two other vibrational modes in the fingerprint region. The *CaChR1* wild-type spectrum shows a negative shoulder at $\sim$1230 cm^{-1} and a narrow negative mode at $\sim$1183 cm^{-1}.

Similar C-C vibrational modes are also visible in the fingerprint range of all variants with possible overlaps by other bands. The spectra of the variants were scaled by the retinal mode at (-)1237 cm^{-1} in relation to wild-type. In some variants the 13-*cis* photocycle is more easily excited, thus yielding a larger proportion of the all-*trans* retinal in the detected spectra. Thus, scaling the data in accordance to the band at (-)1237 cm^{-1} may be unfavorable to the variants with this behaviour making the band assignment difficult. This difficulty means that the final band assignment can only be elucidated using time-resolved spectroscopy.

In the E136Q variant (Figure 3.3 - second spectrum) the fingerprint range is similar to the wild type, except for the positive mode at 1174 cm^{-1}, which is slight stronger in E136Q. In the subsequent variants D299N, D299E and E169Q (Figure 3.3) and in C174T (Figure 3.4) the (+)1174 cm^{-1} band is not recognizable, suggesting that exclusively the P_2^{380} intermediate state is accumulated in these variants [40]. On the other hand, in the difference spectra of the D202N, C173T and C173/174T variants (Figure 3.4) the (+)1174 cm^{-1} band has more intense signal than in the wild type spectrum, suggesting stronger influences of the P_4^{510} intermediate.

The D299N, D299E and E169Q variants (Figure 3.3) present a slight down-shift in the (-)1202 cm^{-1} band. The mode at (+)1221 cm^{-1} is more pronounced in the D299N, E169Q, D202N, C174T and C173/174T variants than in the wild type. For all variants the small mode at (-)1183 cm^{-1} is more pronounced in comparison to the wild type spectrum, the largest difference is found for C173/174T variant. The same effect is observed in the (+)1276 cm^{-1} band for the D202N and C173/174T variants.

In the 1690-1600 cm^{-1} range, the variants show large differences compared to the wild type, exhibiting a complex band pattern (Figure 3.3 and 3.4). Major changes are

observed in the modes at ∼1650/1653 cm^{-1} and (-)1662 cm^{-1}. The (-)1662 cm^{-1} band loses intensity in all the variants, except for E136Q and D299E, which show the opposite behavior. Changes in these bands could indicate changes in the hydrogen-bonds of the peptide backbone of α-helices due to hydration and/or conformational changes.
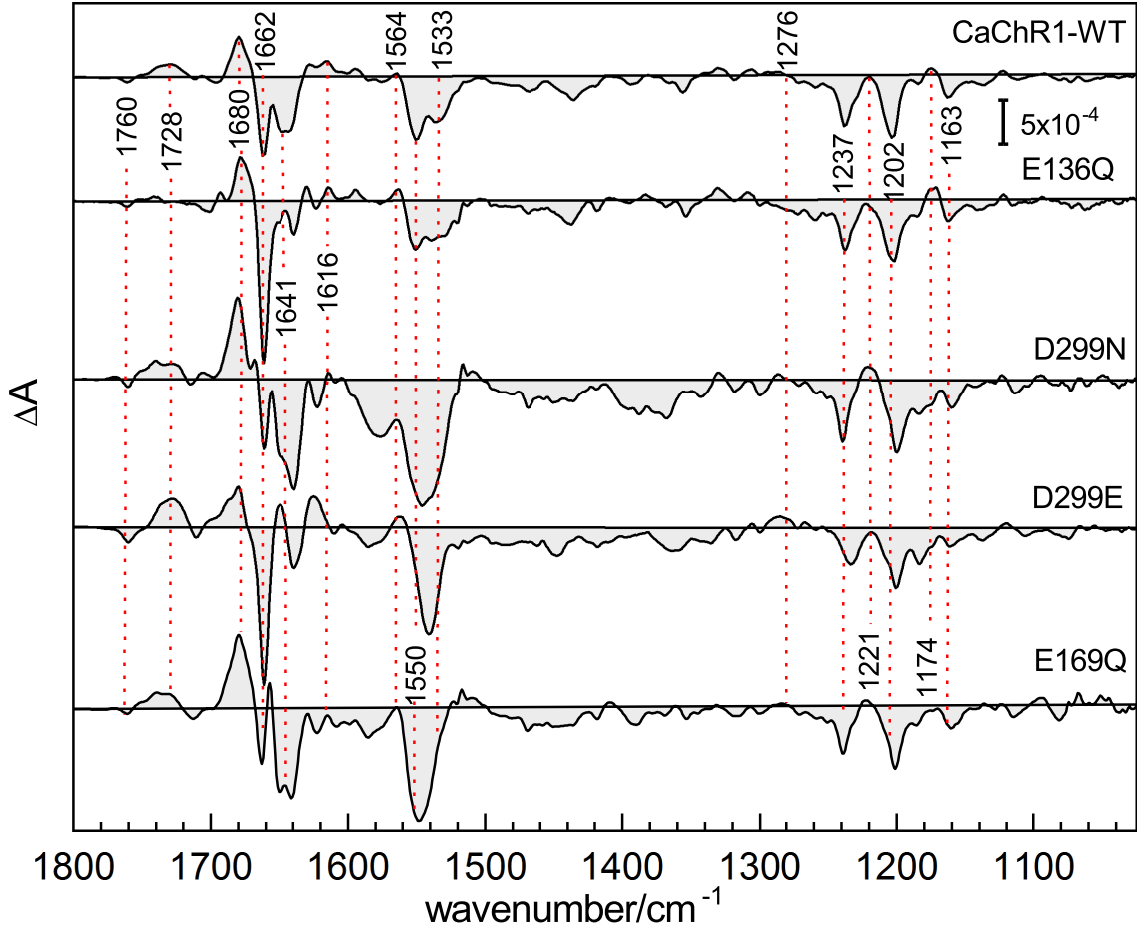
Figure 3.3: Light-induced FTIR of *CaChR1* wild-type and variants E136Q, D299N, D299E and E169Q in the 1800-1000 cm^{-1} range. The spectra of the variants were scaled to the retinal band at 1237 cm^{-1} of wild-type. The spectra were recorded at 24 °C under continuous illumination with a LED emitting maximum at 530 nm.

In the amide II and C=C stretching vibrational range (1600-1500 cm^{-1}) most of the variants show a band pattern strongly deviating from that of the wild type. The E136Q variant displays vibrational bands at the same position as the wild type and with similar intensity. One exception is the (-)1533 cm^{-1} band, which is broader and weaker than in the wild type spectrum. Similar behaviour is also observed to C174T (Figure
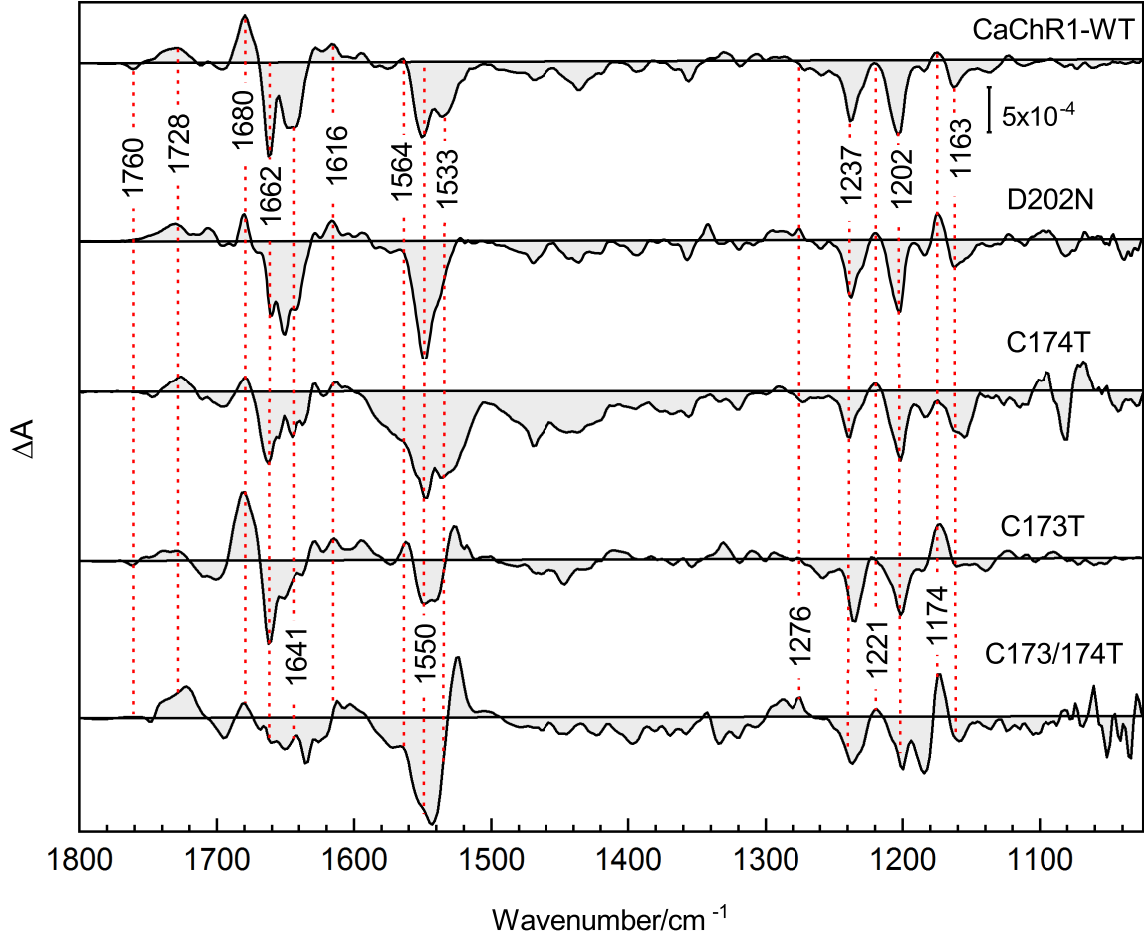
Figure 3.4: Light-induced FTIR of *CaChR1* wild-type and variants D202N, C174T, C173T and C173/174T in the 1800-1000 cm^{-1} range. The spectra of the variants were scaled to the retinal band at 1237 cm^{-1} of wild-type. The spectra were recorded at 24 °C under continuous illumination with a LED emitting maximum at 530 nm.

3.4), but for C174T the (-)1550/(-)1533 cm^{-1} bands are stronger than wild-type. All the other variants show similar changes in the (-)1533 cm^{-1} mode, which shifts to higher frequencies and overlaps with (-)1550 cm^{-1}. The spectra show a broad negative vibrational mode with minimum around 1548 cm^{-1}, except for D202N which shows a sharper band than that of the wild type. Only D299E (Figure 3.3) and C173T (Figure 3.4) present a stronger (+)1564 cm^{-1} mode in comparison to wild-type, also the (+)1522 cm^{-1} band is strongly accentuated in the C173T and C173/174T variants.

A notable feature can be observed when taking into account the changes observed in the bands around (-)1533/(+)1524 cm^{-1} of the C173T and C173/174T variants,

together with the changes observed in the vibrational modes of the C-C stretching range. This may be indicative of an intermediate state with a protonated Schiff base and a red-shifted absorption maximum in the C173T and C173/174T variants when compared to the wild type. The changes observed at (+)1174, (+)1221 and (-)1237 cm^{-1} in D202N suggest a stronger 13-*cis* photocycle than that of the wild type, similar assignments were observed for the variant E123T of *CrChR2* [114]. The absence of the (+)1174 cm^{-1} band in the difference spectra of D299N, D299E, E169Q and C174T variants suggests that exclusively the P_2^{380} intermediate state is accumulated for these variants without the influence of the P_4^{510} intermediate.

3.2.2 Carboxylic (C=O) Vibrational Range

In this section, the bands of the C=O vibrational range are assigned, allowing the identification of the amino acids responsible for protonation and deprotonation during the photocycle. As stated previously, the mutation were made using only conservative replacements, which means that the carboxylic end group of Asp and Glu residues were replaced by their corresponding Asn and Gln (Figure 3.5(a) - E136Q, D299N, E169Q and Figure 3.5(b) - D202N), with the exception of D299E (replaced Asp to Glu). Thus, the length of the amino acids are maintained but the ability of the protonation or deprotonation function is suspended. In addition to the carboxylic variant D202N, Figure 3.5(b) also shows the FTIR difference spectra of the cysteine variants C174T, C173T and C173/174T in the C=O vibrational range.

As already discussed in section 3.1, the light-induced FTIR difference spectrum of the *CaChR1* wild-type (1800-1680 cm^{-1} range) is mainly formed by four positive vibrational modes at 1704, 1728, 1740 and 1751 cm^{-1} and three negative vibrational modes at 1698, 1711 and 1761 cm^{-1}.

The variants with the strongest differences in relation to the *CaChR1* wild-type spectrum are those upon mutation of Glu to Gln (E136Q) and Asp to Asn (D202N), as shown in the second top spectra in Figure 3.5(a) and 3.5(b) respectively. In the E136Q variant, the positive mode at 1728 cm^{-1} is invisible when compared to the *CaChR1* wild-type (top spectrum Figure 3.5(a)). The negative mode at 1760 cm^{-1} and the two positive shoulders at 1748 and 1740 cm^{-1} remain in the same position and with similar intensity as the wild type spectrum. At a lower spectral range, a strong negative mode at 1703 cm^{-1} and a positive mode at ~1693 cm^{-1} are observed in the spectrum of E136Q. These bands could originate from the C=O stretching vibration due to the amino acid exchange, from Glu to Gln, providing possible changes in the hydrogen bonding. Here, due to the missing of the (+)1728 cm^{-1} band we can suggest that the E136 amino acid is a proton acceptor during the *CaChR1* photocycle. Thus, E136 might be deprotonated

in the dark state and protonated in the open conductive state (P_2^{380} intermediate), presenting the complete opposite behaviour of the corresponding residue E90 in the *CrChR2*, which is protonated in the dark state and deprotonated in the last intermediate state of the photoreaction (during the lifetime of the P_4^{510}) [37].

For the D202N variant (second spectrum Figure 3.5(b)) the negative vibrational mode at 1760 cm^{-1} is completely vanished. This variant has already been discussed by *Vera Murders* [33], who assigned the (-)1760 cm^{-1} band to the C=O stretching vibration of D202 amino acid. Aside from this, the spectra of the D202N variant and wild-type differ in the strong positive band around 1705 cm^{-1}, indicating the presence of small amounts of P_1^{590} intermediate state in the D202N spectrum [33, 39]. The absorption changes of the C=O stretching vibration of the introduced Asn residue may also contribute at this frequency range.

The D299N, D299E and E169E variants in Figure 3.5(a) do not show differences as those observed in E136Q and D202N. However, these variants also have strong influence on the *CaChR1* photocycle. The D299N, D299E and E169Q variants were previously investigated by Ogren et. al [39, 40], where they showed light-induced FTIR data of the P_1^{590} and P_2^{380} intermediate states. But due to the new information obtained about the influence of other amino acids, it is necessary to revisit the role of these amino acids (D299 and E169) on the *CaChR1* photocycle.

The D299N variant shows a decrease in the intensity of the positive mode at ~1724 cm^{-1}, probably due to the blue-shift of the maximum positive mode to ~1740 cm^{-1}. The up-shift is consistent with E169 upon P_2^{380} intermediate in the D299N variant, but with a slightly weaker hydrogen bonding [39, 40]. A second difference is the mode at 1698 cm^{-1}, which has a positive feature in the D299N spectrum. This could be due to an overlap with the down-shifted (+)1704 cm^{-1} band. The remaining bands are found at a similar position and intensity as the wild type.

The D299E variant has a stronger positive mode at ~1724 cm^{-1} than the wild type.
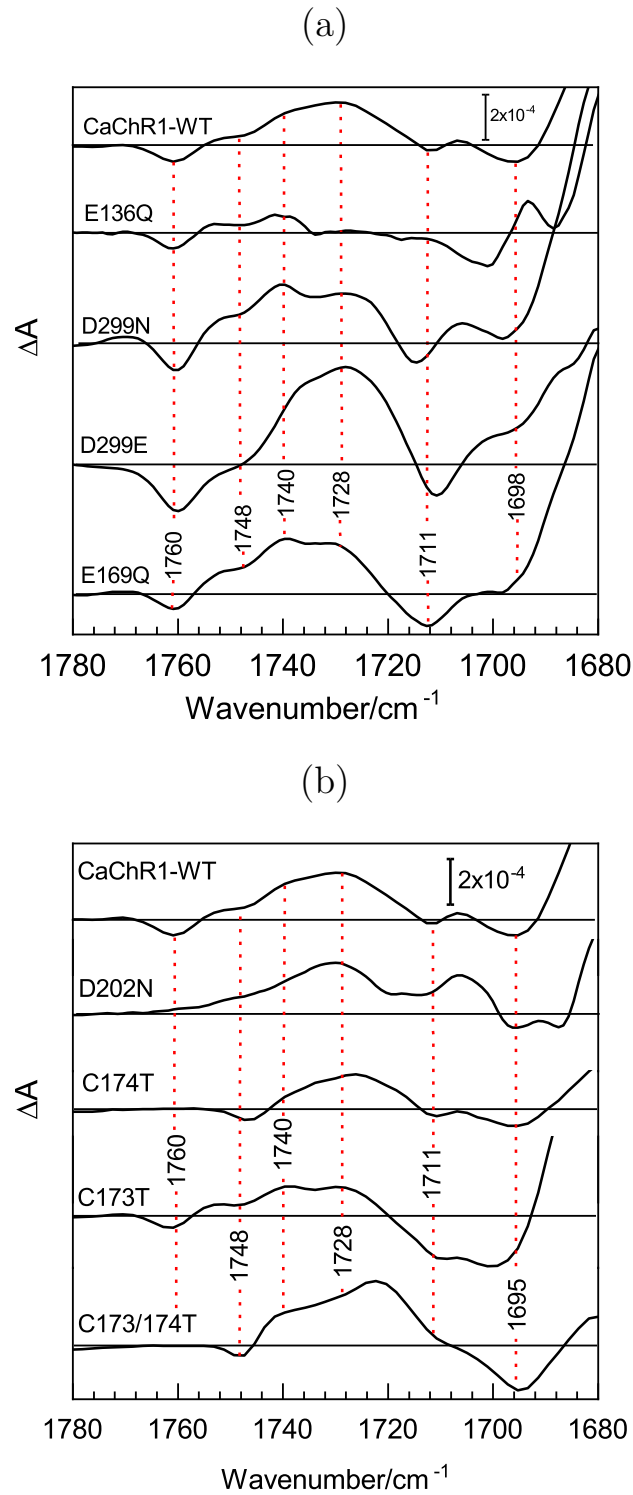
Figure 3.5: Light-induced FTIR of *CaChR1* wild-type and variants (a) E136Q, D299N, D299E and E169Q. (b) D202N, C174T, C173T and C173/174T in the 1800-1690 cm^{-1} range (C=O vibrations). The spectra of the variants were scaled to the retinal band at 1237 cm^{-1} of the wild type. The spectra were recorded at 24 °C under continuous illumination with a LED emitting maximum at 530 nm.

On the other hand, the modes at (+)1740 cm^{-1} and (+)1748 cm^{-1} decrease in intensity. A possible explanation of this behaviour is that the (+)1728/(+)1740 cm^{-1} bands presented in the wild type spectrum shift to lower wavenumbers under this mutation and contribute to the broad positive mode around 1724 cm^{-1} [40]. The modes at (+)1704 cm^{-1} and the (-)1698 cm^{-1} are not present in the D299E spectrum. This could be related to the replacement of the Asp to Glu amino acids, which have a longer chain with an extra carbon and consequently may affect the 1740-1750 cm^{-1} range, provoking a down-shift of the modes in around ∼20-30 cm^{-1} [39, 40].

The E169Q variant shows a decrease in the intensity of the modes around (+)1728 cm^{-1} and (-)1698 cm^{-1}, whereas the remaining vibrational modes of E169Q spectrum have a similar behaviour as the wild type (Figure 3.5). The changes around 1698 cm^{-1} could be related to the replacement of the Glutamic acid for the Glutamine or/and accumulation of a different intermediate than that of the wild type.

Ogren et. al. [39] suggested that during the wild type photocycle the E169 is protonated in the ground state [38], as it is the first amino acid to be deprotonated and consequently forming a negative band in the transition from ground state to P$_1^{590}$ intermediate [39]. This is in agreement with the studies performed by Stensitzki et. al.[116] that assigned a negative vibrational mode around 1690 cm^{-1} as the deprotonation of the E169 in the femtosecond time range. Thus, if the E169 amino acid is deprotonated in the early intermediate [39, 40, 116], its hydrogen bonds will be less strong in the following moments of the photocycle, until it is re-protonated. The re-protonation of E169 could give rise to a positive band in the transition to the P$_2^{380}$ intermediate state at higher wavenumbers (1729/1725 cm^{-1}) [40]. Thus, the positive modes observed in the 1730-1720 cm^{-1} range in the wild type spectrum could be formed by the E169 and E136 overlapped protonation signal.

In Figure 3.5(b) the variants D202N (already discussed above) and the Cysteine variants (replaced by Theorine - C174T, C173T and C173/174T) are shown. The strongest

differences in relation to wild-type are present in the C174T and C173/174T variants, which show a down-shift for the deprotonation mode ((-)1760 cm^{-1} - wild-type), already assigned to D202 [33]. The (-)1760 cm^{-1} mode shifts to a lower position of (-)1745 cm^{-1} in C174T and (-)1748 cm^{-1} in C173/174T variant. An interpretation for the band shift is that the replacement of C174 by the threonine would induce the formation of a stronger hydrogen bond between the terminal COOH of D202 and the hydroxyl side chain of threonine (C174T), provoking the down-shift in the negative vibrational mode ((-)1760 cm^{-1}) [117]. A possible consequence of this amino acid replacements are changes in the positive vibrational modes, which may overlap with the negative modes ((-)1745 cm^{-1} and (-)1748 cm^{-1}) or also present the position shift. This would justify the difference between the intensity of the positive absorption bands in the cysteine variants and the wild type. The down-shift of the (-)1760 cm^{-1} band does not occur for the C173T variant, whereas the range from 1710-1696 cm^{-1} is strongly affected by this mutation. The difference in the lower range could be related to interactions between the C173 and nearby carboxyl amino acids and/or the C173T variant accumulating a different intermediate than that of the wild type .

3.2.3 Cysteine (S-H) Vibrational Range

In this section, a detailed view of the S-H stretching vibration range (2600-2500 cm^{-1}) is taken, allowing analysis of the cysteine side groups in the D202N, C174T, C173T, and C173/174T variants (Figure 3.6). Other carboxylic variants (E136Q, D299N, D299E and E169Q) will also be discussed as they also present some influence on the S-H vibrational bands (Figure 3.7).
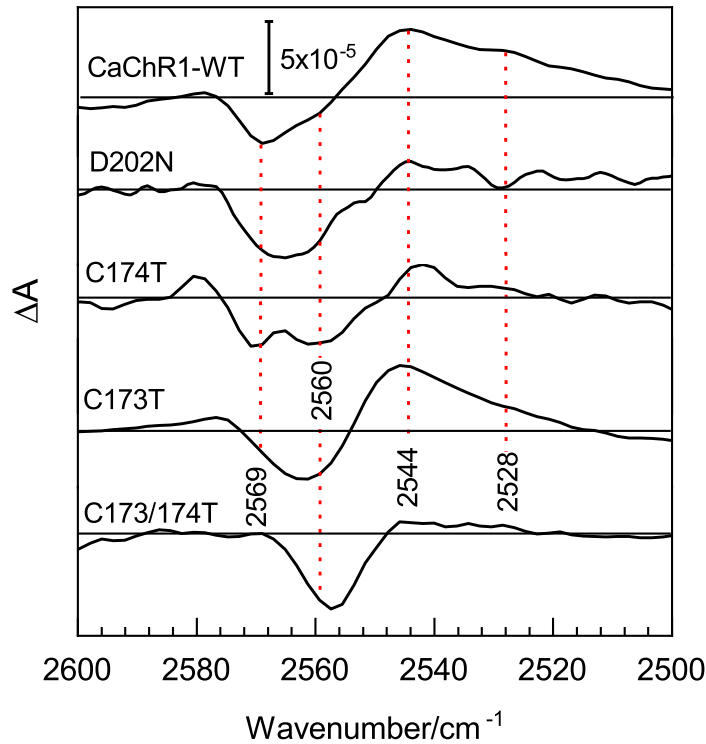
Figure 3.6: Light-induced FTIR of *CaChR1* wild-type and variants D202N, C174T, C173T and C173/174T in the 2600-2500 cm^{-1} range (S-H vibrations). The spectra of the variants were scaled to the retinal band at 1237 cm^{-1} of *CaChR1* wild-type. The spectra were recorded at 24 °C under continuous illumination with a LED emitting maximum at 530 nm.

The changes in the protonation state or in the hydrogen-bonding of the D202N, C174T, C173T and C173/174T variants can be see in Figure 3.6. The light-induced FTIR results for the *CaChR1* wild-type are presented in Section 3.1, which can be summarised as two negative vibrational modes (2569 and 2560 cm^{-1}) and a broad positive vibrational mode with a shoulder (2544 cm^{-1} and 2528 cm^{-1}, respectively). It has already been

argued that the most likely candidates that influence the S-H vibrational range are C174 and C173 [33, 36], but until now no conclusive results were published.

The replacement of the aspartic acid (D) into by asparagine (N) at position 202 (second spectrum in Figure 3.6) strongly affects the S-H vibrational range. Compared to the wild type spectrum, the positive vibrational mode at 2544 cm^{-1} is almost completely vanished and the (-)2569 cm^{-1} band is shifted to a lower wavenumber of (-)2564 cm^{-1}.

For the C174T variant the (-)2569 cm^{-1} mode present in wild-type spectrum is shifted to a higher wavenumber of around $\sim$2571 cm^{-1} and has less intensity than the (-)2560 cm^{-1} band. The (+)2544 cm^{-1} band is almost completely vanished showing only a small signal in C174, similar to the D202N spectrum. The strong effects on the S-H range can be correlated with the D202 and C174 amino acids in *CaChR1* being analogous to the DC gate of the *CrChR2*, which plays a critical role in the *CrChR2* photocycle [118]. Consequently, a strong contribution from D202 and C174 in the *CaChR1* wild-type spectrum is not surprising.

In the C173T variant the (+)2544 cm^{-1} band remains similar in shape and intensity to those presented by wild-type. However, the (-)2569 cm^{-1} band in the wild type spectrum shows a shift to lower wavenumbers in the C173T variant ($\sim$2564 cm^{-1}) and seems to overlap with the (-)2560 cm^{-1} band, which can not be recognized for the C173T variant. In the double variant C173/174T, where the two cysteines were exchanged by theorine, only a negative vibrational mode at 2559 cm^{-1} can be recognized in the photo-stationary state. With the additional mutation of C173 amino acid no positive band can be detected. Thus, the C173 amino acid most likely only has a small contribution in the positive range (2550-2520 cm^{-1}) that may be due to protonation or minor changes in the S-H bond, with the main contribution to the spectral changes stemming from the C174 amino acid. The (-)2569/(-)2560 cm^{-1} bands could not be conclusively assigned to either cysteine amino acids (C173 and C174), leaving open the possibility of these negative vibrational modes resulting from another cysteine, which

would be deprotonated and re-protonated during the photocycle.

Replacing the carboxylic candidates of the proton acceptors (E136, D299 and E169) also affects the S-H vibrational range, as shown in Figure 3.7. Here, the variant E136Q shows minor changes in the S-H vibrational signal, but the variants D299N, D299E and E169Q strongly influence the S-H vibrational range, which could be due to the accumulation of different intermediates or interaction with the nearby cysteines. For the D299N and E169Q variants the (-)2569 cm^{-1} and (-)2560 cm^{-1} modes present in the wild type spectrum are reduced to one band with weaker signal than those of the wild type and shifted position to (-)2562 cm^{-1} (D299N) and (-)2564 cm^{-1} (E169Q).
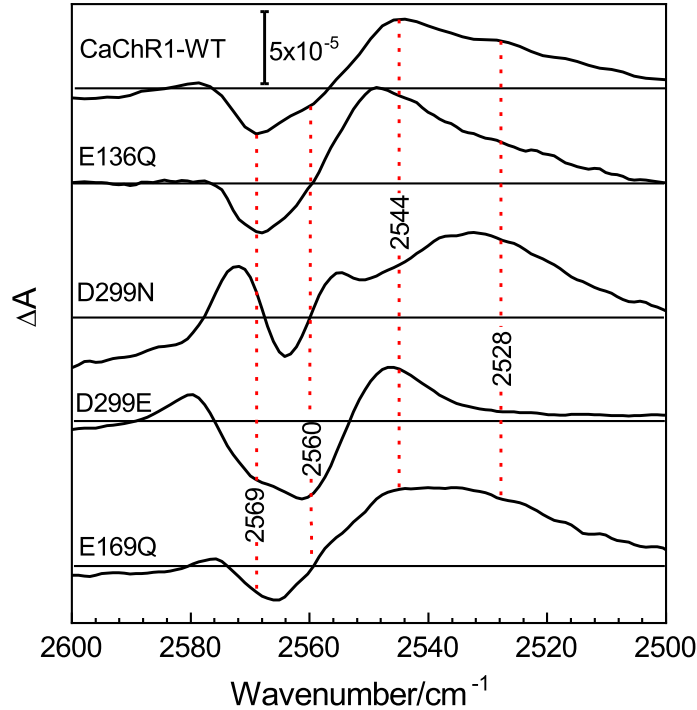
Figure 3.7: Light-induced FTIR of *CaChR1* wild-type and E136Q, D299N, D299E and E169Q variants in the 2600-2500 cm^{-1} range (S-H vibrations). The spectra of the variants were scaled to the retinal band at 1237 cm^{-1} of wild-type. The spectra were recorded at 24 °C under continuous illumination with a LED emitting maximum at 530 nm.

For the D299E variant the negative signal is broader than the wild type and the intensity of (-)2560 cm^{-1} band is increased. In addition, the positive vibrational mode decreases in breadth and intensity for the D299E variant in comparison to the wild type. The

opposite behavior is observed to D299N and E169Q, in both variants the positive signal increases in comparison to the wild type and the $(+)2544$ cm^{-1} band is down-shifted to $(+)2534$ cm^{-1} in the D299N spectrum. Thus, it can be speculated that the mutation of the amino acids D299 and E169 affect the surrounding cysteines, which may have some influence on the S-H stretching vibrations.

3.2.3.1 Overview

The $(-)1760$ cm^{-1} band present in the wild type spectrum is assigned to the D202 amino acid [33]. This difference absorbance can be associated with the deprotonation of the terminal carboxylic group during the transition from the dark state to the P_2^{380} intermediate state. Due to the high frequency of this vibrational mode and the down-shift in C174T and C173/174T $((-)1745$ cm^{-1} and $(-)1748$ cm^{-1}, respectively), it can be suggested that the D202 amino acid is not or just weakly H-bonded in the ground state. The latter possibility cannot be totally excluded since values in this frequency region have been calculated for C=O oscillations, which are hydrogen bonded to the H atom of a cysteine [117]

D202 is the equivalent amino acid of the proton donor of the Schiff base in *CrChR2* (D156). For both proteins these residues are protonated in the dark state and are deprotonated during the photoreaction. In *CaChR1* the D202 is found deprotonated in the P_2^{380} intermediate [33], unlike the *CrChR2* where D156 is deprotonated in the P_3^{520} [37]. It is suggested that in *CaChR1* the Schiff base is also in a deprotonated condition in the P_2^{380} intermediate [33, 35]. Thus, the proton released from D202 does not go straight to the Schiff base, in analogy to *CrChR2* [37]. Rather, it is likely relayed to a different residue. A candidate to store the proton is the C174 amino acid, which is assigned to the protonation band at $(+)2544$ cm^{-1}. The assignment is due to the positive S-H band $((+)2544$ cm$^{-1})$ be missing in the difference spectra of the C174T and C173/174T variants (Figure 3.6). Also, the light-induced FTIR spectrum suggests

the protonation of the E136 amino acid, due to the band at $(+)1728$ cm^{-1}. This is contrary to the assignment suggesed by Ogren et. al. [40], who attribute this mode to the E169 amino acid.

However, changes observed in the light-induced FTIR difference spectra of the variants in comparison to the wild type, could be due to the accumulation of different intermediates rather than obstructions of deprotonation and reprotonation. Thus, the band assignment using only light-induced FTIR difference spectra is ambiguous and inconclusive. On this basis, time-resolved IR spectroscopy using EC-QCL was conduced for all the variants in the 2600-2500 cm^{-1} and 1800-1510 cm^{-1} vibrational frequency ranges.

3.3 Time-Resolved spectroscopy on wild-type CaChR1

This section will focus on the temporal evolution of the vibrational modes found within the 1800-1510 cm^{-1} and 2600-2500 cm^{-1} ranges which are related to the conformational changes and proton transfers of the *CaChR1* photo-intermediates. The contour plot of these two vibrational ranges are shown in Figure 3.8, in red are the positive vibrational modes and in blue the negative vibrational modes.

(a) (b)
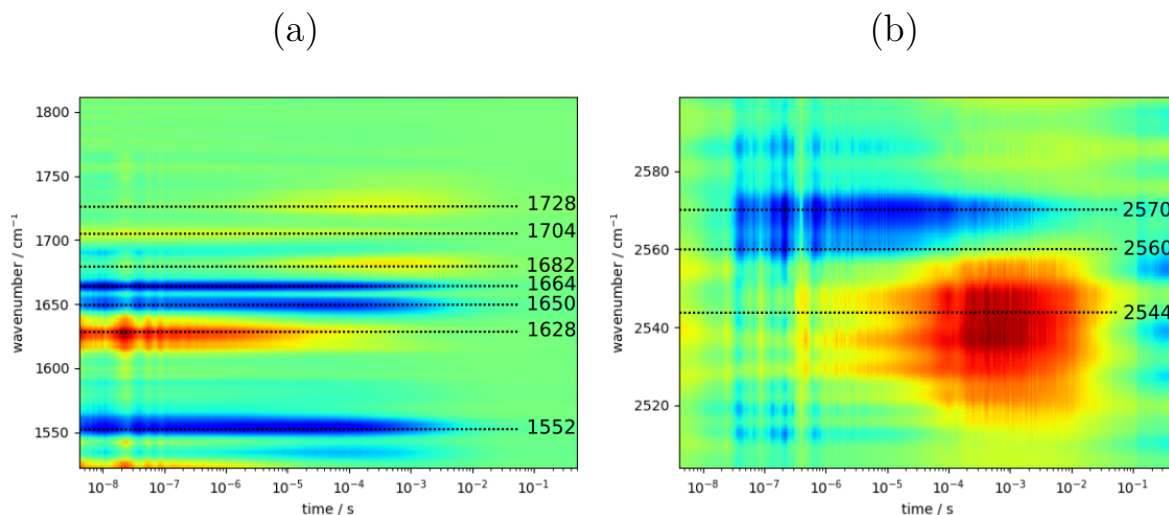
Figure 3.8: Time-Resolved IR absorbance changes in *CaChR1* during the photocycle. (a) the contour plot of transient absorbance 1800-1510 cm^{-1} range and (b) the contour plot of transient absorbance 2600-2500 cm^{-1} range. The frequency position of some of the vibrational modes are indicated in the figure. The kinetics were collected after laser excitation at 532 nm.

The SVD and global analysis of the data sets shown in Figure 3.8 were performed using a home-built algorithm written in Python by *David Ehrenberg*. It functions using a certain number of singular components which are fitted with a defined number of exponential decays. From the global analysis we can extract the time constants (Table 3.1) and the species associated spectra (SAS) showing the key intermediate states of the *CaChR1* wild-type. The data analysis of *CaChR1* data were made using simple sequential reactions schemes, which satisfactorily describes the photocycle mechanism

of the data presented in this work. However, this does not eliminate the possibility of a more complicated description of the *CaChR1* photocycle.

Table 3.1: Time constants of the *CaChR1* wild-type photoreaction derived from global analysis of time-resolved IR Spectroscopy.

τ(s)/spectral range	1800-1510 cm^{-1}	2600-2500 cm^{-1}
τ_1 (P$_1^{590}$)	2.7 ± 0.2 μs	0.8 ± 0.2 μs
τ_2 (P$_1^{590} \rightarrow$ P$_{2a}^{380}$)	37 ± 4 μs	83 ± 8 μs
τ_3 (P$_{2a}^{380} \rightarrow$ P$_{2b}^{380}$)	0.77 ± 0.04 ms	–
τ_4 (P$_{2b}^{380}$)	7.1 ± 0.5 ms	5.3 ± 1 ms
τ_5 (P$_{2b}^{380} \rightarrow$ P$_4^{520}$)	–	53 ± 7 ms

Based in the analysis and in Ref. [33] can be suggested that after green-light (532 *nm*) excitation, the *CaChR1* wild-type converges from the ground state to the P$_1^{590}$ intermediate state that decay under τ_1 and τ_2 time constants. The decay of P$_1^{590}$ give the raise of the P$_{2a}^{380}$ intermediate with τ_2. The decay of the P$_{2a}^{380}$ and raising of the P$_{2b}^{380}$ intermediates occur with τ_3. The subsequent time constants correspond to the decay of P$_{2b}^{380}$ intermediate state.

3.3.1   1800-1510 cm^{-1} Vibrational Range

In Figure 3.9 are show the spectra of *CaChR1* wild-type in the 1800-1510 cm^{-1} vibrational range. For the P$_1^{590}$ spectrum the (-)1534/(+)1520 cm^{-1} modes are found. The (-)1534 cm^{-1} band corresponds to the C=C stretching mode in the ground state with the retinal in the all-*trans* configuration and a protonated Schiff base [34, 35]. The (+)1520 cm^{-1} is assigned as the characteristic band of the ethylenic vibrations (C=C) in the P$_1^{590}$ intermediate state [39]. Due to the differences in the retinal environment of *CaChR1* and *BR*, the visible absorption of the *CaChR1* wild-type is blue-shifted and the ethylenic modes are up-shifted to higher frequencies in comparison to *BR* (UV/Vis absorption around 560 nm and ethylenic modes at (-)1529/(+)1514 cm^{-1}) [119–122]. However, based on the similarities of the ethylenic bands ((-)1534/(+)1520), it is suggested that the P$_1^{590}$ intermediate of the *CaChR1* wild-type is analogous to the
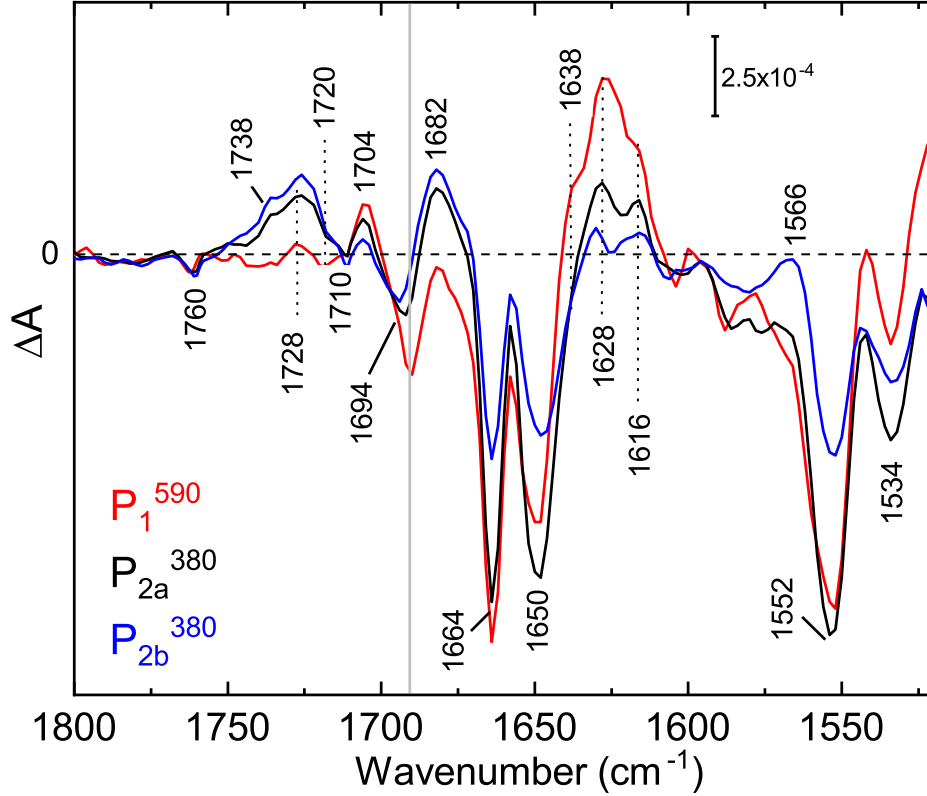
K intermediate of the *BR* [39].

Figure 3.9: Species associated spectra(SAS) showing the key intermediate states of the *CaChR1* wild-type photoreaction recorded by time-resolved IR spectroscopy. The data analysis was made using a simple sequential reactions schemes. The sequential model has four components, before the decay back to the ground state. Corresponding time constants are listed in table 3.1. The red spectrum correspond to pure P_1^{590} intermediate state. The black spectrum correspond to the P_{2a}^{380} intermediate state. The blue spectrum correspond to P_{2b}^{380} intermediate state. The vertical gray line indicates where the data was merged. The 1800-1690 cm^{-1} and 1690-1510 cm^{-1} ranges were measured separately with distinct samples, the 1800-1690 cm^{-1} was re-scaled (divide by 2) and merged with 1690-1510 cm^{-1} before the analysis be perform. For better understanding and reduced noise the final set was smoothed by factor 2, thus the spectra resolution is 4 cm^{-1}. The data were collected after laser excitation at 532 nm.

Near the mode of C=C double bonds of the retinal ((-)1534 cm^{-1}) a second mode at (-)1552 cm^{-1} is found. The (-)1552 cm^{-1} signal indicates an additional ethylenic vibration [35] with a contribution from the amide II backbone structure [36, 39]. This amide II contribution is formed by the coupling of the C-N stretching and NH bending vibrations of the peptide groups [39, 123]. The (-)1552 cm^{-1} intensity decreases in the P_{2b}^{380} spectrum (Figure 3.9 - blue trace). The 1566 cm^{-1} band is the characteristic mode

of the ethylenic vibrations in the configuration of 13-*cis* retinal with a deprotonated Schiff base [35, 36, 40]. The 1566 cm^{-1} mode rises with the formation of the P_{2a}^{380} spectrum, being more prominent in the P_{2b}^{380} spectrum.

In the 1690-1600 cm^{-1} vibrational range (combination of C=N and C=O stretch of the amide I peptide bond), the (-)1664 cm^{-1} mode is assigned to the C=O stretch of the amide I peptide backbone groups [36, 102] and has a strong signal in the P_1^{590} spectrum, recovering in intensity only in the P_{2b}^{380} spectrum. The (+)1682 cm^{-1} band characteristic of *CaChR1* [39] has no signal during P_1^{590}, but reaches maximum intensity in the P_{2b}^{380} intermediate state (open state). The rise of the (+)1682 cm^{-1} band can be an indicative of weakening of the the H-bond between the peptide C=O and N-H groups [36, 102]. The (-)1650 cm^{-1} band assigned to the C=N stretch mode [39, 124], has strong signal in P_1^{590} and reaches its maximum intensity in the P_{2a}^{380} intermediate state.

In the 1690-1600 cm^{-1} vibrational range of the P_1^{590} spectrum, three strong positive vibrational modes are present: at (+)1628 cm^{-1} and two shoulders at (+)1635/(+)1616 cm^{-1}. Ogren et. al. [39] based on a FTIR investigation of *CaChR1* wild-type at low temperatures, suggested that the (+)1638 cm^{-1} band is the down-shift of (-)1650 cm^{-1} and corresponds to the C=N stretch in the P_1^{590} intermediate state [39]. The (+)1628/(+)1616 cm^{-1} bands could be attributed to the protein amide I vibrations [39, 124]. Analogously, *CrChR2* has a vibrational mode at (+)1624 cm^{-1} which is attributed to hydrogen-bonding changes of an arginine [125].

3.3.1.1 1690-1510 cm^{-1} Kinetics

The main kinetics of the 1690-1510 cm^{-1} range are shown in Figure 3.10 and 3.11. The 1652 cm^{-1} kinetic (C=N stretching mode on the ground state) has a strong negative signal in its early stages and fast recovery with $\tau_3^{1800-1510} = 0.77$ ms (time constants are shown in Table 3.1), suggesting that changes in the amide I peptide backbone vibration

happen between the P_{2a}^{380} and P_{2b}^{380} intermediate states. The $(+)1682$ cm^{-1} kinetic has no signal during the early stages, then emerging to show its maximum intensity at $\tau_3^{1800-1510}$ time constant. This behaviour is suggestive of changes in the H-bonded peptide C=O and N-H groups in the rise of the P_2^{380} intermediate.

In Figure 3.10(b) the kinetics of the $(+)1616$, $(+)1628$ and $(+)1636$ cm^{-1} vibrational modes are shown, these kinetics have strong signal during $\tau_1^{1800-1510} = 2.7$ μs indicating that they arise in the sub-ns time-range. The 1628 cm^{-1} and 1636 cm^{-1} kinetics shown a fast recovery decay even before $\tau_3^{1800-1510}$, having strong signal only during the P_1^{590} intermediate ($\tau_1^{1800-1510}$). The $(+)1616$ cm^{-1} kinetic has a slower decay compared to the other two kinetics (1628 cm^{-1} and 1636 cm^{-1}).

In Figure 3.11 the 1532 cm^{-1}, 1552 cm^{-1} and 1566 cm^{-1} kinetics are shown. The 1566 cm^{-1} kinetic has negative signal its early stages and evolves rapidly after the second time constant ($\tau_2^{1800-1510} = 37$ μs). An mentioned early, the mode at this position (1566 cm^{-1}) is characteristic of the C=C vibrations in the P_2^{380} intermediate, which is indicative of a deprotonated retinal Schiff base [35, 36, 40].

The $(-)1532$ cm^{-1} kinetic (C=C vibrations in the ground state with protonated all-*trans* retinal Schiff base) has no signal the initial stages of measurement, evolving to a negative intense signal after the first two time constants ($\tau_1^{1800-1510} = 2.7$ μs and $\tau_2^{1800-1510} = 37$ μs) and presenting fast recovery behaviour after $\tau_3^{1800-1510}$. The 1552 cm^{-1} kinetic has strong signal from the beginning showing a slight growth in the signal in the $\tau_2^{1800-1510}$ and a fast recovery around the $\tau_3^{1800-1510}$ time constant. Suggesting changes in the C-N stretching and NH bending vibrations of the peptide groups (amide II) between the P_{2a}^{380} and P_{2b}^{380} intermediates.

(a)

(b)

Figure 3.10: Kinetics of the 1690-1600 cm^{-1} vibrational range of the protein backbone of the *CaChR1* photocycle. (a) The kinetics 1652 cm^{-1} in blue and 1682 cm^{-1} in red. (b) 1616 cm^{-1} in blue, 1628 cm^{-1} in red and 1636 cm^{-1} in magenta. The time traces were subjected to global analysis, the curve fit are shown in grey. The time constants from Table 3.1 are indicated in the figure. The kinetics were collected after laser excitation at 532 nm.

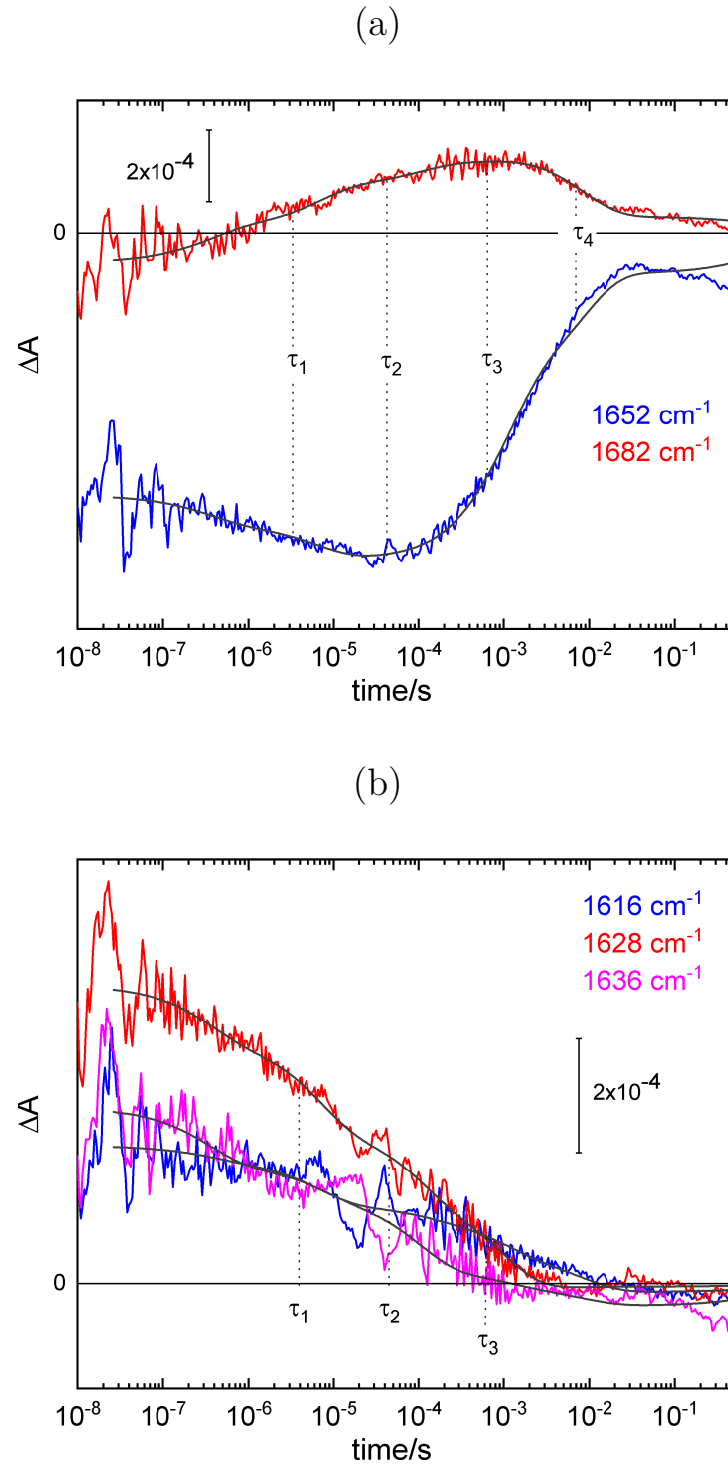**Figure 3.11:** Kinetics of the 1600-1510 cm^{-1} vibrational range of the protein backbone of the *CaChR1* photocycle. 1532 cm^{-1} in black, 1552 cm^{-1} in blue and 1566 cm^{-1} in red. The time traces were subjected to global analysis, the curve fit are shown in grey. The time constants from Table 3.1 are indicated in the kinetics. The kinetics were collected after laser excitation at 532 nm.
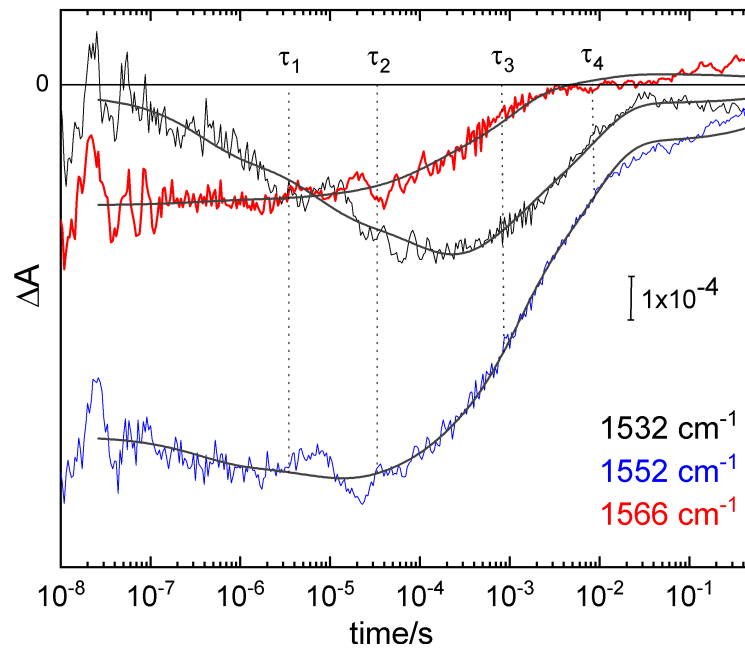
3.3.2   Carboxylic (C=O) Vibrational Range

In the 1800-1690 cm^{-1} range (Figure 3.9: carboxylic range) the vibrational modes of protonation and deprotonation of Asp and Glu residues are found, as well as changes of the hydrogen bond in their terminal -C(=O)-OH groups. For the *CaChR1* wild-type a large number of overlapping vibrational bands are expected in this region. The P_1^{590} intermediate state, shows the presence of vibrational modes at (+)1704 and (-)1690, which are mainly in agreement with the light-induced FTIR data published by Ogren et. al. [39]. The strongest protonation band ((+)1704 cm^{-1}) of the P_1^{380} intermediate decays quickly, exhibiting less than half of the initial intensity in P_{2b}^{380} substate. The negative band at (-)1690 cm^{-1} show a up-shift behavior in the transition to P_{2a}^{380} ((-)1694 cm^{-1}) and P_{2b}^{380} ((-)1698 cm^{-1}) intermediate states.

New vibrational modes at (-)1710, (-)1760, (+)1720, (+) 1728 and (+)1738 cm^{-1} are rising in the transition from P_1^{380} to P_2^{380} intermediate states. (+)1728 cm^{-1}, the strongest vibrational mode in the carboxylic region, together with the modes at (-)1710, (-)1760 and (+)1738 cm^{-1}, reach their maximum intensity in the P_{2b}^{380} substate. Here, it is necessary to emphasize that the time-resolved IR data of *CaChR1* is distinctly different than what were observed for *CrChR2* [37] and for the M state of *BR* [96, 126], indicating a distinguishable proton transfer mechanism among these proteins.

3.3.3   Cysteine (S-H) Vibrational Range

As previously mentioned, *CaChR1* has an extensive number of cysteine amino acids located at the N-terminal part of the channel (aa 1-352) that present central locations (see Figure 1.3). Thus, it is expected that the cysteine amino acids play an important role in the *CaChR1* photocycle. The hydrogen-bonding and protonation changes in the terminal thiol group of the cysteine of *CaChR1* were reported by Ref. [36] and the attempt at assignment of the vibrational bands using different variants by Ref.

[33]. However, only steady state FTIR data were used in these previous investigations, providing no information on the kinetics and temporal evolution of the photocycle.

Figure 3.12 show three spectra at different time ranges, indicating the maximal spectral changes, the curves and the standard deviation bars were obtained by the averaging three time windows from 0.4 - 2 μs, 1 - 7 ms and 90 - 250 ms. The time windows were chosen taking care that only one intermediate state is accumulated for each spectrum. In Figure 3.12, all the spectra contain valleys and ridges that could be related to the off-set of the kinetics. In this work it was decided not to perform the off-setting correction since the *CaChR1* reaction is longer than the time range measured by the time-resolved IR experiment. It could therefore be possible that in the later times some of the ridges and valleys are also mixed with information about later stages of the photocycle reaction.
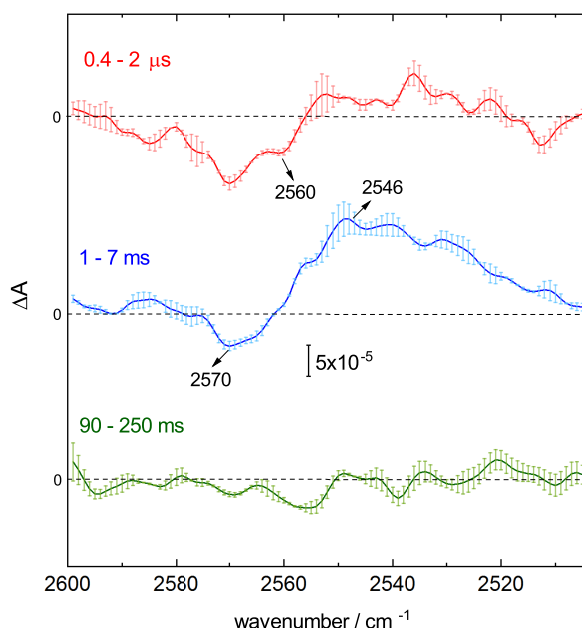
Figure 3.12: Time-resolved IR difference spectrum of *CaChR1* wild-type in the region characteristic of S-H vibrations (2600-2500 cm^{-1}). Spectra at different times were selected to indicate the maximum of the spectral changes. The data set were averaged from 0.4 - 2 μs, 1 - 7 ms and 90-250 ms, providing the standard deviation. The data were collected after laser excitation at 532 nm. The raw data were smoothed for the spectral resolution of 4 cm^{-1}.
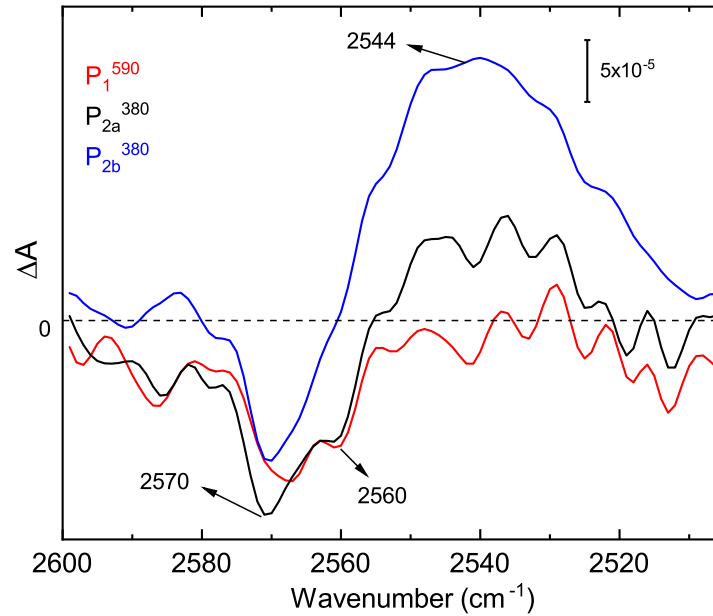
Figure 3.13: The species associate spectra (SAS) of the first three intermediate states of the *CaChR1* wild-type photoreaction recorded by time-resolved IR spectroscopy. Corresponding time constants are listed in table 3.1, for clarity the SAS of P_4^{510} has been omitted. The data was collected after laser excitation at 532 nm.

As previously shown in the light-induced FTIR data of the *CaChR1* wild-type Figure 3.2(b) and Ref. [36] the S-H range can be described by two negative vibrational modes at (-)2569/(-)2560 cm^{-1} and one positive vibrational mode at (+)2544 cm^{-1}. The time-resolved IR data shows peaks at the same positions, the negative range has strong intensity during the early stages (sub-ms timescale) and the positive range has a higher intensity in the ms time range.

The SAS of *CaChR1* wild-type for the S-H range are shown in Figure 3.13, the (-)2570 cm^{-1} mode has the maximum intensity at P_{2a}^{380} (Figure 3.13), while the (-)2560 cm^{-1} band has nearly half of the intensity of (-)2570 cm^{-1}. The (-)2560 cm^{-1} shows its strongest intensity signal in P_1^{590} spectrum, keeping the signal almost constant in the P_{2a}^{380} and eventually being almost completely vanished in the P_{2b}^{380} substate. *CaChR1* has two possible rotamers with distinct orientation in respect to the C-S torsion [107, 127], which may give rise to the the vibrational mode at 2560 cm^{-1}. The P_1^{590} intermediate contains only negative vibrational modes, the (+)2544 cm^{-1} band shows a small signal

in the P_{2a}^{380} and maximum intensity in the P_{2b}^{380} intermediate.

The kinetics of carboxylic C=O (1800-1690 cm^{-1}) and S-H (2600-2500 cm^{-1}) vibrational ranges are discussed in the next sections combined with the band assignment using the time-resolved IR data of the variants.

3.3.3.1 Overview

Figure 3.9 suggests that during the P_{2a}^{380} to P_{2b}^{380} intermediate state transition, changes in signal are observed exclusively in the 1670-1510 cm^{-1} range, with no significant contribution in the C=O vibrational range (1800-1690 cm^{-1}). The changes in amide I vibrations consist mainly of the mode νC=O and N-H groups of the peptide backbone and amide II vibrations are mainly the coupled mode of the C-N stretching and N-H in-plane bending vibrations of the peptide backbone [103]. Thus, the changes in the amide I and II vibrational modes could be related with hydration and/or structural changes of the protein backbone.

The hydration changes of the α-helix can down-shift the amide I vibration frequency in around 8-20 cm^{-1}, due to H-bonding changes between the amide C=O and water molecules [128, 129], this behaviour was observed to *CrChR2* that presented the down-shift of (-)1663/(+)1650 cm^{-1} [37]. A similar effect was proposed for the amide II bands [37], here a frequency up-shift around (-)1550/+1560 cm^{-1} in *CrChR2* could be due to alterations between the H-bonding of water and the amide C=O, which would lead to the weakening of the H-bond between amide C=O and N-H pairs, provoking a stronger N–H bond [37].

It is possible that analogous effect happen to *CaChR1*, Lórenz-Fonfría et. al. [36] associated vibrational changes in the amide I and amide A ranges in the transition from the ground state to P_2^{380} intermediate. The (-)1662 cm^{-1}, has a fast recovery in $\tau_3^{1800-1510}$, appear in the typical region for transmenbrane helices. In line with this assignment Lórenz-Fonfría et. al. [36] have identified the negative bands at (-)3318/(-)3288 cm^{-1}, which are in the characteristic region for the amide A vibration (N-H stretching) of α-helices [103, 104]. The (+)1628 cm^{-1} is associated to the (+)3247 cm^{-1}, the last assigned to the amide A vibrations of β-strands [103]. The band at (+)1682 cm^{-1} and bands found at (+)3382/(+)3348 cm^{-1} [36] indicate weak H-bonded peptide C=O and N-H group [102]. For α-helical transmembrane proteins the amide

II vibrations of the α-helix are found around 1545-1540 cm^{-1} [103], in *CaChR1* the (-)1552 cm^{-1} is assigned as a combination of amide II and retinal (C=C) vibrations [35] and has fast recovery in the $\tau_3^{1800-1510}$. Based on these observations, we can suggest that the alterations in the amide I and II vibrational modes under the $\tau_3^{1800-1510}$ time constant are a strong indicative of conformational and/or H-bond changes in the protein backbone that could happen in the transition from the P$_{2a}^{380}$ to P$_{2b}^{380}$, providing the biphasic characteristic of the P$_2^{380}$ intermediate. However, no conclusive statement can be make based only on the data presented here, to clarify these hypothesis more experiments need to be performed in the amide A and fingerprint ranges, focusing on the conformational and hydration changes of *CaChR1*.

3.4 Time Resolved spectroscopy on CaChR1 variants

In this section, the time-resolved IR data performed on the carboxylic and cysteine variants are analyzed. Here, the tentative assignment of the vibrational bands started in sections 3.2.2. and 3.2.3 using light-induced difference FTIR data are expanded upon.

Below are the time-resolved spectra in the carboxylic range showing the maximum accumulation of the P_1^{590} and P_2^{380} intermediate states. The spectra for each variant's maximum accumulation were chosen based on the global analysis of the variants and the UV/Vis flash photolysis data, shown by *Vera Muders* [33]. All the variants investigated in this work exhibit the all-*trans* to 13-*cis* isomerization and the formation of a red-shifted P_1^{590} photo-product intermediate. As only the carboxyl and cysteine regions were measured for the variants there is no amide or fingerprint region available for scaling. Thus, the scaling of the variants in the carboxyl vibrational range was done using the negative vibrational mode at 1760 cm^{-1}, except for the variant D202N which was scaled using the (+)1732 cm^{-1} vibrational mode. In the S-H vibrational range the variants were scaled in relation to the wild type using the negative (-)2570 cm^{-1} vibrational mode. For the S-H range a comparison can be made between *CaChR1* wild-type and the variants spectra with maximum accumulation of the P_2^{380} intermediate state.

3.4.1 Cytoplasmic Side Amino Acids

3.4.1.1 C=O Vibrational Range

In Figure 3.14 the P_1^{590} and P_2^{380} spectra of the D202N and C174T variants are shown. In the P_1^{590} spectra of D202N variant the $(+)1704$ cm^{-1} band is not as pronounced as in the wild type (Figure 3.14A). The negative band around the 1718-1710 cm^{-1} range show stronger signal in comparison to the wild type. This behavior can be associated with the $(+)1704$ cm^{-1} mode being weaker in the D202N variant, which could affect the nearby vibrational modes.
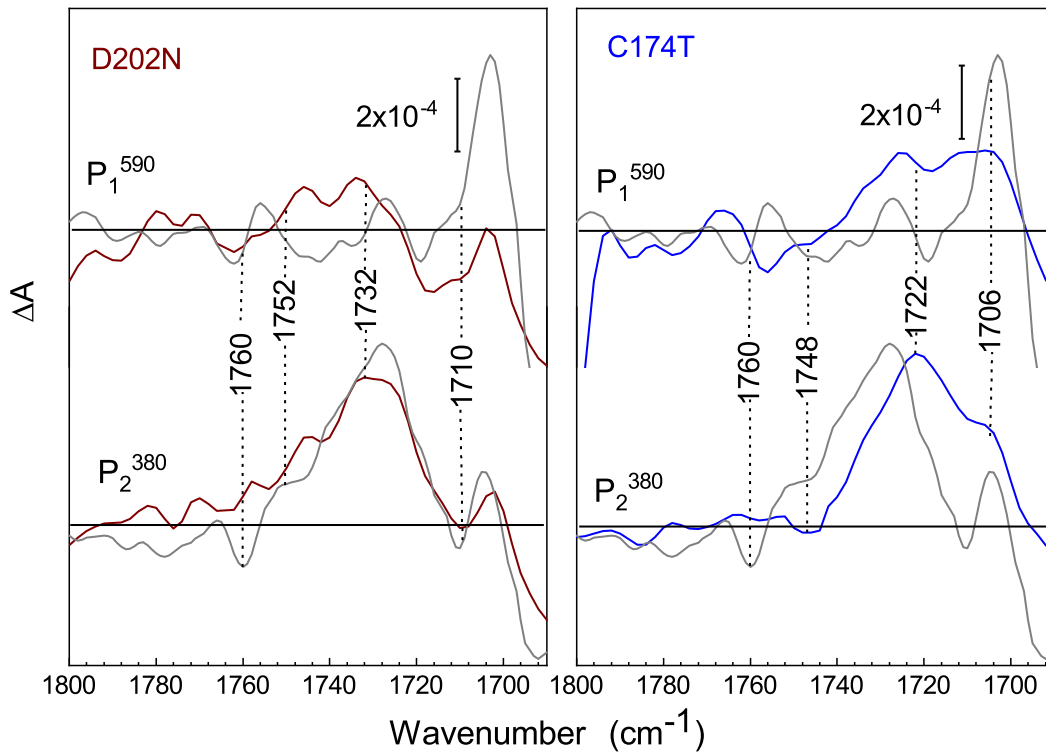
Figure 3.14: Time-resolved IR absorbance changes in *CaChR1* variants during the photocycle in the 1800-1690 cm^{-1} range. A) D202N (burgundy trace) and B) C174T (blue trace), the wild type spectra were repeated in gray trace. The spectra show the maximum absorption of the *CaChR1* wild-type and variants in the P_1^{590} and P_2^{380} intermediate state. For clarity and to reduce the signal-to-noise ratio the raw data were smoothed for the spectral resolution of 4 cm^{-1}. The samples were excited by a YAG laser at 532 nm.

In the P_2^{380} spectrum of the D202N variant the 1752-1690 cm^{-1} range is similar to the

wild type. The most perceivable difference is the absence of the (-)1760 cm^{-1} band, assigned to the deprotonation of D202 [33]. The high frequency of the vibrational mode ((-)1760 cm^{-1}) indicates that D202 is only slightly or not at all hydrogen bonded in the ground state. Contrary to what is observed in the *CrChR2*, where the analogous amino acid D156 was assigned to a vibrational mode at 1737 cm^{-1} [37], suggesting a stronger hydrogen bond in D156 than the one presented by D202 (*CaChR1*).

At section 3.2.2 light-induced difference data show that the cysteine variants strongly influence the carboxylic region (see Figure 3.5). As already mentioned, replacing the cysteine amino acid for a threonine at position 174 could result in the formation of a stronger hydrogen bonds with D202, affecting the vibrational modes in the P_1^{590} and P_2^{380} intermediate state of the C174T variant. In the P_1^{590} intermediate state of the C174T variant (see Figure 3.14B) the 1703-1728 cm^{-1} range has a broad positive band while no negative vibrational mode is recognized in this range (1703-1728 cm^{-1}). In the transition from the P_1^{590} to P_2^{380} intermediate states the strongest vibrational mode is found at frequency (+)1722 cm^{-1} and has an increased signal intensity.

The double variant C173/174T shows changes in the lower frequency range (see Figure 3.15A), the P_1^{590} spectrum has a broad positive range at 1735-1700 cm^{-1}, making it difficult to distinguish the bands individually. An intense positive peak at 1734 cm^{-1} is immediately apparent and there is a noticeable absence of the strong vibrational mode at (+)1704 cm^{-1}. The P_2^{380} intermediate reveals an intense positive mode at 1722 cm^{-1} and two shoulders at (+)1704 and (+)1734 cm^{-1}, similar to C174T variant. The C173/174T variant has the negative band down-shifted to position 1744 cm^{-1}, emphasizing the influence of the threonine at position 174.

Unlike the other cysteine variants, the C173T variant has no shift in position of the vibrational modes. In the P_1^{590} photo-intermediate three vibrational modes are distinguished around (+)1708, (+)1722 and (+)1734 cm^{-1} and one shoulder at (+)1756 cm^{-1} (see Figure 3.15). A vibrational mode at (-)1762 cm^{-1} is distinguishable in P_1^{590}

intermediate state and is down-shifted to 1760 cm^{-1} in the P$_2^{380}$ intermediate state. Except for the vibrational mode around (+)1708 cm^{-1} that is vanished in the P$_2^{380}$ intermediate state, the other positive bands grow in intensity without any position change. The (-)1696/8 cm^{-1} band found in the wild type spectra, is absent in the P$_2^{380}$ spectra of the C173T variant. The changes in the lower frequency region could indicate interaction between the C173 and nearby carboxylic amino acids, such as D299 and E169 [116].

Figure 3.15: Time-resolved IR absorbance changes in *CaChR1* variants during the photocycle in the 1800-1690 cm^{-1} range. A) C173/174T (green trace) and B) C173T (red trace), the wild type spectra were repeated in gray trace. The spectra show the maximum absorption of the *CaChR1* wild type and variants in the P$_1^{590}$ and P$_2^{380}$ intermediate state. For clarity and to reduce the signal-to-noise ratio the raw data were smoothed for the spectral resolution of 4 cm^{-1}. The samples were excited by a YAG laser at 532 nm.

3.4.1.2   S-H Vibrational Range

The spectrum of the time-resolved data of the D202N variant in the S-H region (see Figure 3.16) are in good agreement with the light-induced spectra shown in Figure 3.6.

However, some differences are found for the C174T variant between the steady state (3.6(b) - third spectrum) and the time-resolved data (Figure 3.16(b)). The last one has a strong negative mode at position 2562 cm^{-1} (Figure 3.16(b)), unlike the steady state which has two negative modes at 2569 cm^{-1} and 2560 cm^{-1} (Figure 3.6). The increase of the (-)2562 cm^{-1} band in the time-resolved data could be associated to an overlap with the secondary negative mode at the position 2560 cm^{-1} or the possibility of S-H oscillation may be influenced by electrostatic interaction of the isomerized retinal. In addition, the differences between the light-induced and time-resolved data could come from the improvement of the signal using a EC-QCL and the fact that the time-resolved data (Figure 3.16(b)) reflects only signal from pure P$_2^{380}$ intermediate state without contribution of any other intermediate. This may cause some deviation between the light-induced and the time-resolved data.

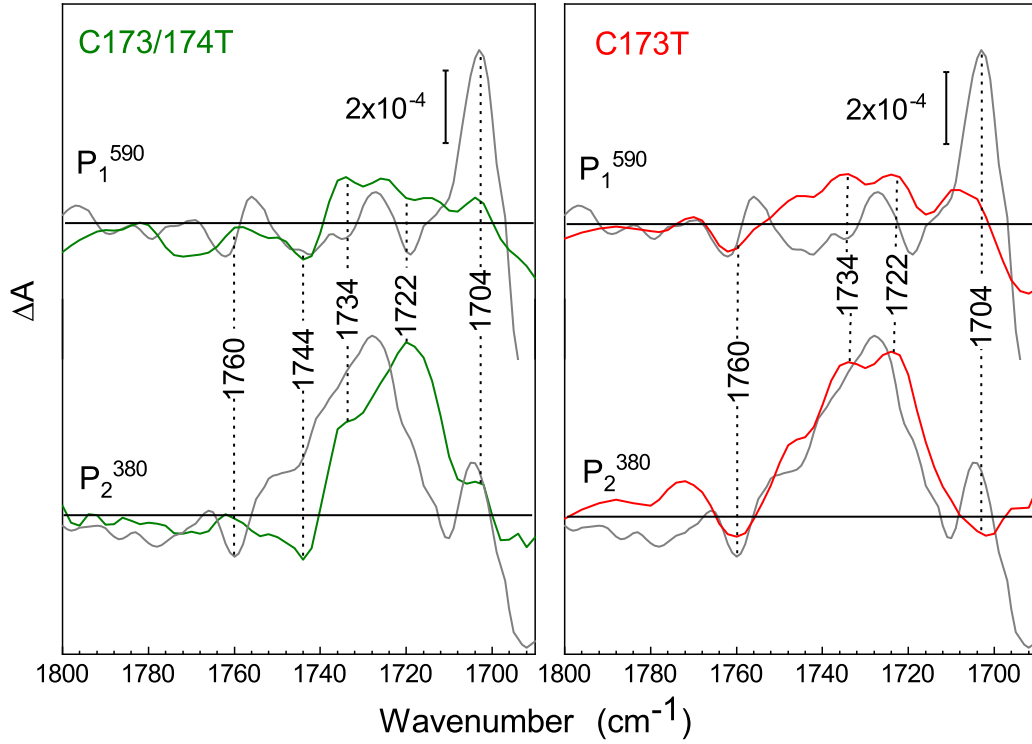**Figure 3.16:** Time-resolved IR absorbance changes in *CaChR1* variants during the photocycle in the 2600-2500 cm^{-1} range. (a) D202N (burgundy trace) and (b) C174T (blue trace), the *CaChR1* wild-type spectrum was repeated in gray trace. The data show the maximum absorption of the *CaChR1* wild-type and variants in the P$_2^{380}$ intermediate state. For clarity and to reduce the signal-to-noise ratio the raw data were smoothed for the spectral resolution of 4 cm^{-1}. The samples were excited by a YAG laser at 532 nm.

The carboxylic variant D202N (see Figure 3.16 (a)) shows a downshift in the negative vibrational modes in comparison to *CaChR1* wild-type, the bands are found at (-)2566

and (-)2558 cm^{-1}. The presence of more intense signal around (-)2558 cm^{-1} could be due to the absence of a strong positive band in the D202N.Thus, we can speculate that the shift of (-)4 cm^{-1} in the (-)2566 cm^{-1} vibrational mode in D202N spectrum may be a consequence of the overlap with a more intense (-)2558 cm^{-1} vibrational mode. Similar to the D202N and C174T variants, the positive mode of the S-H vibrations is not recognized for the C173/174T variant (Figure 3.17(a)), only a negative mode at (-)2558 cm^{-1} is found in the P$_2^{380}$ pure spectrum.

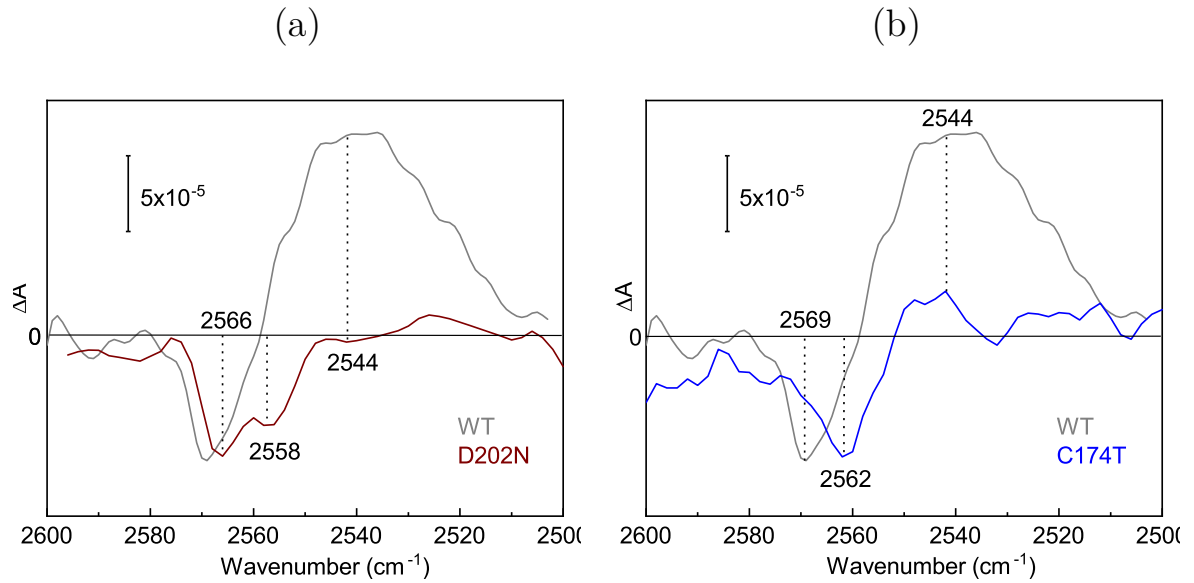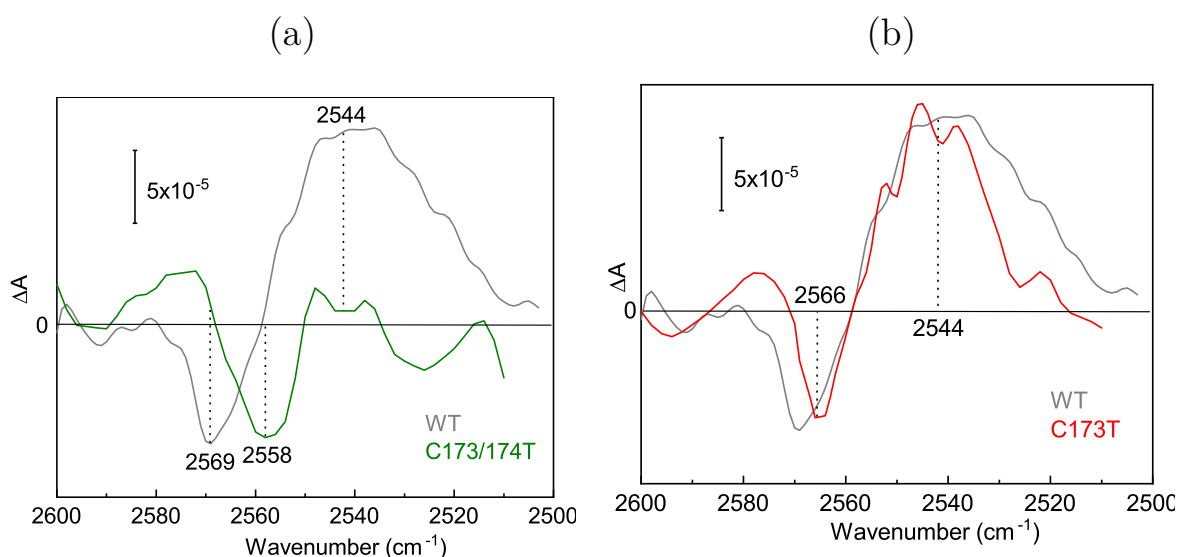**Figure 3.17:** Time-Resolved IR absorbance changes in *CaChR1* variants during the photocycle in the 2600-2500 cm^{-1} range. (a) C173/174T (green trace) and (b) C173T (red trace), the *CaChR1* wild-type spectrum was repeated in gray trace. The data show the maximum absorption of the *CaChR1* wild-type and variants for the P$_2^{380}$ intermediate state. For clarity and to reduce the signal-to-noise ratio the raw data were smoothed for the spectral resolution of 4 cm^{-1}. The samples were excited by a YAG laser at 532 nm.

The C173T variant shows the most similarity with the wild type (Figure 3.17(b)), but in the time-resolved data, the differences between the P$_2^{380}$ intermediate of C173T and the wild type are more perceptible. The C173T variant has a positive mode at 2544 cm^{-1} which is sharper than that of the wild type and only one negative mode at 2566 cm^{-1} (see Figure 3.17(b)). Since is suspected that the C173 is not directly involved in the proton transfer during the photocycle, a possible interpretation for the differences is due to the proximity of C173 with the retinal. Here, the isomerization of the retinal could affect the nearby cysteines and consequently provoke changes in the S-H vibrational

oscillations. In addition, the (-)2569 cm^{-1} mode may originate from the hydrogen bonds between the C173 with nearby amino acids. The replacement of the cysteine for a threonine could affect the existence of these hydrogen bonding. A suggestion is that the C173 and C174 could be H-bonded in the ground state, which could reduce the pKa value of C174 and enable the deprotonated condition of C174 in the ground state.

3.4.1.3   Assigned Kinetics and Overview

The light induced and time-resolved IR spectroscopy in the *CaChR1* wild-type and its variants enable the assignment of the (-)1760 cm^{-1} (C=O region) and (+)2544 cm^{-1} (S-H region) vibrational modes to the D202 and C174 amino acids, respectively. The global fit analysis and the time constants of the kinetics of the *CaChR1* wild-type are shown in Figure 3.18.

The 1760 cm^{-1} kinetic shows a decaying behaviour with the first two time constants from Table 3.1 ($\tau_1^{1800-1510} = 2.7$ μs and $\tau_2^{1800-1510} = 37$ μs). The (+)2544 cm^{-1} kinetic shows a growing behaviour during the first two time constants $\tau_1^{2600-2500} = 0.8$ ns and $\tau_2^{2600-2500} = 83$ μs (Table 3.1 S-H range), indicating the protonation of the C174. The decay behaviour of 2544 cm^{-1} happens between $\tau_4^{2600-2500}$ and $\tau_5^{2600-2500}$, indicating the release of the proton. The results suggest that D202 deprotonation and C174 protonation take place during the transition from the P$_1^{590}$ to P$_2^{380}$ intermediate state.

The Figure 3.19 show the kinetics of the two negative vibrational modes of the S-H absorption range. Unlike the (+)2544 cm^{-1} , the negative kinetics 2560 and 2570 cm^{-1} show intense signal from the initial stages, indicating that the deprotonation or hydrogen bonding of one or more cysteines take place even before the time resolution (ns) of our experiment. But no conclusive statement can be made, since the signal of these kinetics can have contribution and be overlapped with heat contributions from within the sample medium. The recovery of the 2560 and 2570 cm^{-1} kinetics are faster than that of the (+)2544 cm^{-1} kinetic, the 2560 cm^{-1} shows full recovery by $\tau_4^{2600-2500}$

Figure 3.18: Selected kinetics of vibrational bands from time-resolved IR spectroscopy. The 1759 cm^{-1} in blue and 2544 cm^{-1} in red. The kinetics corresponds to the deprotonation of D202 and protonation of C174, respectively. The time constants from Table 3.1 are indicated in the kinetics. The data were collected after laser excitation at 532 nm.

and 2570 cm^{-1} at $\tau_5^{2600-2500}$. We were not able to do a conclusive assignment of these two negative modes (2560 and 2570 cm^{-1}). However, we suggest that C173 together with one of the other cysteine amino acids present in *CaChR1*, could be involved in the formation of these vibrational modes due to deprotonation or hydrogen bonding changes.
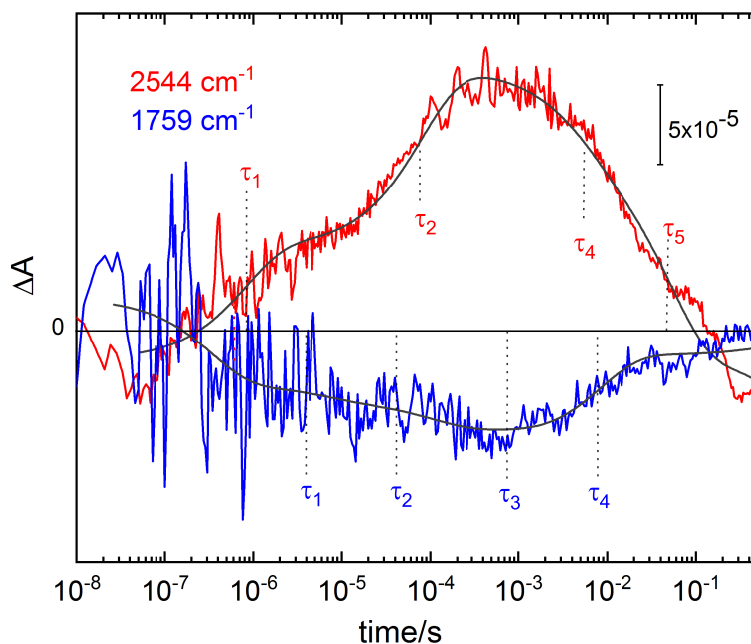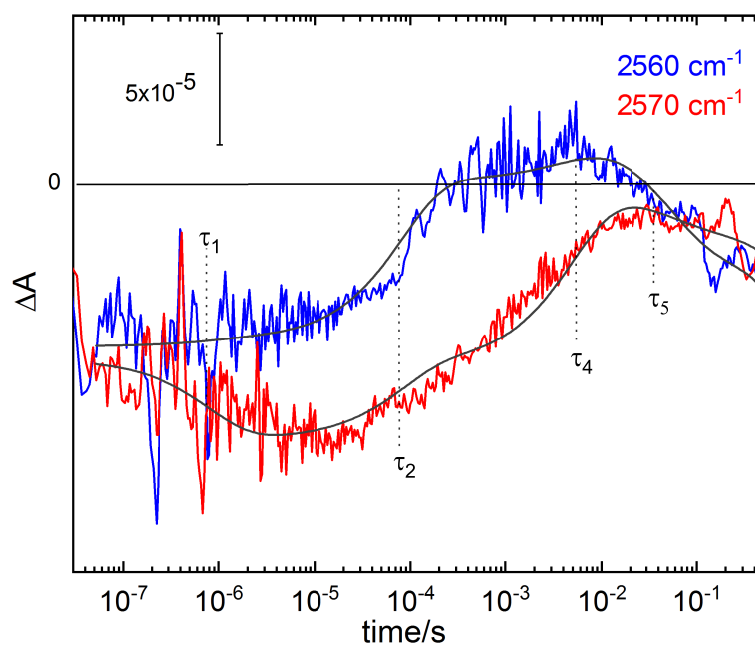
Figure 3.19: Selected kinetics of vibrational bands from time-resolved IR spectroscopy. The 2560 cm^{-1} in blue and 2570 cm^{-1} in red. The time constants from Table 3.1 are indicated in the kinetics. The data were collected after laser excitation at 532 nm.

3.4.2 Extracellular Side Amino Acids

3.4.2.1 C=O Vibrational Range

In Figure 3.20 the data of D299N and D299E variants in the C=O vibrational range (1800-1690 cm^{-1}) are shown, the P$_1^{590}$ intermediate state of these variants were partially discussed by Ref. [39, 40]. Both variants show divergences in P$_1^{590}$ and P$_2^{380}$ intermediate in comparison to the wild type (Figure 3.20). In the P$_1^{590}$ intermediate spectra of the D299N and D299E variants (Figure 3.20) positive vibrational modes are present at (+)1738 cm^{-1} for D299N and at (+)1728 cm^{-1} for D299E. The negative bleach around 1720 cm^{-1} in the wild type is down-shifted in both variants to (-)1716 cm^{-1} in D299N and (-)1710 cm $^{-1}$ in D299E. As suggested by Ogren et. al. [39], here we also observe the down-shift of the (+)1704 cm^{-1} band to 1696 cm^{-1} for both variants (D299N/E), indicating the assignment of this vibrational mode (1704 cm^{-1}) to the protonation of the D299 amino acid in the transition from ground state to P$_1^{590}$ intermediate [39].

In the P$_2^{380}$ spectra of D299N and D299E (Figure 3.20) no strong changes or new bands are observed in comparison with the P_1^{560} intermediate spectra. The D299N variant maintains the stronger positive mode at (+)1738 cm^{-1} frequency. On the other hand, for the D299E variant the strongest positive mode is found at frequency (+)1728 cm^{-1}, in the same position as the wild type. Both variants have the (-)1760 cm^{-1} band in the exact same position as the wild type. For the D299N variant, the (-)1710 cm^{-1} vibrational mode is missing or could be up-shifted to (-)1716 cm^{-1} frequency.

In figure 3.21 the P$_1^{590}$ and P$_2^{380}$ spectra of E136Q and E169Q variants are shown. In the E136Q variant, the absence of the 1704 cm^{-1} band is remarkable and a strong 1700 cm^{-1} band in the P$_1^{590}$ spectra is also of note. These changes could be related with the up-shift of the (-)1696/8 cm^{-1} vibrational mode, which could result in an overlap with the (+)1704 cm^{-1} vibrational mode, justifying the vanishing of the positive band (1704 cm^{-1}). In the transition from the P$_1^{590}$ to P$_2^{380}$ intermediate state no new bands were
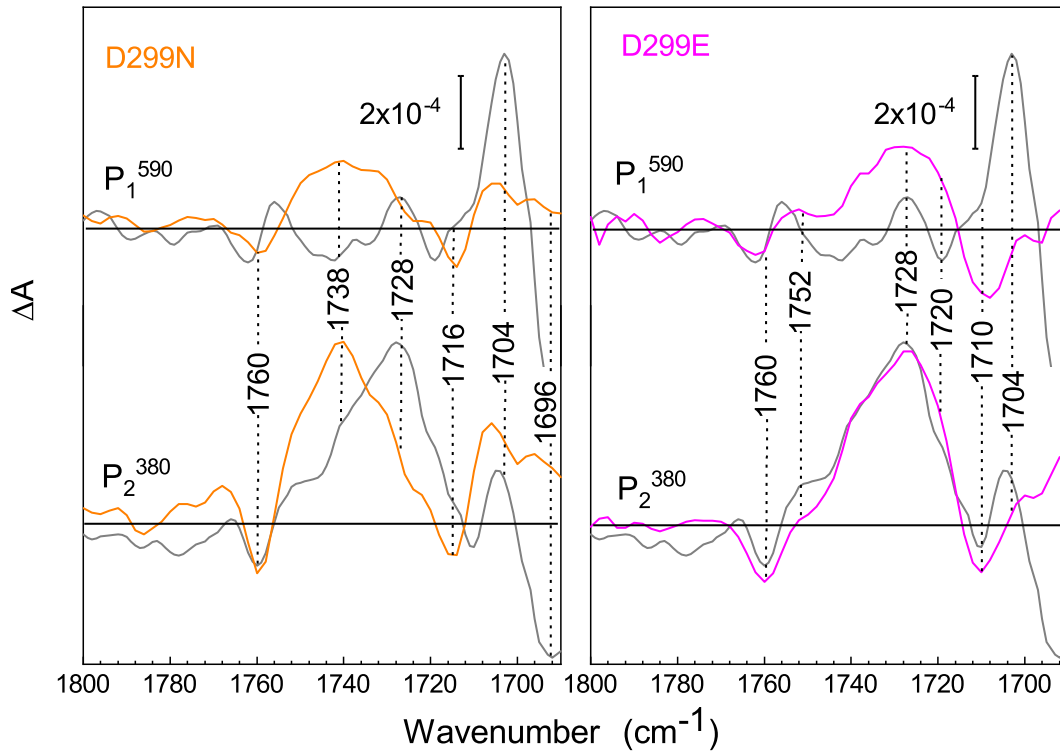
Figure 3.20: Time-resolved IR absorbance changes in *CaChR1* variants during the photocycle in the 1800-1690 cm^{-1} range. (A) D299N (orange trace) and (B) D299E (pink trace), the wild type spectra were repeated in gray trace. The spectra show the maximum absorption of the *CaChR1* wild-type and variants in the P$_1^{590}$ and P$_2^{380}$ intermediate state.For clarity and to reduce the signal-to-noise ratio the raw data were smoothed for the spectral resolution of 4 cm^{-1}. The samples were excited by a YAG laser at 532 nm.

observed, beside a small positive mode at 1738 cm^{-1} and the decreased in intensity of the (-)1710 cm^{-1} band. In addition, the presence of a broad positive shoulder with small intensity in the 1740-1710 cm^{-1} range is notable. The (+)1728 cm^{-1} band, which is the strongest vibrational mode in the wild type spectrum , is completely vanished for the E136Q variant, suggesting the assignment of this band as the protonation of the E136 amino acid.

Similar behavior to the E136 variant is followed by the E169Q variant in the P$_1^{590}$ spectrum (Figure 3.21B). For E169Q, is possible distinguish the presence of two negative vibrational modes at ~1708 and 1696 cm^{-1}, the latter with less intensity than the first. In the P$_1^{560}$ spectrum the vibrational modes at 1704 cm^{-1} and 1720 cm^{-1} are

Figure 3.21: Time-resolved IR absorbance changes in *CaChR1* variants during the photocycle in the 1800-1690 cm^{-1} range. (A) E136Q (navy-blue trace) and (B) E169Q (cyan trace), the wild type spectra were repeated in gray trace. The spectra show the maximum absorption of the *CaChR1* wild-type and variants in the P$_1^{590}$ and P$_2^{380}$ intermediate state.For clarity and to reduce the signal-to-noise ratio the raw data were smoothed for the spectral resolution of 4 cm^{-1}. The samples were excited by a YAG laser at 532 nm.

also missing, similar results were discussed by Ref. [40]. As already observed by Ref. [33, 34], the P$_2^{380}$ spectrum of the E169Q variant is similar to the wild type in the 1780-1730 range, however, it has a lower intensity signal for its positive peak around the 1728-1714 cm^{-1} range in comparison to the wild-type. Additionally the (-)1696/8 cm^{-1} band that has strong signal in the wild type spectrum, show a small intensity for the E169Q variant.

3.4.2.2 S-H Vibrational Range

Figure 3.22 shows the corresponding pure P$_2^{380}$ spectrum of the carboxylic variants (D299N, D299E, E136Q and E169Q) in the S-H vibrational range. Unexpectedly, all

carboxylic variants show changes and influences in the S-H range. The variants here have a similar behavior to that shown by the light-induced FTIR results (Figure 3.7).

The spectrum of the D299N variant (Figure 3.22(a)) has only one negative mode with a maximum at (-)2562 cm^{-1}. The main positive mode is shifted from 2544 cm^{-1} to 2530 cm^{-1} and a small shoulder appears at (+)2550 cm^{-1}. The maximum accumulation of P$_2^{380}$ intermediate state of D299E variant (Figure 3.22(b)) shows two intense negative modes at (-)2569/(-)2562 cm^{-1} and a small positive mode at (+)2548 cm^{-1}.

In the S-H vibrational range the time-resolved IR spectrum of the P$_2^{380}$ intermediate state is only weakly affected by the E136Q variant (see Figure 3.22(c)). As well as D299E, the pure P$_2^{380}$ spectrum of E169Q has strong differences from wild-type (see Figure 3.22(d)). The (+)2544 cm^{-1} mode is down-shift to (+)2526 cm^{-1}, the E169Q spectrum has only one negative mode at (-)2564 cm^{-1}. The variants that present large differences compared to the wild type (D299N, D299E and E169Q) are those in proximity to cysteine amino acids positioned in the middle core of the trans-membrane (C109, C133, C134 and C173 - see Figure 1.3). This reinforces the interpretation that the replacement of D299 and E169 by other amino acids can affect the nearby cysteines [116], which could cause H-bonding reorganization and consequently changes in the S-H vibrational range.
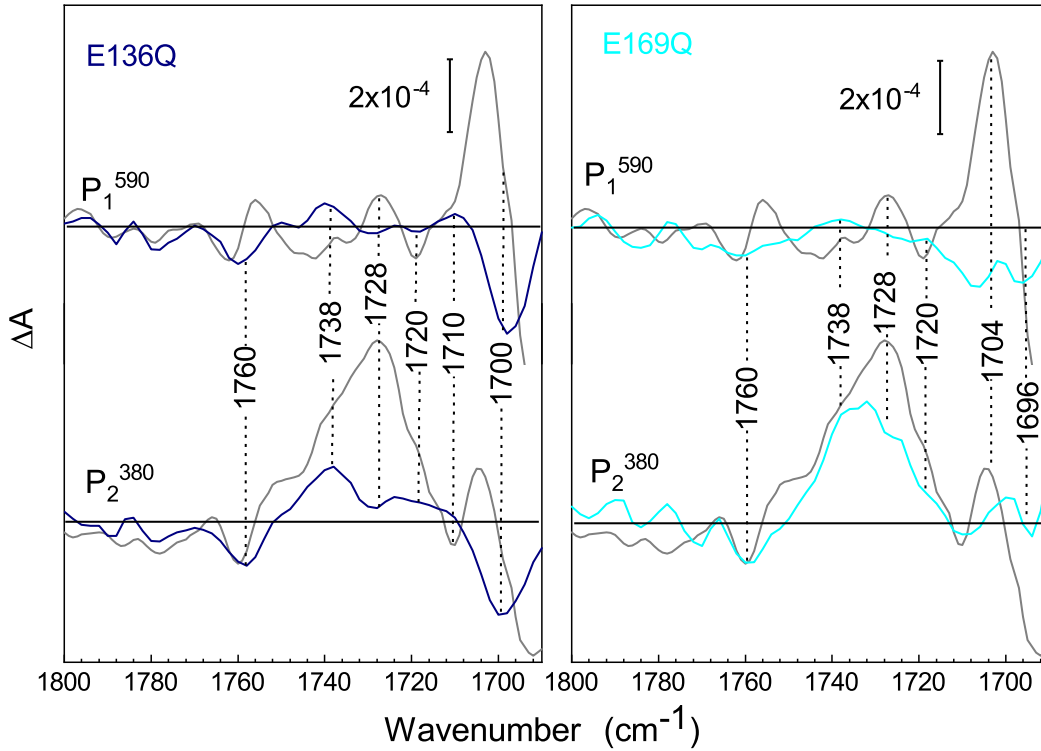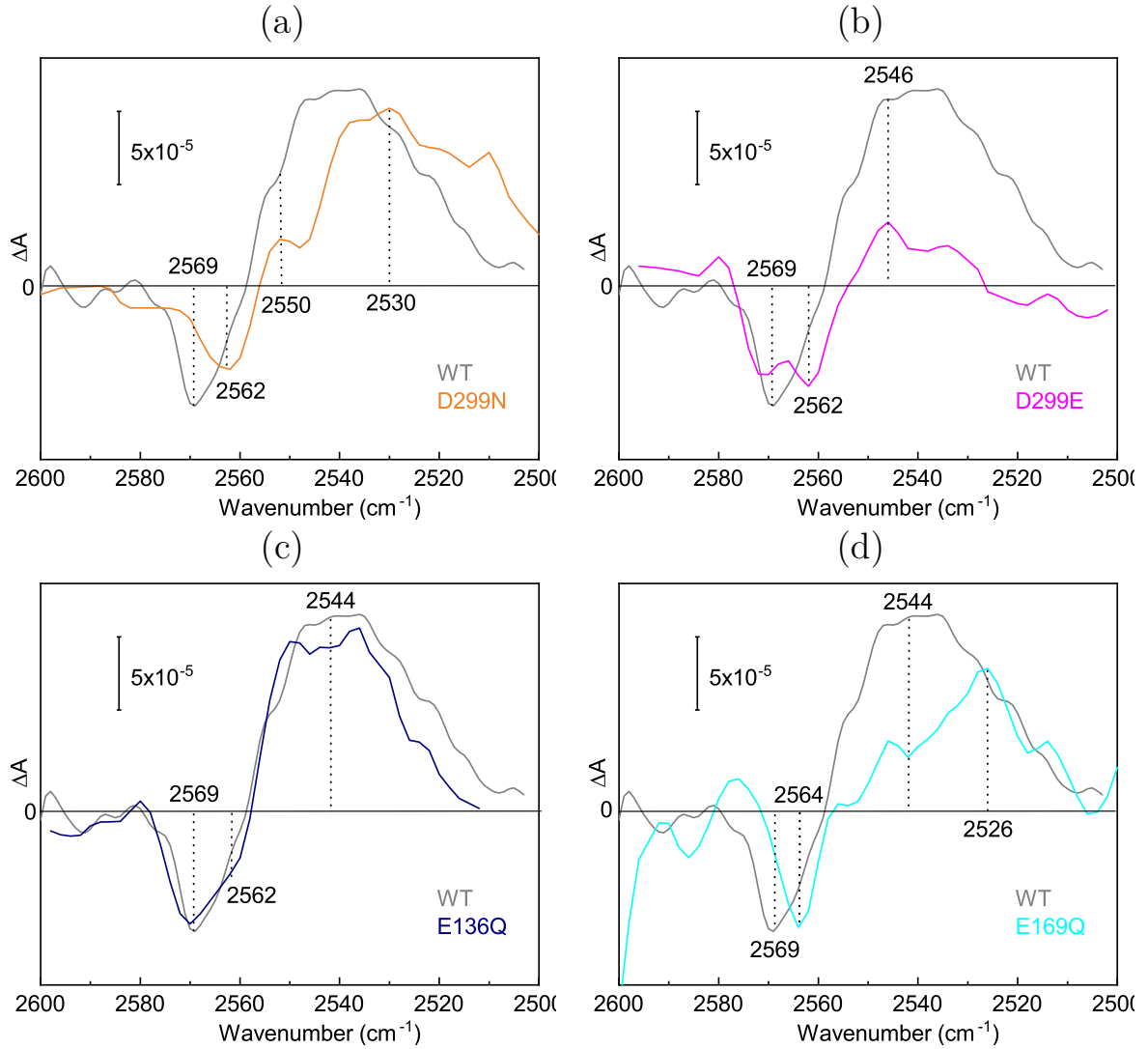
Figure 3.22: Time-Resolved IR absorbance changes in *CaChR1* variants during the photocycle in the 2600-2500 cm^{-1} range. (a) D299N (orange trace), (b) D299E (pink trace), (c) E136Q (navy-blue trace) and (d) E169Q (cyan trace), the wild type spectrum was repeated in gray trace. The data show the maximum absorption of the *CaChR1* wild-type and variants in the P$_2^{380}$ intermediate state. For clarity and to reduce the signal-to-noise ratio the raw data were smoothed for the spectral resolution of 4 cm^{-1}. The samples were excited by a YAG laser at 532 nm.

3.4.2.3 Assigned Kinetics and Overview

In Figure 3.23 the 1704 cm^{-1} and 1728 cm^{-1} kinetics of the *CaChR1* wild-type are shown. The 1704 cm^{-1} kinetic is assigned to the protonation of D299 in the early P$_1^{590}$ intermediate state [39, 40] and a strong signal from its early stages, suggesting that the protonation of the D299 amino acid takes place even before the *ns* time scale, in

agreement with the studies performed by Stensitzki et. al. [116]. The 1704 cm^{-1} kinetic shows a two step decay behavior in the range of $\tau_2^{1800-1510} = 37\ \mu$s and $\tau_3^{1800-1510} = 0.77$ ms time constants (Table 3.1).

The 1728 cm^{-1} kinetic (Figure 3.23) assigned as the protonation of E136 amino acid, has no signal during the early times and displays growth between the first two time constants $\tau_1^{1800-1510} = 2.7\ \mu$s and $\tau_2^{1800-1510} = 35\ \mu$, indicating that the protonation of E136 occurrs during the transition from P$_1^{590}$ to P$_2^{380}$ intermediate state.
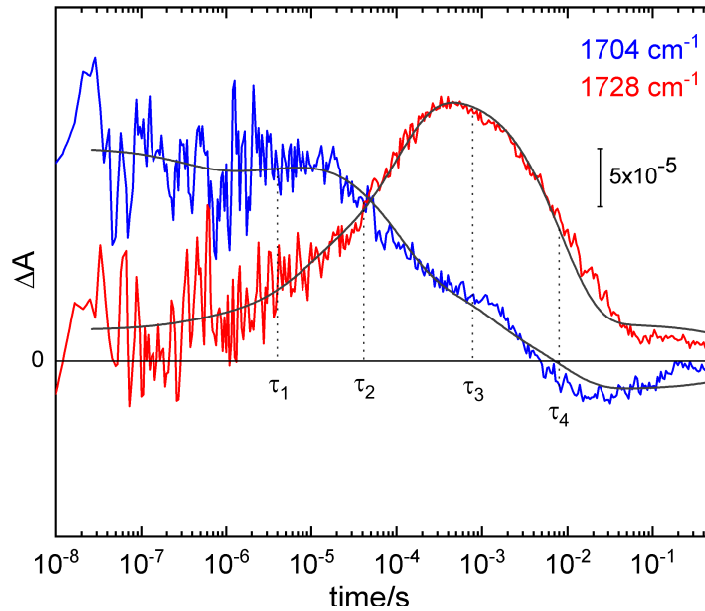
Figure 3.23: Selected kinetics of vibrational bands from time-resolved IR spectroscopy. The 1704 cm^{-1} in blue and 1728 cm^{-1} in red. The kinetics at 1704 cm^{-1} corresponds to the decay of the D299 after the protonation at the P$_1^{590}$ intermediate state and 1728 cm^{-1} protonation of the E136. The time traces were subjected to global analysis and the curve fit are show in grey lines. The time constants from Table 3.1 are indicated. The data were collected after laser excitation at 532 nm.

In Figure 3.24 the 1698 cm^{-1}, 1710 cm^{-1} and 1720 cm^{-1} kinetics of the *CaChR1* wild-type are show. The 1710 cm^{-1} kinetic has no signal in early times, but evolves to a negative signal in the ms time range. Unlike 1710 cm^{-1}, the 1698 cm^{-1} kinetic shows a fast decay in early stages.The 1698 cm^{-1} kinetic shows a greater difference in absorption over time while the 1720 cm^{-1} kinetic evolves to a positive signal. Here, we suggest the assignment of 1720 cm^{-1} vibrational mode to the E169 [39], but the modes

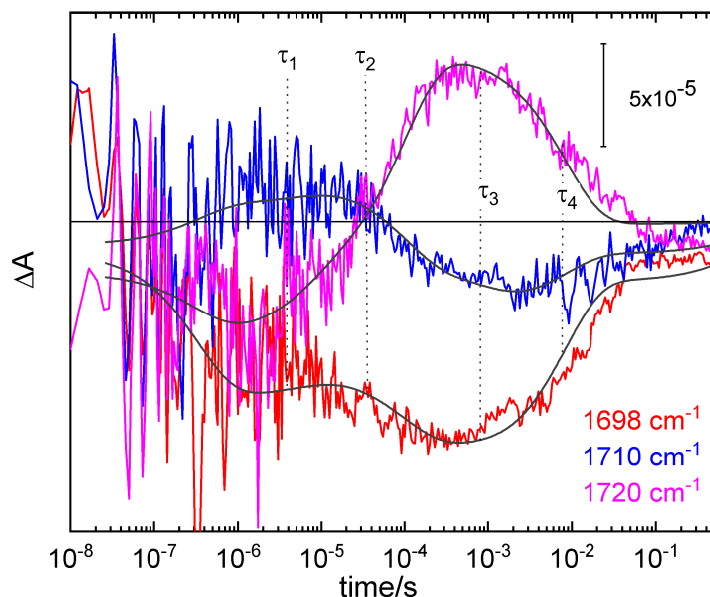at 1698 cm^{-1} and 1710 cm^{-1} can not be fully assigned.

Figure 3.24: Selected kinetics of vibrational bands from time-resolved IR spectroscopy. The kinetics 1698 cm^{-1} in red, 1710 cm^{-1} in blue and 1720 cm^{-1} in magenta. The time traces were subjected to global analysis and the curve fit are show in grey lines. The time constants from Table 3.1 are indicated. The data were collected after laser excitation at 532 nm.

Based on our data, two points need to be discussed regarding the influence of the E169 amino acid in the *CaChR1* photocycle. First, the E169 is presumably protonated in the ground state (pK$_a$ value $\simeq$9) [24] and would be deprotonated in early stages of the P$_1^{590}$ intermediate state [39, 116].

During the photocycle E169 is reprotonated, which could result in a positive vibrational mode. In the *CaChR1* wild-type, the band at 1720 cm^{-1} evolves to a positive signal during the transition to the P$_2^{380}$ intermediate state (Figure 3.24 - 1720 cm^{-1}), which overlaps with the main positive mode at 1728 cm^{-1}, assigned to the E136 amino acid. One possibility is that the mode at 1720 cm^{-1} indicates the reprotonation of E169 in the transition from P$_1^{590}$ to P$_2^{380}$ intermediate state, making it the proton acceptor of the Schiff Base during the transition to the P$_2^{380}$ intermediate state.

The second point of discussion is the vibrational modes in the lower range (1690-1710 cm^{-1}) of the E169Q and E136Q variants that could be caused by difference bands of the introduced glutamine (Q) in replacement of a glutamic acid (E). Due to the

replacement, the positive mode at higher wavenumbers (like 1704 cm^{-1}) could be slightly down-shifted and overlapped with the negative vibrational mode at 1696/8 cm^{-1}. The negative mode of the amide I could be shifted and superimposed into the vibrational modes of the carboxylic amino acid, this is supported by the lack of strong vibrational modes in the C=O vibrational range [39, 40]. Another interpretation for the changes in the lower range of E169Q spectra (1690-1710 cm^{-1} - Figure 3.21) is that the D299 amino acid is protonated (1704 cm^{-1} vibrational mode) by the E169 in the transition from ground state to P$_1^{590}$ intermediate [39, 116], because the replacement of E169 for a glutamine (Q), this proton transfer could not take place or be delayed sufficiently. Consequently, the (+)1704 cm^{-1} vibrational mode would also be missing or shifted for the E169Q variant, reinforcing the assignment of (+)1704 cm^{-1} mode to the protonation of the D299. On top of this a negative band at 1690 cm^{-1} was assigned as the deprotonation of E169 in the transition from ground state to P$_1^{590}$ [116], justifying the missing of a strong negative mode in the lower frequency range on the E169Q variant.

The time-resolved IR data suggests that the E169 amino acid is protonated in the transition from the P$_1^{590}$ to P$_2^{380}$ intermediate by the Schiff base, in the same time range that E136 would be protonated by other amino acid. Here, the D299 amino acid is the strongest candidate to be the proton donor to E136, generating the vibrational mode at 1728 cm^{-1}. Thus, D299 needs goes through a deprotonation function in the transition from the P$_1^{590}$ to P$_2^{380}$ intermediate state, which would generate a negative vibrational mode. A possible indication of the deprotonation of D299 amino acid could be the mode at (-)1698 cm^{-1}. Such a low vibrational energy in carboxylic amino acids occurs only in quite specific situations, when the C=O group must interact with an H-bonding donor and the O–H group must be H-bonded to a strong acceptor [117, 130]. The frequencies lower than the C=O strenching region (< 1700 cm^{-1}) have been reported for carboxylic groups only in two situations: a) when the H-bonding donor is the NH$_3^+$ group from a lysine [117, 130] and b) when the H-bond acceptor is a COO$^-$ group [131].

Thus, we suggest a similar behaviour of *CrChR2* [37], here the terminal carboxylate of E169 is the H-bond acceptor of protonated D299 in the P_1^{590} intermediate state of *CaChR1*. The negative mode 1696/8 cm^{-1} would indicate the breaking of this H-bond and the deprotonation of D299, which would transfer the proton to E136 amino acid. Thus, the deprotonation of the D299 and the Schiff base would coincide or be within a similar time range as the protonation of E136 and E169 amino acids.

3.5 General characterization of DsLOV-M49S

An experimental approach is required to solve the intermediates involved in the covalent bond formation that leads to the rise of the adduct state in LOV domains. For this, were employed light-induced FTIR spectroscopy, Time-Resolved IR spectroscopy using EC-QCL and Flash photolysis UV/Vis spectroscopy. An advantage in using the variant of *Dinoroseabacter Shibae* LOV domains is the short dark state recovery lifetime of DsLOV-M49S compared to others LOV domains. This unique characteristic facilitates the time-resolved experiments that typically require many repetitions for signal averaging.

Blue-light excitation induces the formation of a covalent bond between the C_{4a} atom of the FMN and the thiol side chain of C72, generating the cysteinyl-adduct state. This is accompanied by changes in the vibrational modes of the FMN cofactor and the apo-protein, as recorded by light-induced FTIR difference spectroscopy (Figure 3.25). Under the light excitation and the formation of the cystenyl-adduct state, large changes are induced in the dipole moment of the FMN chromophore and the apo-protein. Since the FMN is the largest dipole of the DsLOV-M49S system, it is expected that the strongest difference bands in the light-induced IR difference spectrum (Figure 3.25) are originated by the FMN chromophore with small contributions of the protein moiety.

In the light-induced FTIR difference spectrum of DsLOV-M49S, the negative vibrational modes are originated from the dark state (1710, 1672, 1645, 1580, 1550, 1404, 1350, 1270, 1248 and 1221 cm^{-1}) whereas positive vibrational modes originate from contributions of the adduct state (1724, 1682, 1655, 1622, 1533, 1514, 1454, 1425, 1328, and 1301 cm^{-1}). The good agreement between the DsLOV-M49S spectrum in Figure 3.25 and published spectra of other LOV domains [51, 66, 132] allowed the respective assignment of vibrational modes show in Table 3.2.

As already mentioned, besides the influence of molecular changes in the FMN chro-
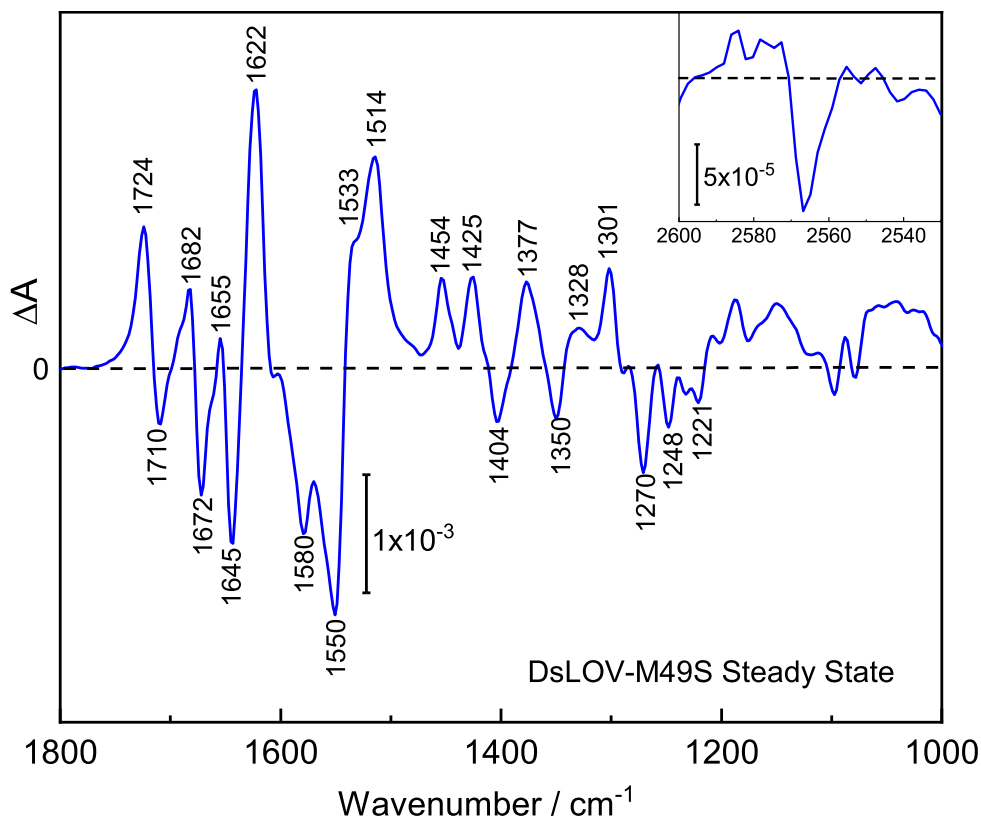
Figure 3.25: Light-induced FTIR difference spectrum of DsLOV-M49S from 1800 – 1000 cm^{-1}. The inset depicts the spectral range of the S-H stretching vibration from 2600 – 2500 cm^{-1}. The spectrum was recorded at 24 °C under continuous illumination with an LED emitting maximum at 460 nm. The indicated frequencies are summarized and assigned in Table 3.2

mophore, the vibrational modes can also have contribution of the apo-protein. This could cause deviation in the band positions in relation to other LOV domains [51, 66, 132]. This may arise from changes in the vibrational frequencies of the amide I (1690-1620 cm^{-1}) and amide II (1570-1520 cm^{-1}) of the protein backbone and also by possible changes in the FMN moiety.

The (-)1550 cm^{-1} and (-)1580 cm^{-1} modes originate from collective C=N and C=C stretching vibrations of the isoalloxazine ring of FMN in the dark state [56, 150]. The former vibrational mode (at (-)1550 cm^{-1}) shows a (-)2 cm^{-1} deviation in comparison with the LOV1 and LOV2 from *Chlamydomonas reinhardtii* and the LOV domain of *Bacillus subtilis* [51]. The (-)1672 cm^{-1} mode is assigned for C$_2$=O stretching vibrations in the dark state and shows a (-)4 cm^{-1} deviation in relation to the frequencies of the

Table 3.2: Band assignments of the molecular vibrations from Figure 3.25. The assignments were conducted based on known modes from previously published studies in (ν) stretching mode; (σ) bending mode.

IR dif. bands	Vibrational assignment
-2566	S-H[66]
+1724	C=O symmetric stretching (νC_4=O - mainly)[133]
-1710	C=O symmetric stretching (νC_4=O - mainly)[133, 134]
+1682	C=O asymmetric stretching (νC_2=O - mainly), $\sigma(N_3$-H)[135]
-1672	C=O asymmetric stretching (νC_2=O - mainly) $\sigma(N_3$-H)[133, 136, 137]
+1655	ν(C=O) (mainly C4=4)[133, 136, 137]
-1645	ν(C=O) (mainly C_2=O), $\nu(C_{10a}$=N), ν(C=C) ring I[66, 134, 138]
+1622	ν(C=O) (mainly C_2=O), ν(CC) ring I[133, 139, 140]
-1580	νC_{4a}=N_5), $\nu(C_4$-C_{4a}), $\nu(C_{10a}$-N_{10}) $\nu(C_{10a}$=N_1)[66, 134, 141, 142]
-1550	$\nu(C_{5a}$=N_6), $\nu(C_8$-C_9), $\nu(C_{10a}$=N_1), $\nu(C_{4a}$=N_5)[66, 134, 142]
+1533	$\nu(C_{4a}$=N_5), $\nu(C_{5a}$-N_5), $\nu(C_{10a}$=N_1), $\sigma(CH_3$)[138, 143]
+1514	ν(CC), ν(CN)[139, 143]
+1454	$\nu(C_2$-N_1), $\nu(C_2$-N_3), $\nu(C_{4a}$=C_4), $\sigma(CH_3$)[144]
+1425	$\nu(C_{4a}$=C_{10a})[143]
-1404	$\nu(C_4$-N_3), νC_4-C_{4a}), $\nu(C_2$-N_3), $\sigma(C_9$-H), $\sigma(C_4$=O)[141, 142, 145]
+1377	$\nu(C_{10a}$-N_{10}), $\sigma(N_3$-H)[146]
-1350	$\nu(C_{10a}$-N_{10}), $\nu(C_1$-N_{10}), $\nu(C_{5a}$=C_{9a}), $\nu(C_{10a}$=C_{4a})[134, 142]
+1301	$\nu(C_2$-N_1), $\nu(C_2$-N_3)[146]
-1270	$\nu(C_{5a}$-N_5)[147, 148]
-1248	$\nu(C_4$-N_3), $\nu(C_2$-N_3), $\nu(C_4$-C_{4a}), $\nu(C_2$-N_1), $\sigma(C_2$=O)[134, 142, 143]
-1221	$\nu(C_7$-CCH_3), $\nu(C_{10a}$-C_{4a}), $\nu(C_1$-N_{10}), $\nu(C_{9a}$-N_{10}), $\nu(C_2$-N_3)[134, 138, 143, 149]

LOV-domains investigated by Bednarz et. al. [51]. Besides the influence of the protein backbone, these small deviations can also be caused by the exchange of the methionine (M) amino acid at position 49 for a serine (S) in DsLOV.

Above the 1700 cm^{-1} frequency range the C_4=O stretching vibrations of the FMN carbonyl bond are found. These are of particular interest due to sensitivity not only to the triplet state but also to the adduct state formation. The C_4=O vibration mode shifts from (-)1710 cm^{-1} in the dark state to around (+)1724 cm^{-1} upon formation of

the adduct state. Thus, the $(+)1724$ cm^{-1} band can be use as an indirect proxy for the formation of the covalent bond between the reactive cysteine (C72) and the C_{4a}-FMN atom [66, 135, 151, 152]. The direct proxy to track the formation of the adduct state would be the ~1533 cm^{-1} vibrational mode. It is expected that this band goes through major changes during the transition of the C_{4a} from a planar configuration ($C_{4a}=N_5$) to a nonplanar tetrahedral configuration (C_{4a}-N_5). Thus, the 1533 cm^{-1} band indicate the arises of the C_{4a}-N_5 single bond upon adduct state formation [151, 153].

Unlike other LOV domains, DsLOV-M49S does not show strong vibrational modes at the 1680-1630 range in the light induced FTIR spectrum (Figure 3.25). Notice that the vibrational mode at $(+)1655$ cm^{-1} shows a small intensity in comparison with other LOV domains [51, 66, 140]. These differences could be due to the absence of the Jα helix in the DsLOV-M49S protein structure [78, 79], which, in other LOV domains, has its characteristic absorption bands in the range of 1700-1620 cm^{-1} after the formation of adduct state ($[LOV]^A$) [140, 152, 154]. The effect of the absent Jα helix in DsLOV-M49S will be discussed in more detail in the next sections with help of the time-resolved IR data.

For the covalent bond between the reactive cysteine and the C_{4a} atom of FMN take place, the deprotonation of the terminal thiol moiety in the cysteine side chain must previously take place. This appears in the light-induced difference spectrum as a negative band at 2566 cm^{-1} (inset Figure 3.25) [66]. Consequently, the $(-)2566$ cm^{-1} mode can be assigned as the deprotonation of C72, the only cysteinyl residue of DsLOV. The frequency of the S-H stretch of C72 in DsLOV-M49S is in the same frequency range as reported for other LOV domains [51, 66, 132, 135]. Light-induced FTIR investigations applied in LOV1 and LOV2 from *Chlamydomonas reinhardtii* found the S-H vibrations located at 2570 cm^{-1} and 2573 cm^{-1} [51], respectively. For the LOV domain from *Bacillus subtilis* it is located at 2569 cm^{-1} [51]. This indicates the DsLOV-M49S S-H terminal is in a stronger H-bonded environment than that observed in other previously mentioned LOV domains [51]. The negative intensity of the 2566 cm^{-1} band is an

indicative of the reactive cysteine (C72) which is protonated before the formation of the covalent bond with C_{4a}-FMN, this will be clarified further with the time-resolved IR data in the next section.

3.6 Time-Resolved Rapid-Scan in DsLOV-M49S

In order to investigate the back reaction of DsLOV-M49S to the ground state, rapid-scan experiments were performed across the time range of 9.5 ms – 10 s. For a cleaner graphic the spectra of the final seconds were omitted (Figure 3.26). The data was analyzed, with good reproduction, using a global fit with a single time constant.

Comparing the rapid scan data from Figure 3.26 with the light-induced FTIR data (Figure 3.25), we can affirm that both data sets are in agreement with each other about the bands position. In Figure 3.26 all bands from the chromophore and the apo-protein decay simultaneously. From the data analysis, the time constant for the dark state recovery in DsLOV-M49S was established as $\tau = 1.9$. This result is in agreement with the results shown by Fettweiss et. al. [79].
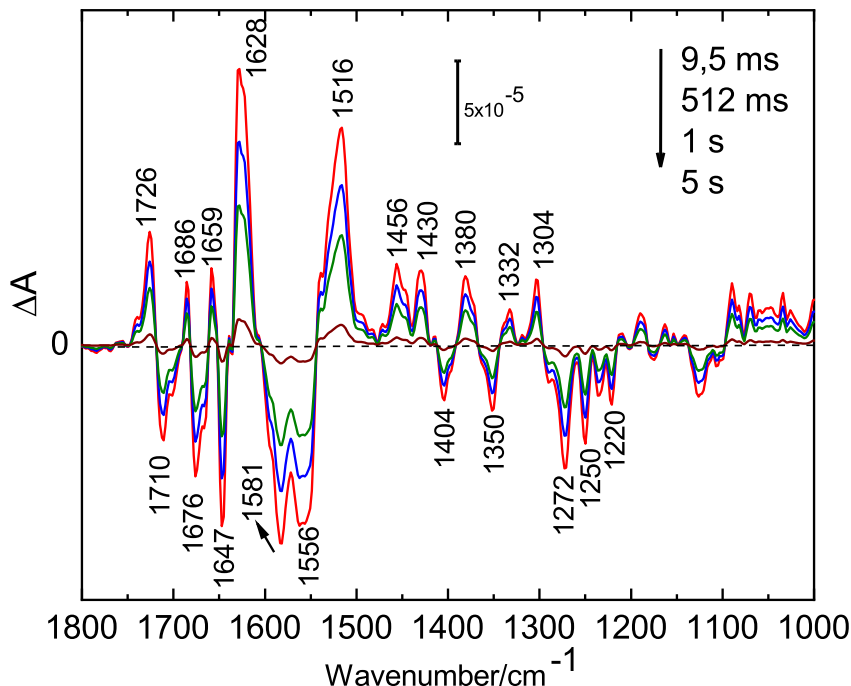
Figure 3.26: Sequence of difference spectra in the millisecond time range of DsLOV-M49S after blue light excitation (460 nm). The data was collected in the range of 9.5 *ms* to 10 *s* and shows the recovery of the DsLOV-M49S to the dark state.

In Figure 3.27 the kinetics of the (+)1516 and (+)1726 cm^{-1} vibrational modes are

shown. Beyond the kinetics, Figure 3.27 also features a second analysis using single exponential fit made individually of each kinetic, which provides the recovery time constant of 1.90 ± 0.24 s for the decay back to the ground state in DsLOV-M49S, which is in full agreement with the global analysis.

Figure 3.27: Kinetics and single exponential fit of the FTIR Rapid Scan experiment, using hydrated film of DsLOV-M49S. The kinetics are from the vibrational modes at 1726 cm^{-1} (blue) and 1516 cm^{-1} (red). The mono-exponential fit of the kinetics decay with time constant of 1.9 s.

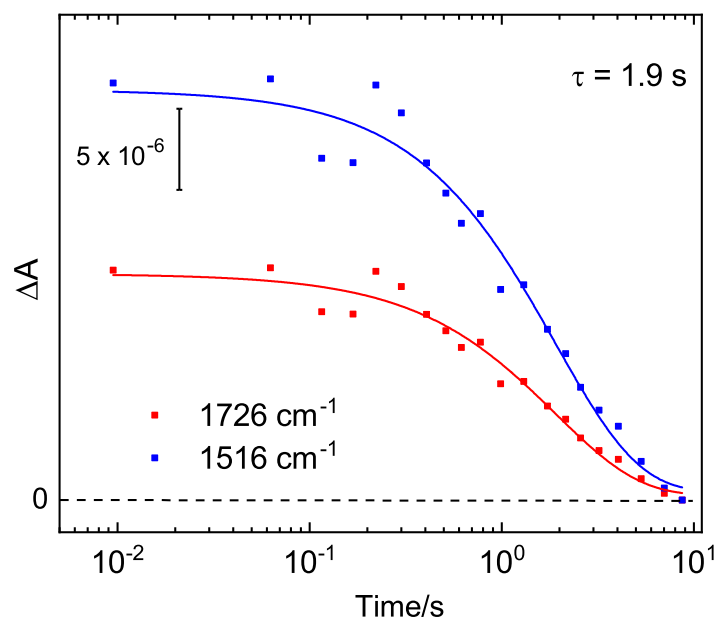# 3.7 Time-Resolved spectroscopy in DsLOV-M49S

The steady-state experiments discussed in the section 3.5 do not provide any information on the time scale of the light-induced changes. Thus, for a further investigation on the photo-intermediates of DsLOV-M49S it is essential to perform time-resolved IR spectroscopy. Here, we are using a self-built flash photolysis spectrometer employing the intense emission from tunable external cavity quantum cascade lasers (EC-QCLs). This method was chosen due to the high photon flux of QCLs [80] that facilitates the detection of contributions of single amino acids of interest, among them the weak S-H vibration of a cysteine residue.

The detection of the thiol residue is often hampered by the low extinction coefficient, ranging from ϵ = 10-200 $M^{-1}cm^{-1}$, the variations are dependent on the hydrogen-bonding properties of the solvent [155]. Our QCLs experiments cover the 2600-2520 cm^{-1} and 1800-1510 cm^{-1} spectral range. Thus, this time-resolved IR method enable us to solve the signature modes of the S-H stretching vibration (2600-2520 cm^{-1}), the amide I (mainly C=O) mode of the peptide backbone and the C=O and C=N stretching vibrations of FMN (1800-510 cm^{-1}). The time-resolved IR spectroscopy using EC-QCLs was performed over the time range of 100 ns – 500 ms, enabling the tracking of the triplet state decay and the formation of the cystenyl-adduct state of DsLOV-M49S. Besides the time-resolved IR data, this section also discusses the Flash-Photolysis UV/Vis data, which was recorded in the visible absorption range of 380-720 nm over the time range of 50 ns - 10 s.

3.7.1 S-H vibrational Range

Using EC-QCLs, the minute absorbance changes of the S-H vibration of DsLOV-M49S with nanosecond time resolution can be traced. The temporal evolution of the S-H vibrations is shown in Figure 3.28A, which shows selected slices of the spectra tracking the intensity increase of the vibrational mode at (-)2566 cm^{-1} until it reaches the maximum intensity.
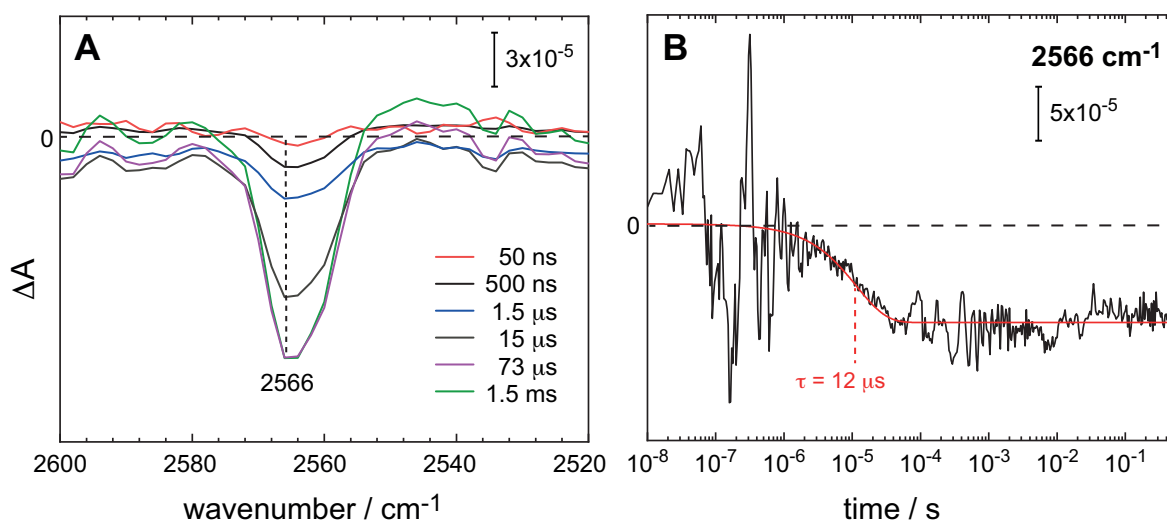

Figure 3.28: (A) Temporal evolution of the IR vibrational difference band of the S-H stretch of C72 of DsLOV-M49S recorded by time-resolved IR spectroscopy using a tunable EC-QCL, the sample was excited using a YAG laser at 460 nm. (B) The initial absorption at 2566 cm^{-1} (black trace) decays mono-exponentially into a plateau with a time constant of 12 ± 2 μs (red trace) indicating the deprotonation of C72. The time constant is indicated in the figure.

In Figure 3.28B, the kinetic of the (-)2566 cm^{-1} band is shown. The 2566 cm^{-1} kinetic clearly exhibits a single exponential decay with a time constant of τ= 12 ± 2 μs, indicated in the Figure 3.28B. The 12 μs time constant corresponds to the deprotonation of the reactive cysteine residue (C72) present in DsLOV-M49S. Due to the weak S-H vibrational signal, it is expected that the S-H signal is overlapped by contributions of broad IR-absorption due to heat transfer from the photo-excited sample to the surrounding aqueous medium. To overcome this issue and separate the pure kinetic signal of the (-)2566 cm^{-1} band from the heat-induced changes of the medium, an integration was performed of the absorption changes over the 2550-2520 cm^{-1} vibrational

range. The time trace obtained from the integration (Figure 3.29 - green trace) was subtracted from the 2566 cm^{-1} kinetic. The kinetic after the subtraction is shown in Figure 3.29 in blue, which shows only a small deviation in early times in comparison with the original kinetic (Figure 3.29 - black trace).
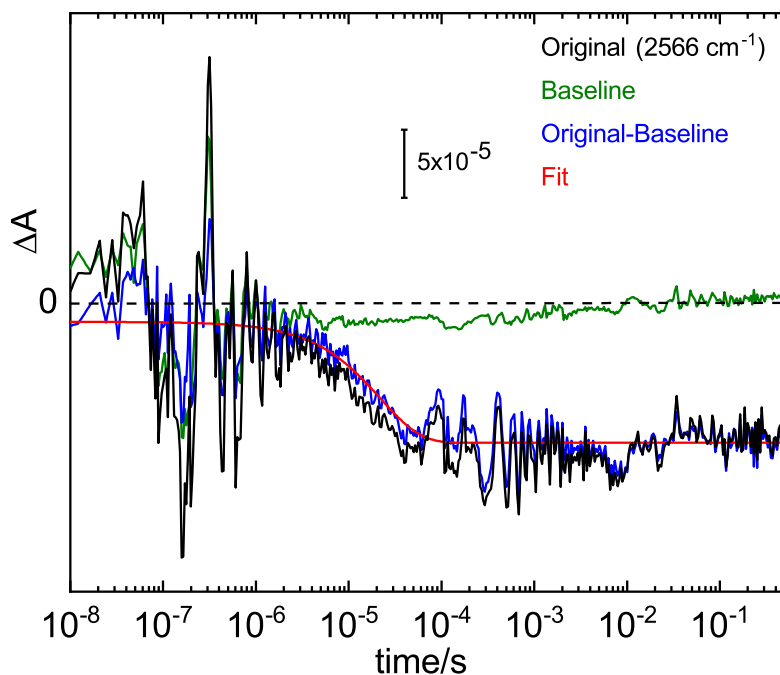
Figure 3.29: Original kinetic of the deprotonation band of the cysteine at 2566 cm^{-1} (black) shows signal interference due to heat-induced changes from the medium (water). To elimitate this interference, we integrated the absorption changes across the range of 2550-2520 cm^{-1} and then subtracted this time trace (green) from the original kinetics at 2566 cm^{-1}. The subtraction of these time traces is shown below in blue and the single exponential Fit of the subtraction curve in red.

In Figure 3.30, the spectra of the S-H vibrational range are compared, which were collected by light-induced FTIR (blue spectrum) and time-resolved IR spectroscopy at 1.5 ms (black spectrum). The time at 1.5 ms was selected arbitrarily taking into account that the deprotonation of the reactive cysteine had already occurred. Both spectra were collected using different techniques yet the frequency of the S-H vibrational band is exactly the same at (-) 2566 cm^{-1} (Figure 3.30(a)).

The S-H stretching mode of DsLOV-M49S shows an asymmetric shape, similar to that of the LOV1 domain from *Chlamydomonas reinhardtii* [51]. Consequently, a more detailed

Figure 3.30: (A) Comparison between time-resolved QCL data at 1.5 ms (black spectrum) and the FTIR light *minus* dark differ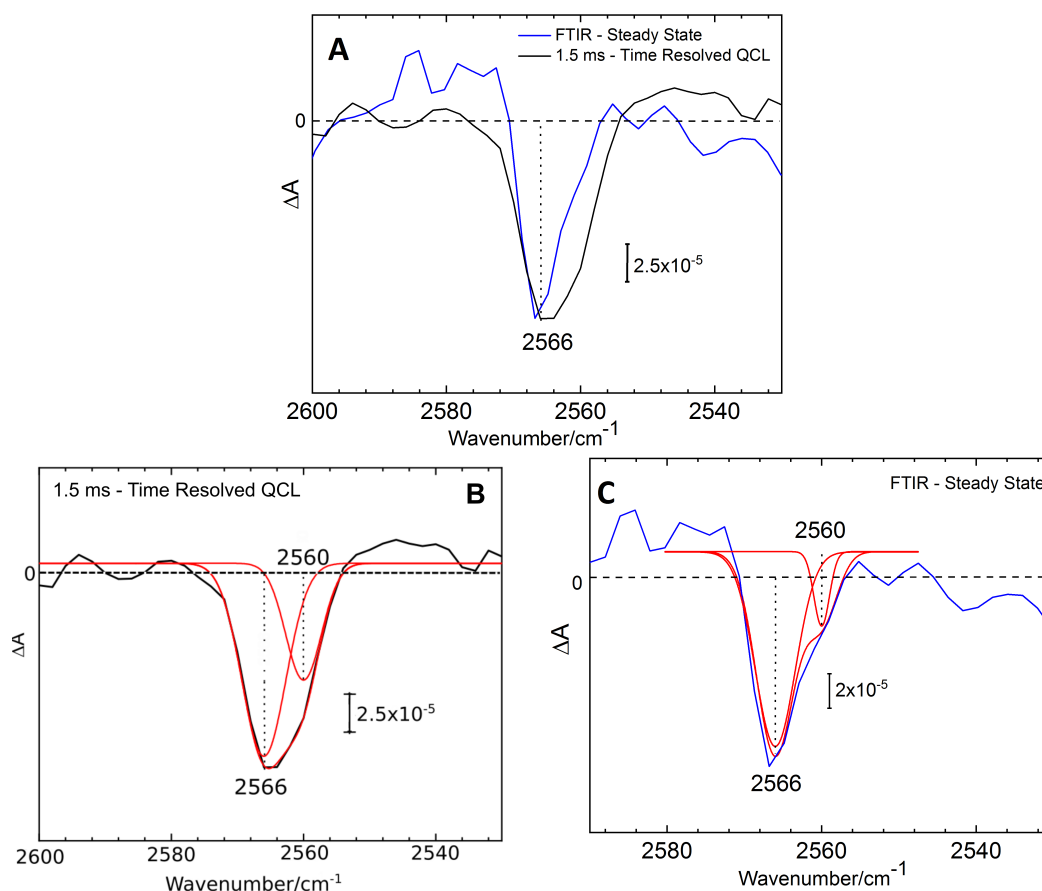ence spectrum in the range of the cysteine S-H stretching vibration (blue spectrum). Data collected from the two different experiments are in good agreement regarding the position of the S-H band at 2566 cm^{-1}, indicating a strong hydrogen-bonding environment. The FTIR light *minus* dark difference spectrum was scale in relation to the time-resolved QCL data. (B) IR difference spectrum at 1.5 ms (black) of the vibrational band of the S-H stretch of C72 of DsLOV-M49S recorded by time-resolved flash photolysis using a tunable EC-QCL. The spectrum has been fitted by the sum of two Gaussians. The relative areas are 67% for the band 2566 cm^{-1} and 33% for the band 2560 cm^{-1}. (C) FTIR steady state light minus dark difference spectrum of the vibrational band of the S-H stretch of C72 of DsLOV-M49S. The spectrum has been fitted by the sum of two Gaussians. The relative areas are 79% for the band 2566 cm^{-1} and 21% for the band 2560 cm^{-1}.

analysis was conducted, performing a Gaussian fit on the S-H stretching mode as shown in Figure 3.30B and C. The Gaussian fit was only adequate when two Gaussian were used, reveling two minima at (-)2566 and (-)2560 cm^{-1}, with the relative areas of each band being 67% and 33%, respectively, for the time-resolved IR data (Figure 3.30B). And for the FTIR steady state (Figure 3.30C) the relative areas are 79% (2566 cm^{-1}) and 21% (2560 cm^{-1}). The results of this analysis are comparable to those found for

LOV1 from *Chlamydomonas reinhardtii* [51].

The detection of two different S-H bands in DsLOV-M49S is in accordance with the possibility that C72 has two different rotamer conformations [78, 79], as is the case in several LOV domain structures [53, 74, 154]. Depending which conformation is adopted by the cysteine amino acid, the distance between the S-Cys and the C_{4a}-FMN atoms can differ [53, 74, 154]. For the DsLOV wild-type, the crystal structure shows just one conformation [79]. However, for those variants in which the original methionine (M) amino acid is replaced by an amino acid with smaller size, as like a serine (S), more conformational freedom is given to C72, enabling it to adopt both conformations [79]. In the DsLOV-M49S the S-H (-)2566 cm^{-1} band corresponds to a C72 surrounded by an environment with moderate hydrogen bonding strength. On the other hand, the (-)2560 cm^{-1} band corresponds to a strong hydrogen bonding environment, suggesting that the conformation of the second rotamer leads to a lower pK_a of the thiol group.

3.7.2 Triplet and Adduct states vibrational modes

The decay of the triplet state and the rising of the adduct state were monitored using two experimental techniques. Time-resolved IR spectroscopy using EC-QCLs in the 1800-1510 cm^{-1} range and the Flash Photysis UV/Vis spectroscopy in the 720-380 nm range. In the latter experiment, no data was collected over the 440-500 nm interval, which was excluded due to the proximity of the wavelength used as the excitation energy (460 nm) of the DsLOV-M49S. Thus, the 400-500 nm range was skipped to avoid damage the detector and light scattering.

Table 3.3: Time constants of the DsLOV-M49S photoreaction derived from time-resolved IR spectroscopy. The global analysis was applied to the kinetics in the 1800 – 1510 cm^{-1} range and 380-730 nm range.

τ(s)/spectral range	1800-1510 cm^{-1}	730-380 nm
τ_1 ([LOV]$^3 \rightarrow$ [LOV]^A)	18 μs	13 μs
τ_2 ([LOV]$^3 \rightarrow$ GS)	83 μs	196 μs
τ_3 ([LOV]^A)	510 μs	–
τ_4 ([LOV]$^A \rightarrow$ GS)	1.9 s	0.56 s

The data sets of both experiments were analysed in similar way by global analysis using a model with a branched triplet decay and no radical. To perform the analysis using the branched triplet decay, two possible pathways were defined, one of the decay pathways leads to the formation of the adduct state while the other restores the ground state in a 4:1 ratio, respectively. The data analysis was performed together with *David Ehrenberg.* The obtained time constants are listed in Table 3.3. The reaction scheme showing the two decays was chosen based on lifetime density analysis (LDA) [94] (Figure 3.31) and testing of other models with global analysis (Figure 3.32).

To perform the LDA [94] the following equation was used

$$min|D * \chi - A| \tag{3.1}$$

where *A* is the data matrix and *D* contains a finite number of exponential decays

$(e^{(-t/\tau_i)})$ minimized in favor of χ. Due to a huge number of lifetimes, we used the Tikhonov regularization. From the analysis a resulting pre-factor for each wavenumber is obtained, which are then plotted as a contour plot (Figure 3.31 shows the 1800-1590 cm^{-1} vibrational range). 200 logarithmically spaced time constants, ranging from 10^{-7} up to 10^{-1} s, were used for the calculations. In Figure 3.31 the more intense blue and red areas denote that the contribution of exponential decays are high at these wavenumbers. Thus, the vertical lines suggest possible transitions of intermediates or decays back to the ground state associated with a large spectral changes. Which can be interpreted as the rise and/or decay of the intermediate states as well as the decay back to the ground state.
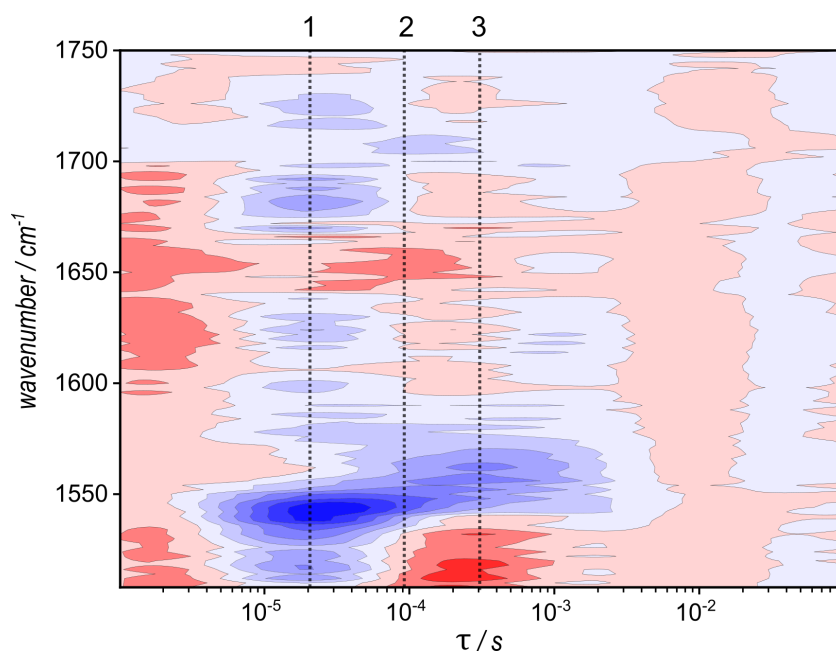
Figure 3.31: Lifetime density analysis of infrared data obtained by time-resolved IR spectroscopy employing EC-QCLs. The calculations were done using algorithm written in Python by *David Ehrenberg*. For DsLOV-M49S 200 logarithmically spaced time constants were used, ranging from 10^{-7} up to 10^{-1} s. The vertical lines indicate the lifetime densities that can be associated with a large spectral changes.

The first vertical line indicated in Figure 3.31 (1 = $\sim$20 μs) are associated with spectral changes involving a vibrational mode around 1726 cm^{-1}, assigned to the C$_4$=O vibration in the adduct state formation. The third vertical line indicated (3 = $\sim$ 560 μs) is related to spectral changes associated at the same wavenumbers as at vertical line 1 combined

with spectral changes in the region around 1555 cm^{-1}. The changes observed in the line 3 could be an indication that further changes are expected in the adduct state. This is contrasted by the second vertical line (2 = $\sim$100 μs) where spectral changes at different wavenumbers are associated. At the second line the changes are concentrated in two regions, at $\sim$1710 cm^{-1} and around 1655 cm^{-1}, these frequencies are assigned to the C$_4$=O vibration in the ground state and C$_4$=O of the triplet, respectively. The changes here can be indicative of an additional concurrent decay from the triplet directly back to the ground state.
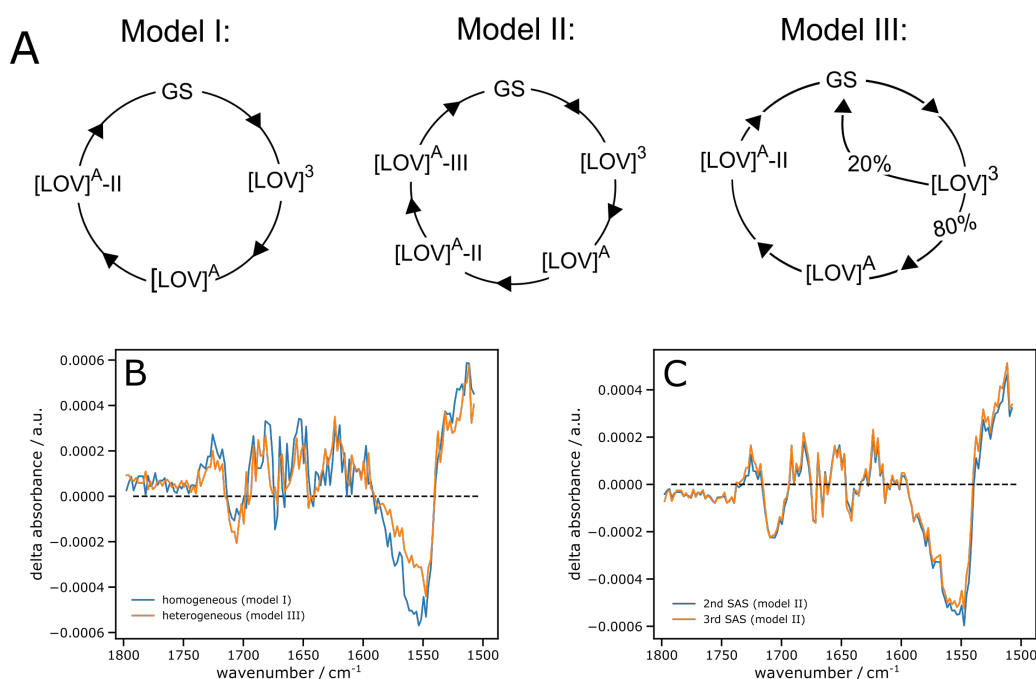
Figure 3.32: (A) Schematic reaction models used for global target analysis. Model I and II are simple sequential reactions schemes. Model I has three components and Model II has 4 components, before the decay back to the ground state (GS). Model II interprets the spectral changes associated with time 2 of the LDA analysis as an additional intermediate. Model III assumes heterogeneity in the triplet state with fixed populations. This means that part of the triplet state decay back to the GS and the other part goes through two more intermediates ([LOV]^A and [LOV]^A-II) before the decay to the GS. (B) Second SAS ([LOV]^A) considering the homogeneous triplet state population (model I - blue trace) and heterogeneous triplet state population (Model III - orange trace). (C) Second ([LOV]^A - blue trace) and third ([LOV]^A-II - orange trace) SAS of the model II.

To perform the global analysis a certain number of singular components are fitted with a defined number of exponential decays. Figure 3.32A schematically shows the models

used to perform global analysis.

The first two models (Figure 3.32A - I and II) are simple sequential reaction schemes where model II interprets the spectral changes associated with the second vertical line of Figure 3.31 ($\sim$100 μs) as an additional intermediate. Fitting the infrared data with model I resulted in a R^2 of 97.24%. Including an additional intermediate raised the R^2 to 97.58%. On the other hand, model III gives a R^2 of 97.40%, here we considers a branch photocycle where part of the triplet state decays to form the adduct state and a second part decays directly back to the ground state as shown in the scheme of Figure 3.32. Should be noted that including additional exponential decays will always improve R^2, making an inspection of the species associated spectra (SAS) necessary (Figure 3.32B and C). For model II (Figure 3.32C), the SAS for $[LOV]^A$ and $[LOV]^A$-II are shown, here the fit did not converge satisfactorily showing almost identical second ($[LOV]^A$) and third ($[LOV]^A$-II) SAS. Thus, introduction of an additional intermediate is not justified and this model was discarded. We further analyzed the time-resolved UV/Vis data with these models. Here, only the reaction scheme model III gave satisfying results with a R^2 of 99.51%.

Choosing a branching ratio of 4:1 in model III for analysis of the infrared as well as of the UV/Vis data yielded the best results. Considering both the LDA and the results of the global analysis, we conclude that the reaction scheme model III describes our data best and is used as a model throughout this work. Other studies have also considered the branched reaction model. Gil et al. [56] in the investigation of the LOV domain from *Avena sativa*, were able to fit time-resolved infrared data with a branched triplet decay but excluded the model due to a discrepancy between a short decay of the triplet back to the ground state and a long-lived triplet upon mutation of the cysteine to a valine [56]. In our case, the triplet decay to the ground state is in agreement for an unquenched triplet state. Contrary to the interpretation of Gil et. al. [56], Kutta et al. [156] favored the decay of the radical anion intermediate back to the ground state with the same 4:1 ratio after a thorough analysis of UV/Vis data in the LOV1 wild-type

and variants from the green alga *Chlamydomonas reinhardtii* [156].

The branching is indicative of cysteine residues with more than one rotamer orientation, as observed in crystal structures of LOV domains from *Chlamydomonas reinhardtii* and *Avena sativa* [53, 154]. Although the crystal structures of DsLOV do not reveal populations of rotamers, it has been discussed that the cysteine residue can adopt the two different conformations in the DsLOV wild-type and M49S [78, 79].

However, it was shown by MD simulations that the two rotamers in *Avena sativa* phototropin 1 LOV2 interconvert on the nanosecond timescale [157]. Song et. al. [157] described that the reactive cysteine residue was flipping rapidly from one conformer to the other, presenting a dynamic equilibrium. Consequently, it seems unclear if in DsLOV the rotamers would be more stable. As already discussed previously, our IR data in the S-H vibrational range present an asymmetric shape indicating the presence of two rotamers. It may well be that crystallization forces the protein to adopt just one conformation, while in solution both are populated. This possibility is also supported by the asymmetric band shape of the S-H stretching; the fit using two Gaussians provides two minima at 2566 cm^{-1} and 2560 cm^{-1} (Figure 3.30), indicating that C72 can have different rotamer orientations, as seen in the results of LOV1 from *Chlamydomonas reinhardtii* [51].

3.7.2.1 Time-Resolved UV/Vis spectroscopy

Figure 3.33 shows the global fit analysis of the flash photolysis UV/Vis raw data, which were extracted the species associated spectra (SAS) and the concentration profile. The global analysis suggested that the DsLOV-M49S photocycle can be described with two distinct intermediate states. The three characteristic absorption bands of the triplet state (390, 660 and 720 nm) can be recognized in the SAS of Figure 3.33A (blue trace). The red show only one absorption maximum at 390 nm, characteristic of absorption by the adduct state. The kinetic traces providing information about the vibrational

Figure 3.33: (A) The decay associated spectra showing the key intermediate states of the DsLOV-M49S photoreaction recorded by time-resolved UV/Vis spectroscopy. The estimated spectral contributions (dots) show 2 step decay of the first spectral component. The $[LOV]^3$ spectrum (blue) shows characteristic absorbance bands in the 500-720 nm range, whereas the $[LOV]^A$ (red) spectrum show the characteristic adduct absorption band at 390 nm. (B) Concentration profiles of $[LOV]^3$ (blue) and $[LOV]^A$ (red) obtained by global Fit analysis applied on the time-resolved UV/Vis absorption spectra of DsLOV-M49S. The sample was excited using a YAG laser at 460 nm.

changes will be discussed later.

3.7.2.2 Time-Resolved IR spectroscopy using EC-QCLs

Figure 3.34 shows the SAS of time-resolved IR data according to our model. The spectrum in black corresponds to the triplet state [50, 56, 137, 140], which is formed even before the ns time range that the time-resolved IR data had been recorded. Here, like in the Flash Photolysis UV/Vis data, we can track the decay of the triplet state and the raising of the adduct state.

The (-)1548 cm^{-1} and (-)1580 cm^{-1} bands (Figure 3.34) are assigned as the collective C=N and C=C stretching vibrations of the isoalloxazine ring of FMN in the ground state [56, 150]. The vibrational modes at (-)1710 cm^{-1} and (-)1676 cm^{-1} are assigned to the C_4=O and C_2=O carbonyl stretching vibrations in the ground state [50], respectively. Under the formation of the adduct state, these carbonyl modes are shifted from (-)1710 cm^{-1} to (+)1726 cm^{-1} (C_4=O) and from (-)1676 cm^{-1} to (+)1624 cm^{-1} (C_2=O) [50]. The (+)1654 cm^{-1} and (+)1624 cm^{-1} bands are assigned as the carbonyl vibrations in the triplet ([LOV]^3) un-protonated state [50, 56, 137, 140]. Thus, the decay of the triplet state can be followed observing the behaviour of these vibrational modes.

The triplet state decays within 18 μs and the adduct state [LOV]^A (Figure 3.34 - red trace) is formed, comparing both intermediates ([LOV]^3 and [LOV]^A) deviations can be observed. Here, two new positive bands are found at frequencies ~1684 cm^{-1} and 1726 cm^{-1} in the adduct state ([LOV]^A) spectrum. The latter band, as already mentioned, is assigned to the C_4=O stretching vibrations and indicates the formation of the adduct state [137].

Based on the characteristic marker bands observed in the SAS of Figure 3.34, we can exclude the formation of an intermediate with a protonated triplet state. This finding is due to the absence of the three vibrational modes for the C=O vibrations, which are expected in the protonated triplet state [50, 140]. Instead, in the triplet state spectrum (Figure 3.34 - black trace) only two vibrational modes are observed at (+)1654 cm^{-1} and (+)1624 cm^{-1}, characteristics of the neutral triplet state [50, 140].
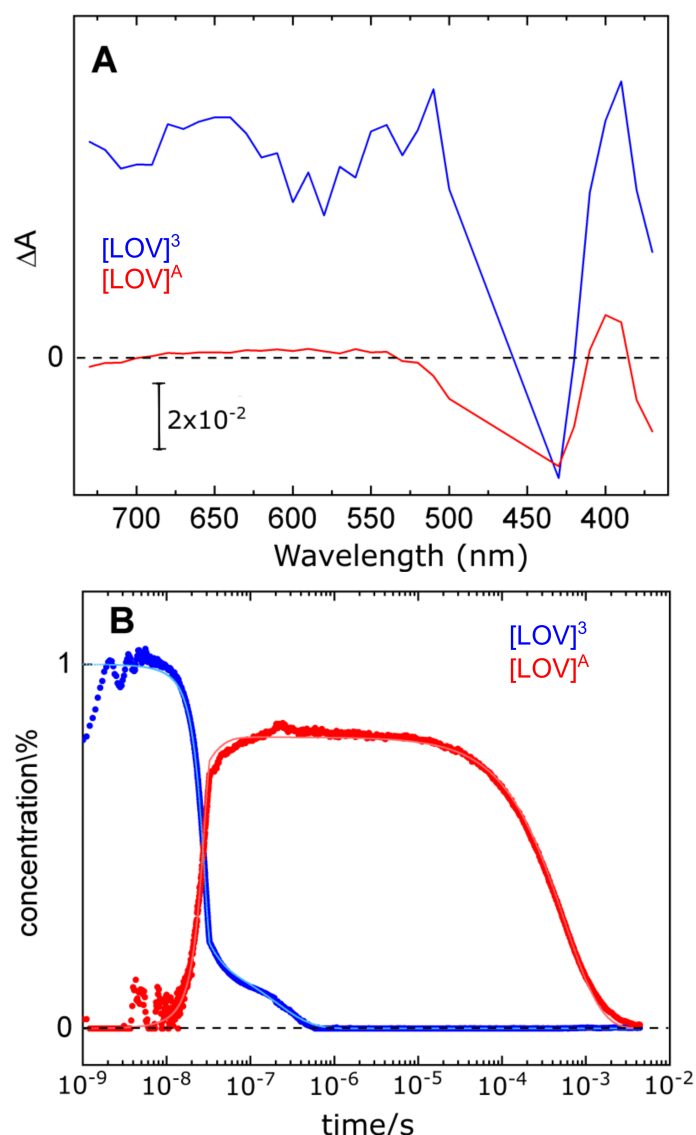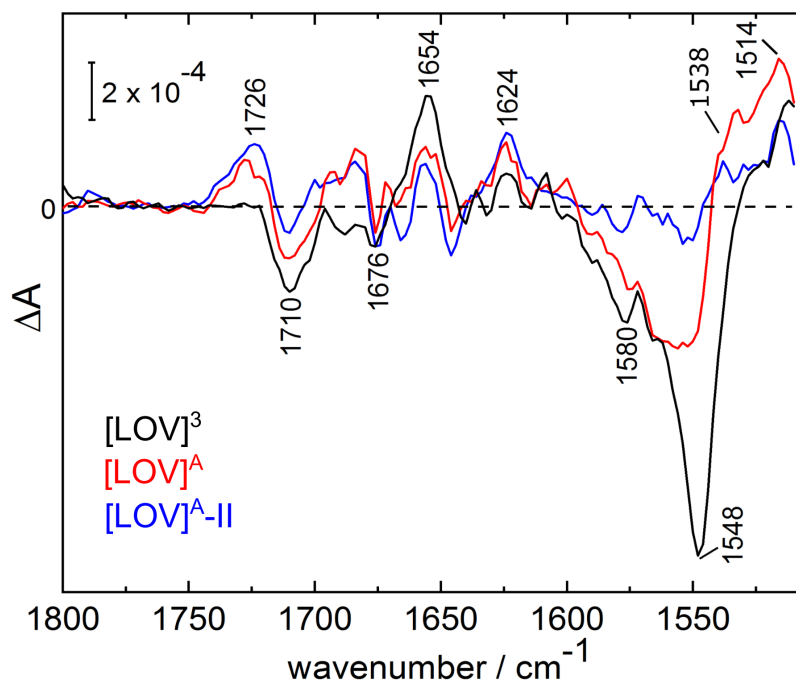
Figure 3.34: Species associated spectra (SAS) showing the key intermediate states of the DsLOV-M49S photoreaction recorded by time-resolved IR spectroscopy. Corresponding time constants are listed in Table 3.3. The black spectrum corresponds to the vibrational changes of the dark state to the triplet state ([LOV]^3) and the red spectrum to the adduct state ([LOV]^A). The blue spectrum refers to the second adduct state ([LOV]^A-II), deviating from the first one mainly in the spectral range of 1580 - 1520 cm^{-1}. The SAS shown here were smoothed with factor 2. The sample was excited using a YAG laser at 460 nm.

In the time-resolved IR data, indications of an additional intermediate state in the transition from the triplet state to the adduct state were not observed. However, the possible formation of a flavin neutral radical (FMN$^\bullet$) and the flavin anion radical (FMN$^{\bullet-}$) intermediates during this transition cannot be ruled out. These two radical (neutral and anion) species have been characterized spectroscopically in solution. The anion radical generated by the photoreduction of FMN by ethylenediaminetetraacetic acid disodium salt dihydrate (EDTA) shows a prominent vibrational mode at (+)1633 cm^{-1} [140], which slightly shifts to (+)1636 cm^{-1} due to solvent effects if the flavin anion radical is generated using riboflavin tetraacetate (RBTA) in CD$_3$CN [137]. On the other hand, the spectrum of the neutral radical generated by RBTA in CD$_3$CN has two marker bands at (+)1660 cm^{-1} and (+)1620 cm^{-1} [137], close to the band positions

detected in our data (+)1654 cm^{-1} and (+)1624 cm^{-1} and are potentially obscured by triplet vibrations. However, it may well be that these states are insufficiently populated for the signal to be detectable in a time-resolved experiment.

In Figure 3.34 the fast recovery of the bands at (-)1580 and (-)1548 cm^{-1} is noticeable, while the other vibrational modes in the 1730-1600 cm^{-1} range remain practically constant, unlike the behavior observed in other LOV domains [158]. This conduct can be due to the structural differences and function of DsLOV-M49S. Molecular Dynamics Simulations by Freddolino et. al. [158] suggested that LOV1 and LOV2 show functional differences from each other. For LOV1 it was suggested that the activation is mostly caused by changes in the hydrogen bonding between protein and ligand. Whereas the LOV2 activation could also be influenced by changes in the flexibility of a set of protein loops [158].

The deviation in the 1730-1600 cm^{-1} range could be due to the unique structural characteristic and function of DsLOV-M49S. The DsLOV protein is originates from LOV1, the crystal structure shows a unique feature with the N-terminal A′α helix being part of the dimer interface [78]. In studies involving UV CD spectroscopy on the DsLOV wild-type in solution, the possibility of an increased flexibility of the N-cap region had been discussed [78, 79]. The increase in flexibility could result in an unfolding of the A′α helix in solution [79], similar to the structural changes observed to AsLOV2 that contain an N-terminal A′α helix and a C-terminal Jα helix [159]. Zayner et. al. [159] found that some side-chain displacements and changes in hydrogen-bonding patterns can be observed in the region near the chromophore and the amino-terminal A′α helix. Which could be interpreted as part of a structural signal, being the adduct formation the starting point of the unfolding of the A′α helix in solution [79].

Similar structural changes have been reported for AsLOV2 [159], including side-chain displacements and changes in hydrogen-bonding patterns in the chromophore binding pocket and the amino-terminus. These rearrangements are interpreted as a starting

point for changes in the A$'\alpha$ helix, which would contribute to the starting of the unfolding of the Jα helix [153]. Since DsLOV does not have a Jα helix, changes in the range from 1730 to 1600 cm^{-1} would be smaller or non-existing in comparison to other LOV domains that have a Jα helix [78, 79].

Swartz et. al.[151] suggested that the bands at (-)1580/(-)1548 cm^{-1} originate from the C$_{4a}$=N$_5$ stretching vibration with a contribution of C$_{10a}$=N$_1$ in the (-)1580 cm^{-1} band. Thus, these two bands are expected to be strongly affected by the formation of the adduct state, due to the conversion of the C$_{4a}$=N$_5$ double bond to a C$_{4a}$-N$_5$ single bond upon formation of the adduct state [151]. The exchange of a planar carbon (sp2 : C$_{4a}$=N$_5$) to a tetrahedral carbon (sp3: C$_{4a}$-N$_5$) would justify the strong changes observed in the (-)1580/(-)1548 cm^{-1} vibrational modes (Figure 3.34).

3.7.3 Kinetic Analysis

Figure 3.35 shows the main kinetics assigned to the triplet and the adduct state, detected by time-resolved IR and Flash Photolysis UV/Vis spectroscopy. The fits in Figure 3.35 were obtained from global analysis, as well as the time constants indicated that are also shown in Table 3.3. The triplet state formed in LOV domains has characteristic absorption bands in the UV/Vis at 390, 660 and 720 nm [53–55, 58]. In Figure 3.35A an exemplary decay of the triplet state recorded at 660 nm and $(+)1654$ cm^{-1} kinetic assigned to the C$_4$=O vibrations on the triplet state are shown. The vibrational changes observed for 1654 cm^{-1} proceed with a similar time course of the vibrational changes recorded at 660 nm, supporting not just its previous assignment to the C$_4$=O vibration in the triplet state but also the two-step decay of this state [56].

Figure 3.35B shows the 390 nm and 1726 cm^{-1} kinetics. The 390 nm kinetic has absorption information from both the adduct and the triplet state. Thus, the 390 nm kinetic shows a decay behavior with two clearly separate components, the first of which has a time constant of $\tau_{UV/Vis}^1 = 13$ μs, which reflects the decay of the triplet state and the second one at $\tau_{UV/Vis}^4 = 0.56$ s corresponding to the decay of the adduct state. The vibrational changes observed in the 1726 cm^{-1} band have information about the C$_4$=O vibration in the adduct state [LOV]^A [66, 135, 151], thus the increases of this mode indicate the rises of the adduct state. Here, the 1726 cm^{-1} vibrational mode rises with the same time constant as the decay of the triplet state, indicating that besides the adduct and the triplet state no other intermediate state is observable in the DsLOV-M49S time-resolved data.

As mentioned early the 1726 cm^{-1} is a indirectly proxy for the formation of the adduct state [137], a direct proxy would be the 1538 cm^{-1} band. Given that the 1538 cm^{-1} mode arises upon the disappearance of the C$_{4a}$=N$_5$ double bond and formation of the C$_{4a}$-N$_5$ single bond [151, 153]. In Figure 3.34 the 1538 cm^{-1} appears only as a shoulder overlap by the 1514 cm^{-1} band, the kinetics of adduct formation as evidenced by the
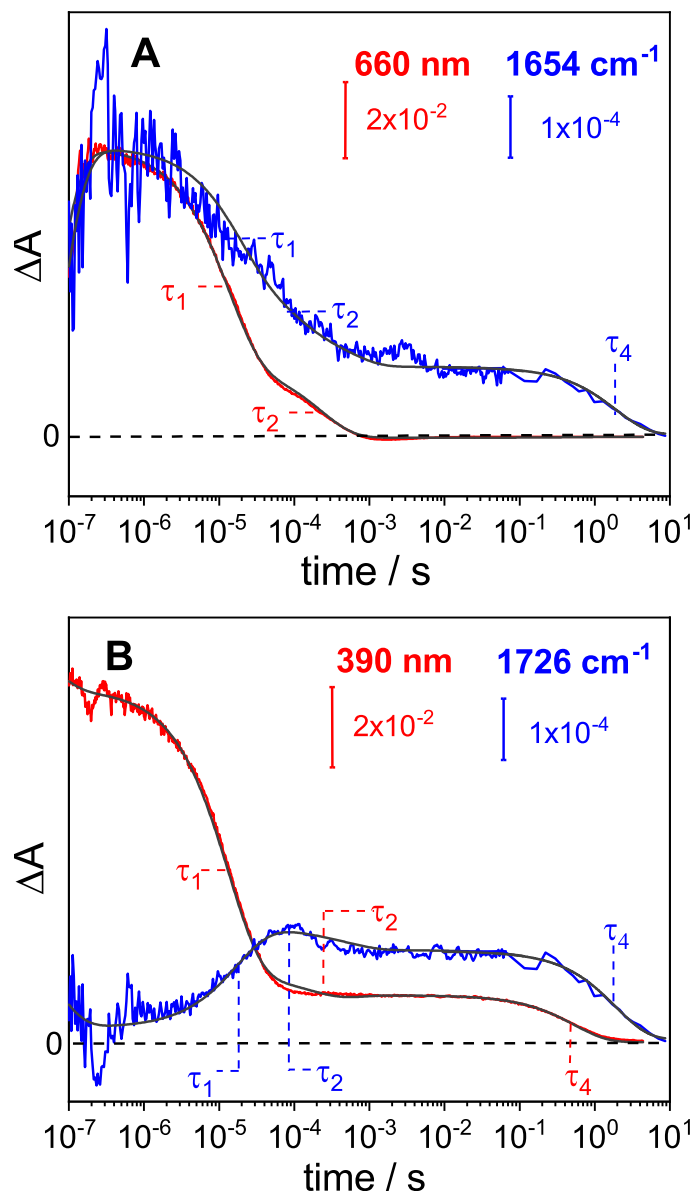
Figure 3.35: Selected kinetics of vibrational bands from time-resolved IR (blue) and UV/Vis (red) absorption experiments. The recorded kinetics were subjected to global fitting (grey smooth lines), the time constants indicated in the kinetics are show in Table 3.3. (A) The kinetics at 660 nm reflect the decay of the triplet state ($[LOV]^3$). The vibrational mode at 1654 cm^{-1} has been assigned to the $C_4{=}O$ vibration of triplet state. (B) The absorption change at 390 nm is also due to the decay of the triplet state and the formation of the adduct state, because both intermediate species have a characteristic absorption band at this wavelength. The kinetic at 1726 cm^{-1} follows the formation of the adduct state as the band has been assigned to the $C_4{=}O$ stretching vibration in the adduct state $[LOV]^A$ [77, 78]. The kinetic traces at single frequencies of the time resolved Rapid Scan data (Figure 3.26) have been extracted and appended to the QCL data to expand the time range of the latter into the ms and s time range. The kinetics were collected after laser excitation at 460 nm.

rise of the bands at 1726 cm^{-1} (blue trace in Figure 3.35B) and at 1538 cm^{-1} coincides with the deprotonation of C72 as derived from the S-H vibrational band at 2566 cm^{-1} (Figure 3.36).
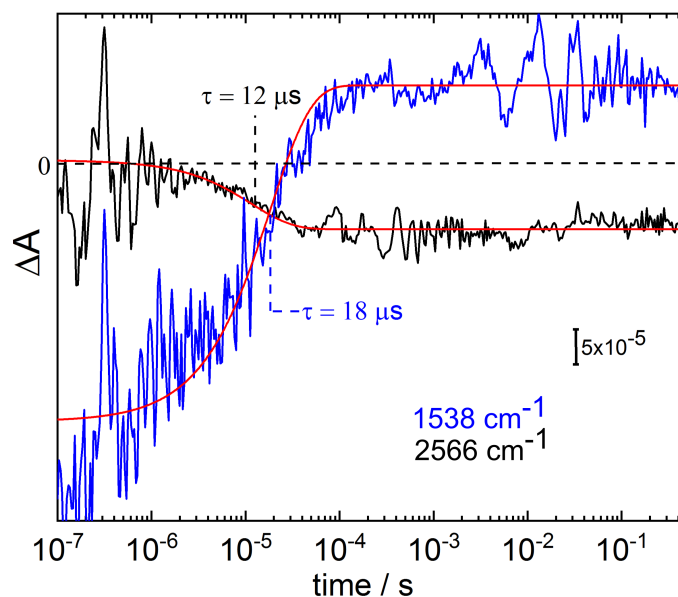

Figure 3.36: Kinetics of proton dissociation from C72 (black trace - $\tau = 12 \pm 2$ μs, replotted from Figure 3.28) and formation of the adduct state (blue trace - $\tau = 18 \pm 2$ μs). The band at 1538 cm^{-1} has been assigned to a vibrational mode with strong C_{4a}-N_5 stretching vibrational character that arises after the transition of C_{4a} to the non-planar sp^3 tetrahedral configuration. Consequently, this kinetic is a proxy for the formation of the adduct state. The single exponential fits provided by analysis using OriginPro are shown in red and the time constants of each individual exponential fit are indicated in the figure. The kinetics were collected after laser excitation at 460 nm.

Figure 3.37 shows additional kinetic traces of the 1800-1510 cm^{-1} range. Unlike the decay of the band at 1654 cm^{-1} (Figure 3.35), the kinetics of the other vibrational modes in the 1800-1510 cm^{-1} range increase in intensity with the early microsecond time range, reaching maximum intensity in the ms time range. The 1514 cm^{-1} kinetic (which is characteristic of the C=N and C=C vibrational modes) rises upon adduct state formation [152]. Here, its signal increases in intensity from the early stages, followed by a sharp decay. The bands at 1624 cm^{-1} and 1654 cm^{-1} (Figure 3.37A and 3.35, respectively), are assigned to the carbonyl vibrations of the triplet-excited state and decay upon adduct formation due to a shift to higher wavenumbers [135, 140]. At

early time points the 1624 cm^{-1} kinetic shows just a small positive signal with a time evolution similar to the kinetic of the band at 1514 cm^{-1}. Since the modes at (+)1654 and (+)1624 cm^{-1} originate from C=O vibrations, a similar behavior in the kinetics were expected. However, the differences can be attributed to the fact that the band at 1654 cm^{-1} mainly contains information on the vibrational changes of the C$_4$=O stretching mode, whereas the band at 1624 cm^{-1} contains a second contribution from the C=C stretching mode of ring I, as well as that of C$_2$=O. The negative kinetic of the 1548 cm^{-1} band originates from collective C=N and C=C stretching vibrations of the isoalloxazine ring within the FMN and the kinetic at 1710 cm^{-1} represents the C$_4$=O vibrations in the ground state. Both negative kinetics show a similar recovery in the interval of ms time range followed by a constant negative signal present until the end of the detection interval.
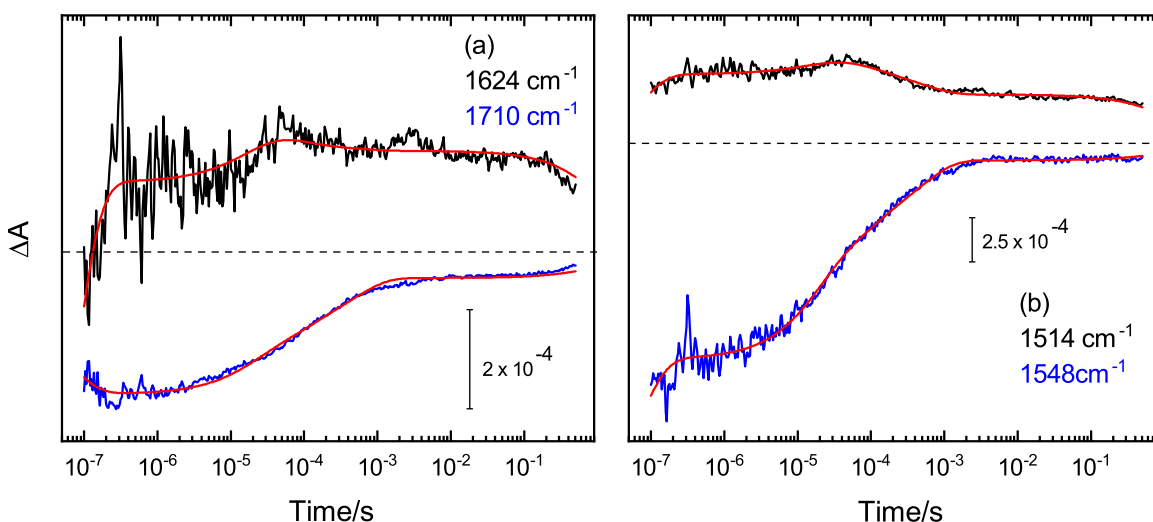
Figure 3.37: Selected kinetics of vibrational bands that arise in the range of 1800-1510 cm^{-1}. (a) The bands at 1624 cm^{-1} and 1710 cm^{-1} are assigned to the C$_2$=O vibrations of [LOV]^3 and vibrations of C$_4$=O of the ground state, respectively. (b) The bands at 1514 cm^{-1} and 1548 cm^{-1} originate from the collective C=N and C=C stretching vibrations of the isoalloxazine ring of FMN. The kinetics were collected after laser excitation at 460 nm.

As shown above, the time constants of the fast decay component of the triplet state and the formation of the N$_5$-H bond obtained by global analysis take place with τ_1= 18 μs (Table 3.3- 1800-1514 cm^{-1}) and 13 μs (Table 3.3- 730-380 nm) which is in agreement

with the time constant of the deprotonation of C72 (Figure 3.28B). Thus, we can infer that the formation of the N_5-H bond and deprotonation of the cysteine residue run in concert which probably is the rate limiting step for the formation of the adduct state.

4

Discussion

4.1 Channelrhodopsin-1

The mutations of specific amino acids can affect the photocycle of *CaChR1* in distinct ways. The time-resolved UV/Vis measurements presented by *Vera Muders* [33] have shown that the exchange of individual amino acids can strongly influence the behaviour of the photocycle intermediates. This means that under continuous illumination different intermediate compositions are accumulated for the different variants. Thus, the temporal and spectral overlapping of the intermediates makes it difficult to compare the IR vibrational bands and make a clear statement using only light-induced difference spectra.

These difficulties were solved by applying time-resolved IR spectroscopy using EC-QCLs, which provided the possibility of tracking the temporal evolution of the vibrational modes. In this work the time-resolved method enabled the detection of the complex pattern of difference bands in the carboxylic (C=O) and cysteine (S-H) vibrational range for *CaChR1* wild-type and the following variants D299N, D299E, E169Q, E136Q, D202N, C174T, C173T and C173/174T. By spectral and kinetics analysis, it is possible suggest the band assignment and point the timing of the deprotonation and protonation steps involving the carboxylic and cysteine amino acids. Solving, partially, the proton

transfer pathway for *CaChR1* photocycle.

4.1.1   Proton Transfer in the Cytoplasmic Side

This work was strongly focused on the contribution of the cysteine amino acids present in the *CaChR1* wild-type, detailing for the first time the time-evolution of the S-H vibrational range. Thus, a proton pathway in the cytoplasmic side of *CaChR1* is suggested in Figure 4.1. The light-induced FTIR experiment in *CaChR1* wild-type and variants allowed the preliminary band assignment in the C=O and S-H vibrational range. The aspartic acid D202 in *CaChR1* was investigated as the possible proton donor of the Schiff base, in analogy to the D156 amino acid that is the proton donor of the Schiff base in *CrChR2* photocycle [37]. The vibrational mode at (-)1760 cm^{-1} was assigned as the deprotonation band of the D202 amino acid [33].

The positive mode ((+)2544 cm^{-1}) in the S-H vibrational range was assigned as the protonation band of the C174 amino acid. However, the C173 amino acid also shows a minor influence in the positive S-H vibrational range, this can be an indication that more than one band is overlapped in this range. On top of it the negative mode at 2570 cm^{-1} is vanished or down-shifted in the C173T and C173/174T variants and reduced in size in the C174T variant. Here, we can speculate that the vibrational mode at (-)2570 cm^{-1} could indicate a moderate H-bond of C173 with a nearby amino acid and after the light excitation the C173 could be strong H-bond leading to the downshift in the vibrational frequency position in around 20-30 cm^{-1}. With the absence of the C173 amino acid the H-bond will no longer take place, affecting the vibrational frequency around (-)2570 cm^{-1} and consequently the positive vibrational range.

The time-resolved IR data suggests that the deprotonation of D202 takes place with the raising of the P$_2^{380}$ intermediate state, in a similar time interval as the protonation of C174 (Figure 3.18). On the other hand, the Schiff base is only re-protonated after $\sim$36 ms when the P$_2^{380}$ intermediate decays [29, 33], which is the same time range as the

reprotonation of D202 [33]. Therefore, the proton from D202 cannot go directly to the Schiff base, the proton needs to be stored elsewhere and must be provided by further amino acids and/or water molecules to the Schiff base. Based on this information we can suggest that the proton is transferred and stored in the C174 amino acid in the raising of the P_2^{380} intermediate state, in agreement with the time-resolved IR data. For this protonation take place, the C174 amino acid must be in the deprotonated condition in the ground state or in the raising of the P_1^{590} intermediate state. This way, the C174 amino acid will be able to go through protonation and deprotonation process during the lifetime of P_2^{380} intermediate state of the *CaChR1* photocycle.
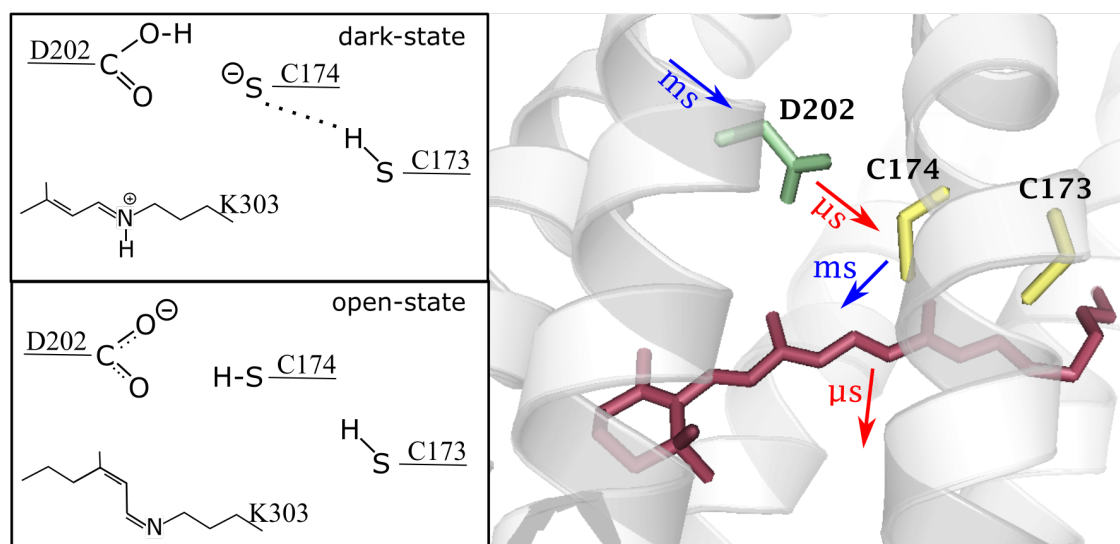
Figure 4.1: Suggested proton pathway involving the D202, C174 and C173 amino acids. The scheme in the left side is showing the dark state with protonated D202 and deprotonated C174 amino acids. After the green-light excitation *CaChR1* goes through several molecular changes, the lower panel shows the open conductive state (P_2^{380} intermediate) with deprotonated Schiff base and D202, while the C174 is protonated. The right side is the homology model with indications of the time range in which the deprotonation and protonation changes should happen.

The thiol groups, like the carboxylic groups, are subject to deprotonation processes through the loss of an H^+. By following the pKa of the thiol groups, the likelihood of deprotonation can be discerned. The pKa of an unperturbed cysteine residue from soluble proteins is about 8.5, which are usually protonated in the ground state [160] at physiological pH of ~7. However, reactive cysteines in proteins can often present

different pKa values [161–163]. This means that specific hydrogen-bond donors and electro-positive environments could affect the pKa of cysteines by lowering it due to the stabilization of the thiolate. The pKa could also be increased by destabilizing an adjacent negatively charged when the cysteine residues are exposed to a hydrophobic environment or an electro-negative local environment [161–163]. For cysteines present in redox-sensitive proteins [164], pKa values of 3.5 for thiol transferase and 5.4 for tyrosine phosphatase [165] were determined. Here, the low pKa value could be attributed to the cysteine side group be deprotonated and stabilized by adjacent positively charged or aromatic amino acid [166, 167]. Thus, it is clear that for multiple proteins the cysteine side groups can be deprotonated and play a key role in the protons transfer during the photocycle [168].

For *CaChR1*, our hypotheses is that the C173 amino acid would be continuously protonated and undergo only a hydrogen bond changes, while the C174 amino acid is deprotonated in the ground state and would be protonated during the transition to the P_2^{380} intermediate state. Consequently, the C174 amino acid would be the proton donor of the Schiff base in the decay of the P_2^{380} intermediate state. The proton transfer could be direct to the Schiff base or could also take place via a water molecule located between C174 and the Schiff base. The absence of the $(+)2544$ cm^{-1} band in the D202N carboxylic variant supports the assumption that the C174 is protonated by the D202 amino acid.

Even after the exchange of two cysteines (C173/174T variant - Figure 3.17), the vibrational mode at $(-)2559$ cm^{-1} remains visible in the S-H stretching vibration range. Thus, it is possible that the other cysteines are most likely to be responsible for this vibrational mode in the S-H range $((-)2559$ cm$^{-1})$. The thiol groups of cysteines can form hydrogen bonds within the α-helix, connecting with the oxygen atom of the peptide backbone or with an amino acid side group of an adjacent α-helix. If the latter case happens, hydrogen bond changes should be detectable if/when the helices move during the photocycle. This would be similar to what was observed for *CrChR2*

and BR where the helices B and F move when the channel is opened [169, 170]. In *CaChR1* there are no cysteine amino acids located on helix F. Thus, the cysteines localized on helix B (Figure 1.3 - C109, C133, C134, C141 and C101) would be the probable candidates to generate the negative mode in the S-H vibrational range [36]. For conclusive assignments of the negative S-H mode it would be necessary to expand the number of cysteine variants investigated.

4.1.2   Proton Transfer in the Extracellular Side

As shown in Figure 4.2 "below" to the retinal are located the three other carboxylic amino acids (D299, E169 and E136) investigated in this work as possible candidates to donate and accept protons. It is assumed that the E169 is protonated (pK$_a$ value $\simeq$9) and the D299 is likely to be deprotonated in the ground state (pK$_a$ value $\simeq$5) at pH 7.4 [38], favouring a strong hydrogen bond between D299 and E169. The pKa value of these two amino acids were determined by Li et. al. [38] with the titration analysis of the wild type and the E169 and D299 variants. In addition the passive ion current is strongly reduced when these two carboxyl groups are exchanged [29]. The E136 amino acid of *CaChR1* is analogous to the E90 in *CrChR2*, the E90 residue is protonated in the dark state but gets deprotonated in the late stages of the P$_4^{480}$ [37]. The equivalent amino acid in *CaChR1* (E136) has the opposite behavior, the residue is deprotonated in the ground state and gets protonated during the lifetime of the open P$_2^{380}$ state, as show in Figure 4.2.

The time-resolved IR data enables the detection of the vibrational mode at (+)1704 in the P$_1^{590}$ intermediate state of *CaChR1* wild-type (Figure 3.9). In agreement with Ogren et. al. [39], we suggest that the (+)1704 cm^{-1} modes indicate the proton transfer from E169 to D299 in the transition from ground state to the P$_1^{590}$ intermediate. As a result, the E169 amino acid would be deprotonated at the P$_1^{590}$ intermediate [39, 40, 116], where it is available to act as the primary proton acceptor of the Schiff base (Figure 4.2 - middle square). In accordance, the time-resolved UV/Vis data on the exchange of E169 into glutamine (Q) showed that the deprotonation of the Schiff base is delayed under this amino acid exchange [29, 33].

The carboxylic oxygen of D299 amino acid is positioned close to the protonated Schiff base in the ground state. In the transition from the ground state to the P$_1^{590}$, the isomerization of the retinal moves the proton of the Schiff base away from D299 (Figure 4.2 - middle square). Thus, the deprotonated D299 has the negative charge neutralized

by H^+-transfer from E169 in the picosecond time range during the lifetime of the P_1^{590} intermediate state [116]. It is also likely that the protonated Schiff base would be stabilized by interaction with the negatively charged C174 in the P_1^{590} intermediate.

Based on the changes observed in the 1730-1710 cm^{-1} range of E169Q variant in the P_2^{380} intermediate state, Ogren et. al. [39, 40] assigned the vibrational mode at $(+)1728$ cm^{-1} to the protonation of E169 by the Schiff base. They proposed that during the P_2^{380} intermediates the two carboxyl groups (E169 and D299) would be protonated, resulting in an unusual neutrality of the two counterions in the conductive state. However, the time-resolved data shown in Section 3.4.2 suggests a different interpretation. Here the proton transfer during the transition from the P_1^{590} to P_2^{380} intermediate also involves the E136 amino acid localized close by the Schiff base (Figure 4.2).

The vibrational mode 1720 cm^{-1}, assigned to E169 amino acid, evolves to a positive signal in the transition from P_1^{590} to P_2^{380} (Figure 3.24), suggesting that the E169 is reprotonated by the Schiff base in the raising of the P_2^{380} intermediate state. Thanks to the light-induced difference and time-resolved IR data we were able to assign the main positive vibrational mode at 1728 cm^{-1} to the protonation of the E136 amino acid (Figure 3.5), contrary to Ogren et. al. [40] who assigned the 1728 cm^{-1} to E169. The protonation of E136 happens in the transition from the P_1^{590} to P_2^{380} intermediate as shown the kinetics of Figure 3.23. Thus, the Schiff base transfers the proton to E169 while the D299 transfers the proton to E136. All these steps should happen concomitant or in similar time range of the proton transfer from the D202 to C174, as show in Figure 4.2-middle square. It is expected that the protonated E136 interacts with the deprotonated D299 during the lifetime of the P_2^{380} state,which can be inferred from the 4 cm^{-1} up-shift of the C=O stretch of E136 ($(+)1728$ cm^{-1}) upon D299N mutation [40]. Since the Shiff base is deprotonated in the P_2^{380} intermediate (open state), we expected that during the transition from the P_2^{380} to the P_4^{510} intermediate state the Shiff base is reprotonated by the C174 amino acid, while the D202 is reprotonated by a outside proton or via other amino acid and the E136 releases the proton, as show in Figure 4.2
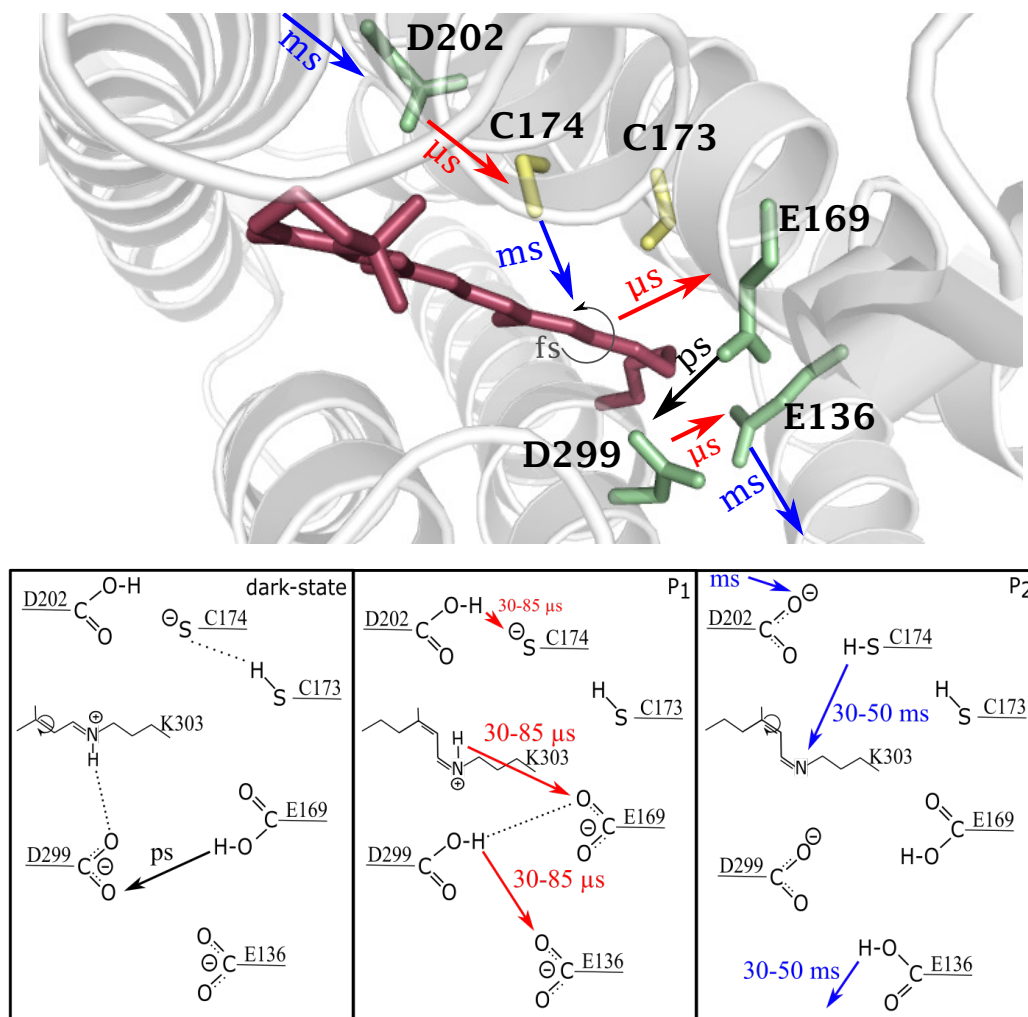
right square.

Figure 4.2: Suggested proton pathway involving all the amino acids used in this study. The upper side is the homology model with indications of the time range in which the deprotonation and protonation changes should happen. The lower side is the scheme showing the intermediate states accessed by time-resolved IR spectroscopy using EC-QCLs, the arrows indicate what will happen next. After the green-light excitation the *CaChR1* goes through several molecular changes, the left panel show the dark state with indication of the first protonation (D299) of the photocycle in the picosecond time range[116]. The black arrow is an indication only for the protonation of D299, for clarity the previous steps are not shown in this figure, but can be found in the Ref. [116]. At the center is displayed the configuration of the P_1^{590} intermediate state, the arrows indicate the concomitant steps in the transition to P_2^{380} intermediate. The right panel shows the P_2^{380} intermediate (open conductive state) with deprotonated Schiff base and D202 and protonated C174, the arrows indicate the concomitant steps in the transition to P_4^{510} intermediate.

4.2 *Dinoroseabacter Shibae* **LOV domain**

Different models have been suggested for the formation of the cystenyl-adduct state in LOV domains [50, 58, 69, 140, 171]. However, none of them have been able to determine the time of the cysteine deprotonation. Using a self-built time-resolved IR spectrometer setup we follow the changes in the vibrational mode of the reactive cysteine (2600-2500 cm^{-1} - S-H) and correlated it with the vibrational changes from the 1800-1510 cm^{-1} range. Based on these results and the comparison to literature, a mechanistic model of the DsLOV-M49S photocycle is presented in Figure 4.3.

Our investigations suggest a branched photocycle for the DsLOV-M49S showing two pathway decays of the triplet state (Figure 4.3). The fast decay component of the triplet state [LOV]^3 show a time constant of $\tau_{IR}^1 = 18$ μs (Table 3.3- 1800-1510 cm^{-1}) and $\tau_{UV/Vis}^1 = 13$ μs (Table 3.3- 730-380 nm), similar to the time constant found to the deprotonation of the reactive cysteine C72 ($\sim$12 μs). Thus, we can infer that the formation of the C$_{4a}$-S bond and deprotonation of the cysteine residue run in concert, being this the rate limiting step for the formation of the adduct state.

The second time constant detected by time-resolved IR and UV/Vis spectroscopy (83 μs and 196 μs, respectively - Table 3.3), corresponds to the decay of the triplet state back to the ground state without going through the formation of the adduct state. This is in agreement with Kutta et. al. [156], which also suggested that the FMN excited decay to the ground state can occur in two ways.

The results found in this work indicate that the transition from the triplet to the adduct state ($\sim$12-18 μs) is slower in DsLOV-M49S than the value usually found for other LOV domains [58, 157]. The rate decay in different steps of the photocycle can depend on a number of factors such as the concentration of dissolved oxygen in the sample, structural differences of DsLOV-M49S in relation to other LOV domains, alteration of hydrogen bonds and of hydrogen chemical bond and changes in the proton transfer

reaction due to the mutation. Studies conducted on AvLOV2 showed the possibility of amino acid exchange affect the access of oxygen molecules to the FMN binding pocket [157]. The mutation of specific amino acids could cause a slight movement of the sulfur atom of the reactive cysteine away from FMN, making it energetically less favorable the formation of S-C_{4a} bond [157, 172]. Besides this, different decay times of the triplet state using different buffers to AsLOV2, ~ 2 μs (sodium phosphate buffer) [58, 157], 6 μs (Tris buffer) [172] and 9.5 μs (deuterated buffer) [56] were found. Therefore, the above-mentioned factors individually or in combination could be the responsible in the rate limiting step of the triplet state decay.

An additional intermediate state in the transition from the triplet to the adduct state is strongly supported by the literature, where the radical-pair mechanism is the mostly likely to happen [52, 53, 65, 68, 69, 171, 173]. Considering the radical mechanism, the one proceeding via hydrogen atom transfer and consequently the formation of a neutral radical is energetically more favorable than passing via zwitterionic radical species [52, 65]. The QM/MM simulations [52] showed that the electron density at the N_5 atom increases during the $[LOV]^3$ transition, leading to a decrease in the $C_{4a}=N_5$ double-bound character. This could result in to the formation of a neutral radical pair. The formation of a possible radical intermediate state would generated an unpaired spin localized on the atoms involved in the adduct formation (Cys-S, FMN-C_{4a} and FMN-N_5) [52]. These conditions would produce a strong spin-orbit coupling constant, which enables an efficient triplet-singlet ISC by the sulfur atom. This would result in a rapid decay of the radical intermediate state.

The adduct formation via a radical-pair mechanism also has experimental support. Kottke et. al. [70] using absorption spectroscopy, mass spectrometry and X-ray crystal-lography investigated radical species produced by the cysteine variant of *Chlamydomonas* LOV1. Investigating the same sample, Bittl et. al. [71] identify the flavin radical species at the cysteine variant using electron paramagnetic resonance (EPR) and characterized it by electron nuclear double resonance (ENDOR). Beside these, Kutta et. al. [156]
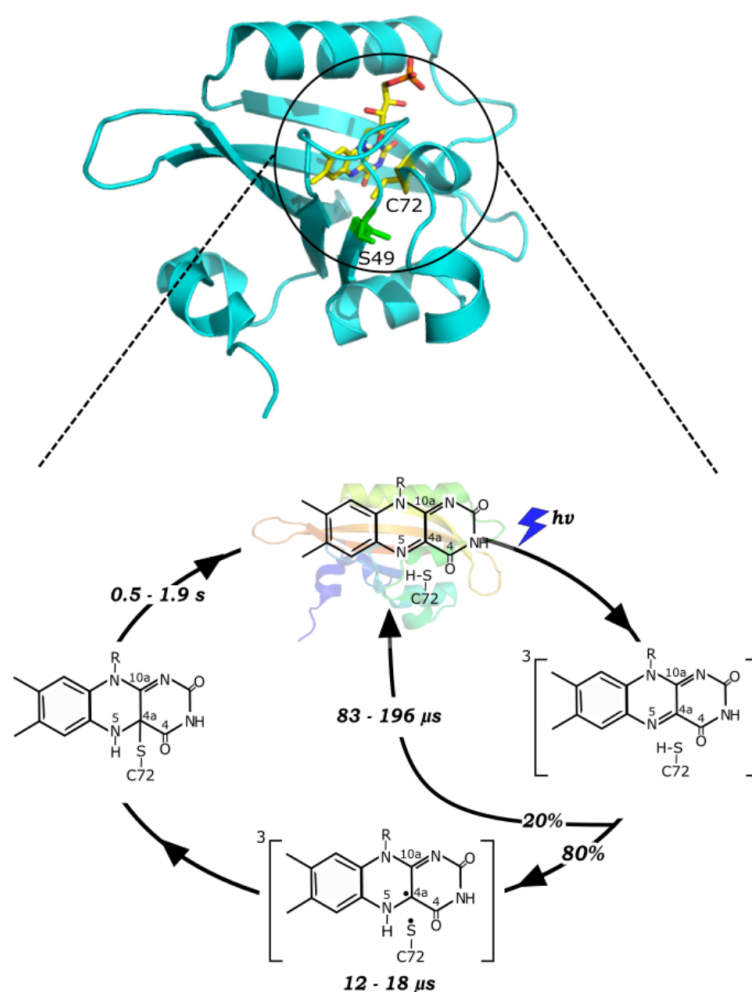
Figure 4.3: Scheme of the suggested photocycle of DsLOV-M49S initiated upon blue-light illumination. Time constants are derived from global analysis of time-resolved experimental data in the IR and UV/Vis region. After light excitation, the DsLOV-M49S relaxes to a triplet state $[LOV]^3$ where a small fraction is not forming the adduct state but rather decays back directly to the dark state. The fraction that go through the triplet state decays via concerted mechanism or via formation of a triplet radical state to form the adduct state $[LOV]^A$. At last the adduct state decay back to the ground state in a time range between 0.5 and 1.9 s.

found evidence for the radical intermediate by investigating wild-type LOV1, LOV2 and cysteine mutants from the PHOT protein of the green alga *Chlamydomonas reinhardtii*, where the presence of the radical anion to the cysteine variant was found. This suggests that the presence of a radial intermediate with short lifetime would be possible in the wild type. As discussed earlier (section 1.1.2), literature also proposes the formation of the adduct state via an ionic mechanism relying on a deprotonated functional cysteine before the covalent bond take place (C_{4a}-S) [58] and zwitterionic adduct species with

the thiol proton bonded at the sulfur atom [69]. However, both these mechanism look unlikely to occur in DsLOV-M49S, since the time-resolved IR data presented previously suggests an un-protonated [LOV]^3 and moderate S-H binding of the cysteine, where the decay of the triplet and the deprotonation of the reactive cysteine runs simultaneously with the covalent bond formation (C_{4a}-S).

Due to its short lifetime, it may well be that the flavin radical is not populated enough to be detected in a time-resolved experiment [152]. Another possibility is that a spectral contribution is obscured by the triplet signal as in the case for the neutral radical with similar marker bands compared to neutral triplet state [LOV]^3 at 1660 cm^{-1} and 1620 cm^{-1} [137]. Although we do not clearly detect a radical species in our time-resolved data, we also suggest a radical-pair mechanism for DsLOV-M49S. In the ionic mechanism, a proton transfer from the cysteine to FMN results in a protonated triplet state [69]. This is in contrast to the triplet state detected in our experiment which was identified as un-protonated by two marker bands at 1654 cm^{-1} and 1624 cm^{-1}. It is also possible that the protonated triplet state is formed as a short lived intermediate not detectable in our experiments. However, Kay et. al. [68] argued that this ionic mechanism is rather unlikely, given that both the flavin neutral radical (FMNH$^+$) and the adduct would be formed in a triplet state. Consequently, the adduct spin state would have been detectable in NMR experiments, which was not the case for the LOV2 domain of *Avena sativa* phototropin 1 [63, 68]. The absence of other intermediate states is corroborated by the concurrence of cysteine deprotonation ($\tau = 12$ μs) and adduct state formation ($\tau_{IR}^1 = 18$ μs, $\tau_{UV/Vis}^1 = 13$ μs). These findings and based on literature [63, 68] leaving a photoreaction via radical species as the most plausible scenario, at least for DsLOV-M49S that was the mechanism studied here.

Bibliography

[1] G. Nagel, D. Ollig, M. Fuhrmann, S. Kateriya, A. M. Musti, E. Bamberg, and P. Hegemann, "Channelrhodopsin-1: a light-gated proton channel in green algae," *Science*, vol. 296, pp. 2395–2398, 2002.

[2] E. S.Boyden, F. Zhang, E. Bamberg, G. Nagel, and K. Deisseroth, "Millisecond-timescale, genetically targeted optical control of neural activity," *Nat Neurosci*, vol. 8, p. 1263, 2005.

[3] T. Bruegmann, D. Malan, M. Hesse, T. Beiert, B. K. F. C. J. Fuegemann, and P. Sasse, "Optogenetic control of heart muscle in vitro and in vivo," *Nat Methods*, vol. 7, pp. 897–900, 2010.

[4] A. M. Packer, L. E. Russell, H. W. Dalgleish, and M. Hausser, "Simultaneous all-optical manipulation and recording of neural circuit activity with cellular resolution in vivo," *Nat Methods*, vol. 12, p. 140, 2015.

[5] M. Z. Lin and M. J. Schnitzer, "Genetically encoded indicators of neuronal activity," *Nat Neurosci*, vol. 19, p. 1142, 2016.

[6] H. H. Yang and F. St-Pierre, "Genetically encoded voltage indicators: opportunities and challenges," *J Neurosci*, vol. 36, pp. 9977–9989, 2016.

[7] G. Nagel, T. Szellas, W. Huhn, S. Kateriya, N. Adeishvili, P. Berthold, D. Ollig, P. Hegemann, and E. Bamberg, "Channelrhodopsin-2, a directly light-gated cation-selective membrane channel," *Proc Natl Acad Sci U S A*, vol. 10, pp. 13 940–13 945, 2003.

[8] G. Nagel, M. Brauner, J. F. Liewald, N. Adeishvili, E. Bamberg, and A. Gottschalk, "Light activation of channelrhodopsin-2 in excitable cells of *caenorhabditis elegans* trigger rapid behavioral response," *Curr Biol*, pp. 2279–2284, 2005.

[9] E. B. Purcell and S. Crosson, "Photoregulation in prokaryotes," *Curr Opin Microbiol.*, vol. 11, pp. 168–178, 2008.

[10] A. Moglich, X. Yang, R. Ayers, and K. Moffat, "Structure and function of plant photoreceptors," *Annu Rev Plant Biol*, vol. 61, pp. 21–47, 2010.

[11] M. Beeby, B. D. O'Connor, C. Ryttersgaard, D. R. Boutz, L. J. Perry, and T. O. Yeates, "The genomics of disulfide bonding and protein stabilization in thermophiles," *PLoS Biol.*, vol. 3, p. e309, 2005.

[12] S. M. Marino and V. N. Gladyshev, "Cysteine function governs its conservation and degeneration and restricts its utilization on protein surfaces," *J. Mol. Biol.*, vol. 404, pp. 902–916, 2010.

[13] F. R. Salsbury, S. T. Knutson, L. B. Poole, and J. S. Fetrow, "Functional site profiling and electrostatic analysis of cysteines modifiable to cysteine sulfenic acid," *Protein Sci.*, vol. 17, pp. 299–312, 2008.

[14] S. M. Marino and V. N. Gladyshev, "A structure-based approach for detection of thiol oxido reductases and their catalytic redox-active cysteine residues," *PLoS Comput. Biol.*, vol. 5, p. e1000383, 2009.

[15] O. P. Ernst, D. T. Lodowski, M. Elstner, P. Hegemann, L. S. Brown, and H. Kandori, "Microbial and animal rhodopsins: Structures, functions, and molecular mechanisms," *Chem.Rev.*, vol. 114, pp. 126–163, 2014.

[16] F. Tombola, M. M. Pathak, and E. Y. Isacoff, "How does voltage open an ion channel?" *Annu. Rev. Cell. Dev. Biol.*, vol. 22, pp. 23–52, 2006.

[17] E. Gouaux and R. Mackinnoni, "Principles of selective ion transport in channels and pumps," *Science*, vol. 310.5753, p. 1461–5, 2005.

[18] B. Corry and S. H. Chung, "Mechanisms of valence selectivity in biological ion channels," *Cell Mol Life Sci*, vol. 63.3, pp. 301–15, 2006.

[19] V. A. Lorentz-Fonfria and J. Heberle, "Channelrhodopsin unchained: Structure and mechanism of a light-gated cation channel," *Biochim Biophys Acta*, 2013.

[20] L. Fenno, O. Yizhar, and K. Deisseroth, "The development and application of optogenetics," *Annu. Rev. Neurasci.*, vol. 34, pp. 389–412, 2011.

[21] F. Schneider, C. Grimm, and P. Hegemann, "Biophysics of channelrhodopsin," *Annu Rev Biophys*, vol. 44, pp. 167–186, 2015.

[22] A. Zamani, S. Sakuragi, T. Ishizuka, and H. Yawo, "Kinetic characteristics of chimeric channelrhodopsins implicate the molecular identity involved in desensitization," *Biophys Physicobiol*, vol. 14, pp. 13–22, 2017.

[23] S. Y. Hou, E. G. Govorunova, M. Ntefidou, C. E. Lane, E. N. Spudich, O. A. Sineshchekov, and J. L. Spudich, "Diversity of chlamydomonas channelrhodopsin," *Photochem Photobiol*, vol. 88, pp. 119–128, 2012.

[24] E. G. Govorunova, E. N. Spudich, C. E. Lane, O. A. Sineshchekov, and J. L. Spudich, "New channelrhodopsin with red-shifted spectrum and rapid kinetics from *mesastigma viride*," *MBio*, vol. 2, pp. e00 115–00 111, 2011.

[25] F. Zhang, M. Prigge, F. Beyrière, S. P. Tsunoda, J. Mattis, O. Yizhar, P. Hegemann, and K. Deisseroth, "Red-shifted optogenetic excitation: a tool for fast neural control derived from *volvox carteri*," *Nat. Neurosci*, vol. 11, pp. 631–633, 2008.

[26] F. Zhang, J. Vierock, O. Yzhar, L. E. Fenno, S. Tsunoda, A. Kianianmomeni, M. Prigge, A. Berndt, J. Cushman, J. Polle, J. Magnuson, P. Hegemann, and

K. Deisseroth, "The microbial opsin family of optogenetic tools," *Cell*, vol. 147, pp. 1446–1457, 2011.

[27] H. E. Nack, I. Radu, C. Bamann, E. Bamberg, and J. Heberle, "The retinal structure of channelrhodopsin-2 assessed by resonance raman spectroscopy," *FEBS Lett.*, vol. 583, pp. 3676–3680, 2009.

[28] F. Litvin, O. Sineshchekov, and V. Sineshchekov, "Photoreceptor electric potential in the phototaxis of the alga *haematococcus pluvialis*," *Nature*, vol. 271(5644), pp. 476–8, 1978.

[29] O. A. Sineshchekov, E. G. Govorunova, J. Wang, H. Li, and J. L. Spudich, "Intramolecular proton transfer in channelrhodopsin," *Biophys J*, vol. 104, pp. 807–817, 2013.

[30] F. Kiefer, K. Arnold, M. Kunzli, L. Bordoli, and T. Schwede, "The swiss-model repository and associated resources," *Nucleic acids research*, vol. 37, pp. D387–392, 2009.

[31] K. Arnold, L. Bordoli, J. Kopp, and T. Schwede, "The swiss-model workspace: a web-based environment for protein structure homology modelling," *Bioinformatics*, vol. 22, pp. 195–201, 2006.

[32] P.-M. C. Guex, N. and T. Schwede, "Automated comparative protein structure modeling with swiss-model and swiss-pdbviewer: a historical perspective," *Electrophoresis*, vol. 30 Suppl 1, pp. S162–173, 2009.

[33] V. Muders. Biophysikalische Untersuchung von Channelrhodopsin-1 aus *Chlamydomonas augustae*, Dissertation, Freie Universität Berlin (2015).

[34] J. I. Ogren, S. Mamaev, D. Russano, H. Li, J. L. Spudch, and K. J. Rothschild, "Retinal chromophore structure and schiff base interactions in red-shifted

channelrhodopsin-1 from *chlamydomonas augustae*," *Biochemistry*, vol. 53, pp. 3961–3970, 2014.

[35] V. Muders, S. Kerruth, C. B. V. A. Lórenz-Fonfría, J. Heberle, and R. Schlesinger, "Resonance raman and ftir spectroscopy characterization of the closed and open states of channelrhodopsin-1," *FEBS Letters*, vol. 588, pp. 2301–2306, 2014.

[36] V. A. Lórenz-Fonfría, V. Muders, R. Schlesinger, and J. Heberle, "Changes in the hydrogen-bonding strength of internal water molecules and cysteine residues in the conductive state of channelrhodopsin-1," *Journal Chem Phys*, vol. 141, pp. 22D507–11, 2014.

[37] V. A. Lorenz-Fonfria, T. Resler, N. Krause, M. Nack, M. Grossing, G. F. von Mollard, C. Bamann, E. Bamberg, R. Schlesinger, and J. Heberle, "Transient protonation changes in chennelrhodopsin-2 and their relevance to channel gating," *PNAS*, vol. 110, pp. 1273–1281, 2013.

[38] H. Li, E. G. Govorunova, O. A. Sineshchekov, and J. L. Spudich, "Role of a helix b lysine residue in the photoactive site in channelrhodopsins," *Biophys J*, vol. 106, pp. 1607–1617, 2014.

[39] J. I. Ogren, A. Yi, S. Mamaev, H. Li, J. Lugtenburg, D. W. L, J. L. Spudich, and K. J. Rothschild, "Comparison of the structural changes occurring during the primary phototransition of two different channelrhodopsin from *chlamydomonas* algae," *Biochemistry*, vol. 54, pp. 377–388, 2014.

[40] J. I. Ogren, A. Yi, S. Mamaev, H. Li, J. L. Spudich, and K. J. Rothschild, "Proton transfer in channelrhodopsin-1 studied by fourier transform infrared (ftir) difference spectroscopy and site-directed mutagenesis," *J Biol Chem*, vol. 290, pp. 12 719–12 730, 2015.

[41] M. A. V. D. Horst and K. J. Hellingwer, "Photoreceptor proteins, "star actors of modern times": A review of the functional dynamics in the structure of

representative members of six different photoreceptor families," *Acc. Chem. Res.*, vol. 37, pp. 13–20, 2004.

[42] J. M. Christie, "Phototropin blue-light receptors," *Annu Rev Plant Biol*, vol. 58, pp. 21–45, 2007.

[43] J. Christie, P. Reymond, G. Powell, P. Bernasconi, A. Raibekas, E. Liscum, and W. Briggs, "Arabidopsis nph1: a flavoprotein with the properties of a photoreceptor for phototropism," *Science*, vol. 282(5394), pp. 1698–701, 1998.

[44] W. Briggs and C. JM, "Phototropins 1 and 2: versatile plant blue-light receptors," *Trends Plant Sci*, vol. 7, pp. 204–10, 2002.

[45] R. Celaya and E. Liscum, "Phototropins and associated signaling: providing the powerof movement in higher plants," *Photochem. Photobiol.*, vol. 81, pp. 73–80, 2005.

[46] K. Huang, T. Merkle, and C. Beck, "Isolation and characterization of a *chlamydomonas* gene that encodes a putative blue-light photoreceptor of the phototropin family," *Physiologia Plantarum*, vol. 115, pp. 613–22, 2002.

[47] M. Kasahara, T. Swartz, M. Olney, A. Onodera, N. Mochizuki, and et al., "Photochemical properties of the flavin mononucleotide-binding domains of the phototropins from *arabidopsis*, rice, and *chlamydomonas reinhardtii*," *Plant Physiol.*, vol. 129, pp. 762–73, 2002.

[48] K. Huang and C. Beck, "Phototropin is the blue-light receptor that controls multiple steps in the sexual life cycle of the green alga *chlamydomonas reinhardtii*," *Proc Natl Acad Sci U S A*, vol. 100(10), pp. 6269–74, 2003.

[49] B. Taylor and I. Zhulin, "Pas domains: internal sensors of oxygen, redox potential, and light," *Microbiol. Mol. Biol. Rev.*, vol. 63, pp. 479–506, 1999.

[50] M. Alexandre, T. Domratcheva, C. Bonetti, L. van Wilderen, R. van Grondelle, M. Groot, K. Hellingwerf, and J. Kennis, "Primary reactions of the lov2 domain of phototropin studied with ultrafast mid-infrared spectroscopy and quantum chemistry," *Biophys J*, vol. 97(1), pp. 227–37, 2009.

[51] T. Bednarz, A. Losi, W. Gartner, P. Hegemann, and J. Heberle, "Functional variations among lov domains as revealed by ft-ir difference spectroscopy," *Photochem Photobiol Sci*, vol. 3(6), pp. 575–9, 2004.

[52] M. Dittrich, P. Freddolino, and K. Schulten, "When light falls in lov: a quantum mechanical/molecular mechanical study of photoexcitation in phot-lov1 of chlamydomonas reinhardtii," *J Phys Chem B*, vol. 109(26), pp. 13 006–13, 2004.

[53] R. Fedorov, I. Schlichting, E. Hartmann, T. Domratcheva, M. Fuhrmann, and P. Hegemann, "Crystal structures and molecular mechanism of a light-induced signaling switch: The phot-lov1 domain from *chlamydomonas reinhardtii*," *Biophys J*, vol. 84(4), pp. 2474–82, 2003.

[54] S. Crosson and K. Moffat, "Structure of a flavin-binding plant photoreceptor domain: insights into light-mediated signal transduction," *Proc Natl Acad Sci U S A*, vol. 98(6), pp. 2995–3000, 2001.

[55] M. Salomon, W. Eisenreich, H. Durr, E. Schleicher, E. Knieb, V. Massey, W. Rudiger, F. Muller, A. Bacher, and G. Richter, "An optomechanical transducer in the blue light receptor phototropin from *avena sativa*," *Proc Natl Acad Sci U S A*, vol. 98(22), pp. 12 357–61, 2001.

[56] A. Gil, S. Laptenok, J. French, J. Iuliano, A. Lukacs, C. Hall, I. Sazanovich, G. Greetham, A. Bacher, B. Illarionov, M. Fischer, P. Tonge, and S. Meech, "Femtosecond to millisecond dynamics of light induced allostery in the avena sativa lov domain," *J Phys Chem B*, vol. 121(5), pp. 1010–1019, 2017.

[57] J. Kennis, S. Crosson, M. Gauden, I. van Stokkum, K. Moffat, and R. van Grondelle, "Primary reactions of the lov2 domain of phototropin, a plant blue-light photoreceptor," *Biochemistry*, vol. 42(12), pp. 3385–92, 2003.

[58] T. Swartz, S. Corchnoy, J. Christie, J. Lewis, I. Szundi, W. Briggs, and R. Bogomolni, "The photocycle of a flavin-binding domain of the blue light photoreceptor phototropin," *J Biol Chem*, vol. 276(39), pp. 36 493–500, 2001.

[59] T. Kottke, J. Heberle, D. Hehn, B. Dick, and P. Hegemann, "Phot-lov1: photocycle of a blue-light receptor domain from the green alga *chlamydomonas reinhardtii*," *Biophys J*, vol. 84(2 Pt 1), pp. 1192–201, 2003.

[60] S. Raffelberg, M. Mansurova, W. Gartner, and A. Losi, "Modulation of the photocycle of a lov domain photoreceptor by the hydrogen-bonding network," *J Am Chem Soc*, vol. 133(14), pp. 5346–56, 2011.

[61] A. Losi and W. Gartner, "The evolution of flavin-binding photoreceptors: an ancient chromophore serving trendy blue-light sensors," *Annu Rev Plant Biol*, vol. 63, pp. 49–72, 2012.

[62] J. Zayner and T. Sosnick, "Factors that control the chemistry of the lov domain photocycle," *PLoS One*, vol. 9(1), p. e87074, 2014.

[63] J. Kennis and T. Mathes, "Molecular eyes: proteins that transform light into biological information," *Interface Focus*, vol. 3(5), p. 20130005, 2013.

[64] K. Magerl, I. Stambolic, and B. Dick, "Switching from adduct formation to electron transfer in a light-oxygen-voltage domain containing the reactive cysteine," *Phys Chem Chem Phys*, vol. 19(17), pp. 10 808–10 819, 2017.

[65] C. Neiss and P. Saalfrank, "Ab initio quantum chemical investigation of the first steps of the photocycle of phototropin: a model study," *Photochem Photobiol*, vol. 77(1), pp. 101–9, 2003.

[66] K. Ataka, P. Hegemann, and J. Heberle, "Vibrational spectroscopy of an algal phot-lov1 domain probes the molecular changes associated with blue-light reception," *Biophys J*, vol. 84(1), pp. 466–74, 2003.

[67] T. Iwata, S. Tokutomi, and H. Kandori, "Photoreaction of the cysteine s-h group in the lov2 domain of adiantum phytochrome3," *J Am Chem Soc*, vol. 124(40), pp. 11 840–1, 2002.

[68] C. Kay, E. Schleicher, A. Kuppig, H. Hofner, W. Rudiger, M. Schleicher, M. Fischer, A. Bacher, S. Weber, and G. Richter, "Blue light perception in plants. detection and characterization of a light-induced neutral flavin radical in a c450a mutant of phototropin," *J Biol Chem*, vol. 278(13), pp. 10 973–82, 2003.

[69] E. Schleicher, R. Kowalczyk, C. Kay, P. Hegemann, A. Bacher, M. Fischer, R. Bittl, G. Richter, and S. Weber, "On the reaction mechanism of adduct formation in lov domains of the plant blue-light receptor phototropin," *J Am Chem Soc*, vol. 126(35), pp. 11 067–76, 2004.

[70] T. Kottke, B. Dick, R. Fedorov, I. Schlichting, R. Deutzmann, and P. Hegemann, "Irreversible photoreduction of flavin in a mutated phot-lov1 domain," *Biochemistry*, vol. 42(33), pp. 9854–62, 2017.

[71] R. Bittl, C. Kay, S. Weber, and P. Hegemann, "Characterization of a flavin radical product in a c57m mutant of a lov1 domain by electron paramagnetic resonance," *Biochemistry*, vol. 42(28), pp. 8506–12, 2003.

[72] K. Jentzsch, A. Wirtz, F. Circolone, T. Drepper, A. Losi, W. Gärtner, and et al., "Mutual exchange of kinetic properties by extended mutagenesis in two short lov domain proteins from *pseudomonas putida*," *Biochemistry-Us*, vol. 48(43), pp. 10 321–33, 2009.

[73] U. Krauss, A. Losi, W. Gärtner, K.-E. Jaeger, and T. Eggert, "Initial characterization of a blue-light sensing, phototropin-related protein from *pseudomonas*

putida: a paradigm for an extended lov construct," *Phys Chem Chem Phys*, vol. 7(14), pp. 2804–11, 2005.

[74] B. Zoltowski, C. Schwerdtfeger, J. Widom, J. Loros, A. Bilwes, J. Dunlap, and et al., "Conformational switching in the fungal light sensor vivid," *Science*, vol. 316(5827), pp. 1054–7, 2007.

[75] F. Circolone, J. Granzin, K. Jentzsch, T. Drepper, K. Jaeger, D. Willbold, and et al., "Structural basis for the slow dark recovery of a full-length lov protein from *pseudomonas putida*," *J Mol Biol*, vol. 417(4), pp. 362–74, 2012.

[76] K. C. KS, A. Bilwes, and B. Crane, "Light-induced subunit dissociation by a light-oxygen-voltage domain photoreceptor from *rhodobacter sphaeroides*," *Biochemistry-Us*, vol. 52(2), pp. 378–91, 2013.

[77] S. Metz, A. Jager, and G. Klug, "Light-induced subunit dissociation by a light-oxygen-voltage domain photoreceptor from of a short light, oxygen, voltage (lov) domain protein in blue light- and singlet oxygen-dependent gene regulation in *rhodobacter sphaeroides*," *Microbiology*, vol. 158(Pt 2), pp. 378–79, 2012.

[78] S. Endres, J. Granzin, F. Circolone, A. Stadler, U. Krauss, T. Drepper, V. Svensson, E. Knieps-Grunhagen, A. Wirtz, A. Cousin, P. Tielen, D. Willbold, K. Jaeger, and R. Batra-Safferling, "Structure and function of a short lov protein from the marine phototrophic bacterium *dinoroseobacter shibae*," *BMC Microbiol*, vol. 15, p. 30, 2015.

[79] T. Fettweiss, K. Rollen, J. Granzin, O. Reiners, S. Endres, T. Drepper, D. Willbold, K. Jaeger, R. Batra-Safferling, and U. Krauss, "Mechanistic basis of the fast dark recovery of the short lov protein dslov from *dinoroseobacter shibae*," *Biochemistry*, vol. 57(32), pp. 4833–4847, 2018.

[80] B. J. Schultz, H. Mohrmann, V. A. Lorenz-Fonfria, and J. Heberle, "Protein

dynamics observed by tunable mid-ir quantum cascade lasers across the time range from 10 ns to 1 s," *Spectrochimica Acta Part A*, vol. 188, pp. 666–674, 2018.

[81] V. A. Lorenz-Fonfria and J. Heberle, "Proton transfer and protein conformation dynamics in photosensitive proteins by time-resolved step-scan fourier-transform infrared spectroscopy," *J Vis Exp*, vol. 88, p. p. e51622, 2014.

[82] J. Chalmers and P. Griffiths, "Handbook of vibrational spectroscopy," *Wiley*, vol. 5 volumes set., 2002.

[83] F. Siebert and P. Hildebrandt, "Vibrational spectroscopy in life science," *John-Wiley & Sons*, 2008.

[84] P. Atkins, J. D. Paula, and R. Friedman, "Quanta, matter, and change: a molecular approach to physical chemistry," *Oxford University Press*, 2009.

[85] A. Kolezynski and M. Krol, "Molecular spectroscopy: Experiment and theory: From molecules to functional," *Springer*, 2016.

[86] P. Bernath, "Spectra of atoms and molecules," *Oxford University Press, USA*, 2005.

[87] I. Campbell, "Biophysical techniques," *Oxford University Press*, 2012.

[88] H. W., P. A., F. M., and H. P., "Spectroscopic characterization of flavin mononucleotide bound to the lov1 domain of phot1 from *chlamydomonas reinhardtii*," *Photochem. Photobiol.*, vol. 75, p. 479, 2002.

[89] D. A. Naylor and M. K. Tahic, "Apodizing functions for fourier transform spectroscopy," *J. Opt. Soc. Am. A*, vol. 24, pp. 3644–3648, 2007.

[90] A. S. Filler, "Apodization and interpolation in fourier transform spectroscopy," *J. Opt. Soc. Am.*, vol. 54, pp. 762–767, 1964.

[91] R. H. Norton and R. Beer, "New apodizing functions for fourier spectrometry," *J. Opt. Soc. Am.*, vol. 66, pp. 259–264, 1976.

[92] J. Faist, F. Capasso, D. L. Sivco, C. Sirtori, A. L. Hutchinson, and A. Y. Cho, "Quantum cascade laser," *Science*, vol. 264, pp. 553–556, 1994.

[93] R. W. Hendler and R. I. Shrager, "Deconvolutions based on singular value decomposition and the pseudoinverse: a guide for beginners," *J Biochem Biophys Methods*, vol. 28(1), pp. 1–33, 1994.

[94] G. F. Dorlhiac, C. Fare, and J. J. van Thor, "Pyldm - an open source package for lifetime density analysis of time-resolved spectroscopic data," *PLOS Comput Biol*, vol. 15(5), p. 1–15, 2017.

[95] V. B. Bergo, M. Ntefidou, V. D. Trivedi, J. J. Amsden, J. M. Kralj, K. J. Rothschild, and J. L. Spudich, "Conformarional changes in the photocycle of *anabaena* sensory rhodopsin: abscence of Schiff base counterion protonation signal," *J. Biol. Chem*, vol. 281, pp. 15 208–15 214, 2006.

[96] M. S. Braiman, T. Mogi, T. Marti, L. J. Stern, H. G. Khorana, and K. J. Rosthschild, "Vibrational spectroscopy of bacteriorhodopsin mutants: light-driven proton transport involves protonation changes of aspartic acid residues 85, 96 and 212," *Biochemistry*, vol. 27, pp. 8516–8520, 1988.

[97] S. O. Smith, J. Lugtenburg, and R. A. Mathies, "Determination of the retinal chromophore structure in bacteriorhodopsin with resonance raman spectrocopy," *J. Membr. Biol*, vol. 85, pp. 95–109, 1985.

[98] S. O. Smith, M. S. Braiman, J. A. P. A. B. Myers, J. M. L. Courtin, C. Winkel, J. Lugtenburg, and R. A. Mathies, "Vibrational analysis of the all-trans-retinal chromophore in light- and dark- adapted bacteriorhodopsin," *J. Am. Chem. Soc.*, vol. 109, pp. 3108–3125, 1987.

[99] S. O. Smith, I. Hornung, R. V. der Steen, J. A. Pardoen, M. S. Braiman, J. Lugten-burg, and R. A. Mathies, "Are c14-c15 single bond isomerizations of the retinal chromophore involved in the proton-pumping mechanism of bacteriorhodopsin?" *Proc. Natl. Acad. Sci. U.S.A.*, vol. 83, pp. 967–971, 1986.

[100] K. Gerwert and F. Siebert, "Evidence for light-induced 13-*cis*, 14-s-*cis* isomeriza-tion in bacteriorhodopsin obtained by ftir difference spectroscopy using isotopically labelled retinals," *EMBO J.*, vol. 5, pp. 805–811, 1986.

[101] A. Maeda, "Application of ftir spectroscopy to the structural study on the function of bacteriorhodopsin," *Isr. J. Chem*, vol. 35, pp. 387–400, 1995.

[102] S. Krimm and J. Bandekar, "Vibrational spectroscopy and conformation of peptides, polypeptides, and proteins," *Adv. Protein Chem.*, vol. 38, p. 181, 1986.

[103] E. Goormaghtigh, V. Cabiaux, and J. Ruysschaert, "Determination of soluble and membrane protein structure by fourier transform infrared spectroscopy. iii. secondary structures," *Subcell Biochem*, vol. 23, pp. 405–50, 1994.

[104] N. Dave, V. A. Lórenz-Fonfría, G. Leblanc, and E. Padrós, "Ftir spectroscopy of secondary-structure reorientation of melibiose permease modulated by substrate binding," *Biophys. J.*, vol. 94(9), p. 3659, 2008.

[105] M. Nack, I. Radu, B. J. Schultz, T. Resler, R. Schlesinger, A. N. Bondar, C. del Val, S. Annruzzetti, C. Viappiani, C. Bamann, E. Bamberg, and J. Heberle, "Kinetics of proton release and uptake by channelrhodopsin-2," *FEBS letters*, vol. 586, pp. 1344–1348, 2012.

[106] A. Barth, "The infrared absorption of amino acid side chains," *Prog Biophys Mol Biol*, vol. 4, pp. 141–173, 2000.

[107] H. Li and G. J. Thomas, "Cysteine conformation and sulfhydryl interactions in proteins and viruses. 1. correlation of the raman s-h band with hydrogen bonding

and intramolecular geometry in model compounds," *J. Am. Chem. Soc.*, vol. 113, pp. 456–462, 1991.

[108] G. H. Bare, J. O. Alben, and P. A. Bromberg, "Sulfhydryl groups in hemoglobin. a new molecular probe at the $\alpha_1\beta_1$ interface studied by fourier transform infrared spectroscopy," *Biochemistry*, vol. 14, pp. 1578–1583, 1975.

[109] Y. Furutani, A. G. Bezerra, S. Waschuk, M. Sumii, L. S. Brown, and H. Kandori, "Ftir spectroscopy of the k photointermediate of *neurospora* rhodopsin: Structural changes of the retinal, protein, and water molecules after photoisomerization," *Biochemistry*, vol. 43, pp. 9636–9646, 2004.

[110] A. Kawanabe, Y. Furutani, K. Jung, and H. Kandori, "Ftir study of the photoisomerization processes in the 13-cis and all-trans forms of anabaena sensory rhodopsin at 77 k," *Biochemistry*, vol. 45, pp. 4362–4370, 2006.

[111] S. Ito, H. E. Kato, R. Taniguchi, T. Iwata, O. Nureki, and H. Kandori, "Water-containing hydrogen-bonding network in the active center of channelrhodopsin," *J.Am.Chem.Soc.*, vol. 136, pp. 3475–3482, 2014.

[112] H. C. Watanabe, K. Welke, F. Schneider, S. Tsunoda, F. Zhang, K. Deisseroth, P. Hegemann, and M. Elstner, "Structural model of channelrhodopsin," *J Biol Chem*, vol. 287, pp. 7456–7466, 2012.

[113] P. Zhou, F. Tian, F. Lv, and Z. Shang, "Geometric characteristics of hydrogen bonds involving sulfur atoms in proteins," *Proteins*, vol. 76, p. 151, 2009.

[114] V. A. Lorenz-Fonfria, J. B. Schultz, T. Resler, R. Schlesinger, C. Bamann, E. Bamberg, and J. Heberle, "Pre-gating conformational changes in the cheta variant of channelrhodopsin-2 monitored by nanosecond ir spectroscopy," *JACS*, vol. 137, pp. 1850–1860, 2015.

[115] V. B. Bergo, M. Ntefidou, V. D. Trivedi, J. J. Amsden, J. M. Kralj, K. J. Rothschild, and J. L. Spudich, "Conformational changes in the photocycle of anabaena sensory rhodopsin: absence of the schiff base counterion protonation signal," *J Biol Chem*, vol. 281, pp. 15 208–15 214, 2006.

[116] T. Stensitzki, S. Adam, I. S. R. Schlesinger, and K. Heyne, "Ultrafast backbone protonation in channelrhodopsin-1 captured by polarization resolved fs vis-pump—ir-probe spectroscopy and computational methods," *Molecules*, vol. 848, p. 25, 2020.

[117] B. Nie, J. Stutzman, and A. Xie, "A vibrational spectral maker for probing the hydrogen-bonding status of protonated asp and glu residues," *Biophys J*, vol. 88(4), pp. 2833–2847, 2005.

[118] M. Nack, I. Radu, M. Gossing, C. Bamann, E. Bamberg, G. F. von Mollard, and J. Heberle, "The dc gate in channelrhodopsin-2: crucial hydrogen bonding interaction between c128 and d156," *Photochem. Photobiol. Sci.*, vol. 9, pp. 194–198, 2010.

[119] F. Siebert and W. Maentele, "Investigation of the primary photochemistry of bacteriorhodopsin by low-temperature fourier-transform infrared spectroscopy," *Eur. J. Biochem.*, vol. 130, pp. 565–573, 1983.

[120] K. Bagley, G. Dollinger, L. Eisenstein, A. K. Singh, and L. Zimanyi, "Fourier transform infrared difference spectroscopy of bacteriorhodopsin and its photoproducts," *Proc. Natl. Acad. Sci. U.S.A.*, vol. 79, pp. 4972–4976, 1982.

[121] K. Rothschild and H. Marrero, "Infrared evidence that the schiff base of bacteriorhodopsin is protonated: br570 and k intermediates," *Proc. Natl. Acad. Sci. U.S.A.*, vol. 79, pp. 4045–4049, 1982.

[122] K. J. Rothschild, H. Marrero, M. Braiman, and R. Mathies, "Primary photochemistry of bacteriorhodopsin: Comparison of fourier transform infrared difference

spectra with resonance raman spectra," *Photochem. Photobiol.*, vol. 40, pp. 675–679, 1984.

[123] F. S. Parker, "Applications of infrared, raman and resonance raman spectroscopy in biochemistry," *Plenum Press*, 1983.

[124] A. Barth and C. Zscherp, "What vibrations tell us about proteins," *Q. Rev. Biophys.*, vol. 35, pp. 369–430, 2002.

[125] M. K. Neumann-Verhoefen, K. Neumann, C. Bamann, I. Radu, J. Heberle, E. Bamberg, and Wachtveitl, "Ultrafast infrared spectroscopy on channelrhodopsin-2 reveals efficient energy transfer from the retinal chromophore to the protein," *J. Am. Chem. Soc.*, vol. 35, pp. 6968–6976, 2013.

[126] C. Zscherp and J. Heberle, "Infrared difference spectra of the intermediates l, m, n, and o of the bacteriorhodopsin photoreaction obtained by time-resolved attenuated total reflection spectroscopy," *J Phys Chem B*, vol. 101(49), pp. 10 542–10 547, 1997.

[127] H. Li, C. J. Wurrey, and G. J. Thomas, "Cysteine conformation and sulfhydryl interactions in proteins and viruses. 2. normal coordinate analysis of the cysteine side chain in model compounds," *J. Am. Chem. Soc.*, vol. 114(19), pp. 7463–7469, 1992.

[128] S. Walsh, R. Cheng, W. Wright, D. Alonso, V. Daggett, J. Vanderkooi, and W. DeGrado, "The hydration of amides in helices; a comprehensive picture from molecular dynamics, ir, and nmr," *Protein Sci*, vol. 12(3), pp. 520–31, 2003.

[129] D. Paschek, M. Puhse, A. Perez-Goicochea, S. Gnanakaran, A. Garcia, R. Winter, and A. Geige, "The solvent-dependent shift of the amide i band of a fully solvated peptide as a local probe for the solvent composition in the peptide/solvent interface," *Chemphyschem*, vol. 9(18), pp. 2742–50, 2008.

[130] K. Takei, R. Takahashi, and T. Noguchi, "Correlation between the hydrogen-bond structures and the c=o stretching frequencies of carboxylic acids as studied by density functional theory calculations: Theoretical basis for interpretation of infrared bands of carboxylic groups in proteins," *J. Phys. Chem. B.*, vol. 112(21), p. 6725–6731, 2008.

[131] G. Iliadis, G. Zundel, and B. Brzezinski, "Aspartic proteinases—fourier transform ir studies of the aspartic carboxylic groups in the active site of pepsin," *FEBS. Lett.*, vol. 352(3), p. 315–317, 1994.

[132] S. Kerruth, P. Langner, S. Raffelberg, W. Gartner, and J. Heberle, "Characterization of the blue-light-activated adenylyl cyclase mpac by flash photolysis and ftir spectroscopy," *Photochem Photobiol*, vol. 93(3), pp. 857–864, 2017.

[133] C. Martin, X. Shi, M. Tsao, D. Karweik, J. Brooke, C. Hadad, and M. Platz, "The photochemistry of riboflavin tetraacetate and nucleosides. a study using density functional theory, laser flash photolysis, fluorescence, uv-vis, and time resolved infrared spectroscopy," *Journal of Physical Chemistry B*, vol. 106(39), pp. 10 263–10 271, 2002.

[134] W. Bowman and T. Spiro, "Normal mode analysis of lumiflavin and interpretation of resonance raman spectra of flavoproteins," *Biochemistry*, vol. 20(11), pp. 3313–8, 1981.

[135] T. Iwata, D. Nozaki, Y. Sato, K. Sato, Y. Nishina, K. Shiga, and S. T. H. Kandori, "Identification of the c=o stretching vibrations of fmn and peptide backbone by 13c-labeling of the lov2 domain of adiantum phytochrome3," *Biochemistry*, vol. 45(51), pp. 15 384–91, 2006.

[136] Y. Zheng, J. Dong, B. Palfey, and P. Carey, "Carey, using raman spectroscopy to monitor the solvent-exposed and "buried" forms of flavin in p-hydroxybenzoate hydroxylase," *Biochemistry*, vol. 38(51), pp. 16 727–32, 1999.

[137] C. Martin, M. Tsao, C. Hadad, and M. Platz, "The reaction of triplet flavin with indole. a study of the cascade of reactive intermediates using density functional theory and time resolved infrared spectroscopy," *J Am Chem Soc*, vol. 124(24), pp. 7226–34, 2002.

[138] M. Benecky, R. Copeland, and T. Spiro, "Resonance raman spectra of flavin semiquinones stabilized by n5 methylation," *Biochim Biophys Acta*, vol. 760(1), pp. 163–8, 1983.

[139] M. Tegoni, M. Gervais, and A. Desbois, "Resonance raman study on the oxidized and anionic semiquinone forms of flavocytochrome b2 and l-lactate monooxygenase. influence of the structure and environment of the isoalloxazine ring on the flavin function," *Biochemistry*, vol. 36(29), pp. 8932–46, 1997.

[140] C. Thöing, A. Pfeifer, S. Kakorin, and T. Kottke, "Protonated triplet-excited flavin resolved by step-scan ftir spectroscopy: implications for photosensory lov domains," *Phys Chem Chem Phys*, vol. 15(16), pp. 5916–26, 2013.

[141] T. Kitagawa, Y. Nishina, Y. Kyogoku, T. Yamano, N. Ohishi, A. Takai-Suzuki, and K. Yagi, "Resonance raman spectra of carbon-13- and nitrogen-15-labeled riboflavin bound to egg-white flavoprotein," *Biochemistry*, vol. 18(9), pp. 1804–8, 1979.

[142] P. Dutta, R. Spencer, C. Walsh, and T. Spiro, "Resonance raman and coherent anti-stokes raman scattering spectra of flavin derivatives. vibrational assignments and the zwitterionic structure of 8-methylamino-riboflavin," *Biochim Biophys Acta*, vol. 623(1), pp. 77–83, 1980.

[143] Y. Nishina, K. Shiga, K. Horiike, H. Tojo, S. Kasai, K. Matsui, H. Watari, and T. Yamano, "Resonance raman spectra of semiquinone forms of flavins bound to riboflavin binding protein," *J Biochem*, vol. 88(2), pp. 411–6, 1980.

[144] Y. Su and G. Tripathi, "Time-resolved resonance raman observation of protein-free riboflavin semiquinone radicals," *JACS*, vol. 116(10), pp. 4405–4407, 1994.

[145] I. Hazekawa, Y. Nishina, K. Sato, M. Shichiri, R. Miura, and K. Shiga, "A raman study on the c(4)=o stretching mode of flavins in flavoenzymes: hydrogen bonding at the c(4)=o moiety," *J Biochem*, vol. 121(6), pp. 1147–54, 1997.

[146] D. Murgida, E. Schleicher, A. Bacher, G. Richter, and P. Hildebrandt, "Resonance raman spectroscopic study of the neutral flavin radical complex of dna photolyase from escherichia coli," *J Raman Spectrosc*, vol. 32(6-7), pp. 551–556, 2001.

[147] M. Abea and Y. Kyogoku, "Vibrational analysis of flavin derivatives - normal coordinate treatments of lumiflavin," *Spectrochimica Acta Part a-Molecular and Biomolecular Spectroscopy*, vol. 43(8), pp. 1027–1037, 1987.

[148] Y. M. Abe, T. Kitagawa, K. Kawano, N. Ohishi, A. Takai-Suzuki, and K. Yagi, "lnfrared spectra and molecular association of lumiflavin and riboflavin derivatives," *Spectrochimica Acta*, vol. 42A(9)), p. 1059–68, 1986.

[149] H. Tojo and K. Shiga, "Resonance raman spectra of anionic semiquinoid form of a flavoenzyme, d-amino acid oxidase," *J Biochem*, vol. 104(2), pp. 227–31, 1988.

[150] J. Iuliano, A. Gil, S. Laptenok, C. Hall, J. T. Collado, A. Lukacs, S. H. Ahmed, J. Abyad, T. Daryaee, G. Greetham, I. Sazanovich, B. Illarionov, A. Bacher, M. Fischer, M. Towrie, J. French, S. Meech, and P. Tonge, "Variation in lov photoreceptor activation dynamics probed by time-resolved infrared spectroscopy," *Biochemistry*, vol. 57(5), pp. 620–630, 2018.

[151] T. Swartz, P. Wenzel, S. Corchnoy, W. Briggs, and R. Bogomolni, "Vibration spectroscopy reveals light-induced chromophore and protein structural changes in the lov2 domain of the plant blue-light receptor phototropin 1," *Biochemistry*, vol. 41(23), pp. 7183–9, 2002.

[152] A. Pfeifer, T. Majerus, K. Zikihara, D. Matsuoka, S. Tokutomi, J. Heberle, and T. Kottke, "Time-resolved fourier transform infrared study on photoadduct formation and secondary structural changes within the phototropin lov domain," *Biophys J*, vol. 96(4), pp. 1462–70, 2009.

[153] P. E. Konold, T. Mathes, J. Weibetaenborn, M. L. Groot, P. Hegemann, and J. T. Kennis, "Unfolding of the c-terminal j-α helix in the lov2 photoreceptor domain observed by time-resolved vibrational spectroscopy," *J Phys Chem Lett*, vol. 7(17), pp. 3472–6, 2016.

[154] A. Halavaty and K. Moffat, "N- and c-terminal flanking regions modulate light-induced signal transduction in the lov2 domain of the blue light sensor phototropin 1 from avena sativa," *Biochemistry*, vol. 46(49), pp. 14 001–9, 2007.

[155] G. Bare, J. Alben, and P. Bromberg, "Sulfhydryl groups in hemoglobin. a new molecular probe at the alpha1 beta 1 interface studied by fourier transform infrared spectroscopy," *Biochemistry*, vol. 14(8), pp. 1578–83, 1975.

[156] R. Kutta, K. Magerl, U. Kensy, and B. Dick, "A search for radical intermediates in the photocycle of lov domains," *Photochem Photobiol Sci*, vol. 14(2), pp. 288–99, 2015.

[157] S. Song, P. Freddolino, A. Nash, E. Carroll, K. Schulten, K. Gardner, and D. Larsen, "Modulating lov domain photodynamics with a residue alteration outside the chromophore binding site," *Biochemistry*, vol. 50(13), pp. 2411–23, 2011.

[158] P. Freddolino, A. Arkhipov, S. Larson, A. McPherson, and K. Schulten, "Molecular dynamics simulations of the complete satellite tobacco mosaic virus," *Structure*, vol. 14(3), pp. 437–449, 2006.

[159] J. Zayner, C. Antoniou, and T. Sosnick, "The amino-terminal helix modulates

light-activated conformational changes in aslov2," *J Mol Biol*, vol. 419(1-2), pp. 61–74, 2012.

[160] G. Giles, K. Tasker, and C. Jacob, "Hypothesis: the role of reactive sulfur species in oxidative stress," *Free Radic Biol Med*, vol. 31(10), pp. 1279–83, 2001.

[161] T. Kortemme and T. E. Creighton, "Ionisation of cysteine residues at the termini of model alpha-helical peptides, relevance to unusual thiol pk$_a$ values in proteins of the thioredoxin family," *J Mol Biol.*, vol. 253, p. 799–812, 1995.

[162] J. Hennecke, C. Spleiss, and R. Glockshuber, "Influence of acidic residues and the kink in the active-site helix on the properties of the disulfide oxidoreductase dsba," *J Biol Chem.*, vol. 272, p. 189–195, 1997.

[163] S. Pinitglang, M. Noble, E. W. T. C. Verma, and K. Brocklehurst, "Studies on the enhancement of the reactivity of the (cys-25)-s-/(his159)-im+h ion-pair of papain by deprotonation across pka 4," *Biochem Soc Trans.*, vol. 24, p. 468S, 1996.

[164] N. Brandes, S. Schmitt, and U. Jakob, "Thiol-based redox switches in eukaryotic proteins, antioxidants & redox signaling," vol. 11(5), pp. 997–1014, 2009.

[165] D. Lohse, J. Denu, N. Santoro, and J. Dixon, "Roles of aspartic acid-181 and serine-222 in intermediate formation and hydrolysis of the mammalian protein-tyrosine-phosphatase ptp1," *Biochemistry*, vol. 36(15), pp. 4568–75, 1997.

[166] Z. Y. Zhang and J. E. Dixon, "Active site labeling of the yersinia protein tyrosine phosphatese: the determination of the pka of the active site cysteine and the function of the conserved histidine 402," *Biochemistry*, vol. 32, pp. 9340–9345, 1993.

[167] S. Rhee, Y. Bae, S. Lee, and J. Kwon, "Hydrogen peroxide: a key messenger that

modulates protein phosphorylation through cysteine oxidation," *Sci STKE*, vol. 2000(53), p. pe1, 2000.

[168] S. Marino and V. Gladyshev, "Analysis and functional prediction of reactive cysteine residues," *Journal Biol Chem*, vol. 287(7), pp. 4419–25, 2012.

[169] N. Krause, C. Engelhard, J. Heberle, R. Schlesinger, and R. Bittl, "Strutctural difference between the close and open states of channelrhodopsin-2 observed by epr spectroscopy," *FEBS letters*, vol. 587, pp. 3309–3313, 2013.

[170] T. Sattig, C. Rickert, E. Bamberg, H. Steinhoff, and C. Bamann, "Light-induced movement of the transmembrane helix b in channelrhodopsin-2," *Angewandte Chemie*, vol. 52(37), pp. 9705–8, 2013.

[171] T. Domratcheva, R. Fedorov, and I. Schlichting, "Schlichting, analysis of the primary photocycle reactions occurring in the light, oxygen, and voltage blue-light receptor by multiconfigurational quantum-chemical methods," *J Chem Theory Comput*, vol. 2(6), pp. 1565–74, 2006.

[172] J. Christie, S. Corchnoy, T. Swartz, M. Hokenson, I. Han, W. Briggs, and R. Bogomolni, "Steric interactions stabilize the signaling state of the lov2 domain of phototropin 1," *Biochemistry*, vol. 46(32), pp. 9310–9, 2007.

[173] S. Nakagawa, O. Weingart, and C. Marian, "Dual photochemical reaction pathway in flavin-based photoreceptor lov domain: A combined quantum-mechanics/molecular-mechanics investigation," *J Phys Chem B*, vol. 121(41), pp. 9583–9596, 2017.

List of Publications

[1] Maia, R., Ehrenberg, D., Oldemeyer, S., Knieps-Grünhagen, E., Krauss, U., Heberle, J., Real-time Tracking of Proton Transfer from the Reactive Cysteine to the Flavin Chromophore of a Photosensing Light Oxygen Voltage Protein. JACS (2021), *accepted for publication.*

[2] Harris, A., Saita, M., Resler, T., Hughes-Visentin, A., Maia, R., Pranga-Sellnau, F., Bondar, A.-N., Heberle, J., Brown, L. S., Molecular details of the unique mechanism of chloride transport by a cyanobacterial rhodopsin. Phys. Chem. Chem. Phys. (2018), 20, 3184-3199, DOI: 10.1039/c7cp06068h.

Acknowledgments

Declaration of authorship

Name: Antonelli Maia

First name: Raiza Nara

I declare to the Freie Universität Berlin that I have completed the submitted dissertation independently and without the use of sources and aids other than those indicated. The present thesis is free of plagiarism. I have marked as such all statements that are taken literally or in content from other writings. This dissertation has not been submitted in the same or similar form in any previous doctoral procedure. I agree to have my thesis examined by a plagiarism examination software.

Date: Signature: